
LHC EFFECTIVE MODEL FOR OPTICS CORRECTIONS

Measurements and corrections of high-order non-linear optics

MAËL LE GARREC

Check yourself before you Shrek yourself.

ICE CUBE FT. SHREK

Abstract

Zusammenfassung

Acknowledgements

cimer les gens

Contents

Abstract	v
Zusammenfassung	vii
Acknowledgements	ix
Contents	x
Glossary	xv
1. Introduction	1
1.1. Motivation	1
1.2. Thesis Outline	1
1.3. Particle Accelerators and CERN	1
1.3.1. Particle Accelerators	1
1.3.2. The CERN Complex	2
1.3.3. The Large Hadron Collider	2
1.4. Tools and Softwares	6
2. Concepts of Accelerator Physics	7
2.1. Introduction	7
2.2. Magnetic Fields	7
2.2.1. Nomenclature	7
2.2.2. Multipole Expansion	8
2.2.3. Beam Rigidity and Normalization	8
2.2.4. Hamiltonian	9
2.3. Coordinate Systems	10
2.3.1. Frenet-Serret System	10
2.3.2. Linear Lattice	10

2.3.3. Non-Linear Lattice	14
2.4. Examples of Maps	19
2.4.1. Non-Linear Transfer of a Single Sextupole	20
2.4.2. Non-Linear Transfer of Two Sextupoles	21
2.5. Observables	23
2.5.1. Dispersion	23
2.5.2. β -function	23
2.5.3. Coupling	24
2.5.4. Momentum Compaction Factor	25
2.6. Detuning Effects	25
2.6.1. Chromaticity	25
2.6.2. Amplitude Detuning	28
2.6.3. Chromatic Amplitude Detuning	29
2.6.4. Feed-Down	30
2.7. Resonances	30
2.7.1. Tune Diagram	30
2.7.2. Frequency Spectrum	30
2.7.3. Resonance Driving Terms	32
3. Optics Measurements and Corrections	33
3.1. Beam Instrumentation	33
3.1.1. Beam Position Monitors	33
3.1.2. Collimators	34
3.1.3. Beam Loss Monitors	34
3.1.4. AC-Dipole	34
3.2. Correction Principles	35
3.2.1. Response Matrix	35
3.2.2. Chromaticity	37
3.3. Optics Measurements	38
3.3.1. Turn-by-Turn Data	38
3.3.2. Chromaticity	39
4. Decapolar Fields	41
4.1. Introduction	41
4.1.1. Motivation	41
4.1.2. Decapolar Correctors	43
4.2. Response of correctors	45
4.3. Bare Chromaticity	47
4.4. Chromatic Amplitude Detuning	49
4.5. Accounting for Decay	51

4.6. Resonance Driving Terms	55
4.6.1. Decapolar Contribution	56
4.6.2. Higher Order Contributions	59
4.6.3. Lower Order Contributions	59
4.7. Impact of Decapolar Fields	67
4.7.1. Large RDT	67
4.7.2. Corrections	67
5. Higher Order Fields	71
5.1. Introduction	71
5.2. Chromaticity	72
5.2.1. Measurement Procedure	72
5.2.2. Performed Measurements	76
5.2.3. NL-CHROMATICITY MODEL	80
5.3. First Measurement of Dodecapole RDTs	81
5.4. CONCLUSIONS AND OUTLOOK	81
6. Skew Octupolar Fields	83
6.1. Correction of skew octupole Fields at Top Energy	83
6.2. Correction of Skew Octupole Fields at Injection Energy	84
6.3. Skew Octupolar Fields from Landau Octupoles	84
A. Hamiltonians and Transfer Maps	85
A.1. Hamiltonians of Elements	85
A.2. Transfer Maps	86
A.2.1. Generic Effective Hamiltonian of Two Elements	86
A.2.2. Transfer Map of Two Sextupoles	89
A.2.3. Transfer Map of a Sextupole and Octupole	91
A.2.4. Transfer Map of a Skew Quadrupole and Octupole	92
B. Chromatic Amplitude Detuning	93
B.1. Expression	93
B.2. Derivations	94
B.2.1. Principle	94
B.2.2. Sextupole	95
B.2.3. Octupole	96
B.2.4. Decapole	97
B.2.5. Dodecapole	98
B.3. PTC Validation	99
C. Resonance Driving Terms	101
C.1. Expressions	101

Contents

C.2. Frequency Spectrum Lines	102
C.3. Amplitude, Resonances and Lines	104
Bibliography	111
List of Publications	117

Glossary

Nomenclature

AC-Dipole Dipole magnet generating a variable oscillating field. Used to force beam oscillations for optics measurements .

Aperture Maximum physical transverse size the beam can take in the accelerator without suffering losses.

ATS Factor Equivalent to the ratio of the virgin β -function to the β -function used in the current ATS scheme, at the edge of the arc.

Beta-function Variable of the twiss-parameters: β as a function of the longitudinal position s . Related to the transverse beam size: $\sigma(s) = \sqrt{\epsilon \cdot \beta(s)}$.

BPM Beam Position Monitor, gives the transverse position of the beam.

Chromaticity Tune change with momentum offset. Usually denoted as three orders: Q' , Q'' and Q''' .

Coupling Correlation between the motion of particles in horizontal or vertical plane to the other. Strong coupling negatively impacts the optics and is usually avoided .

Crosstalk Interferences between two electronic circuits.

Dipole Magnets with two poles, responsible for bending the particles in the accelerator..

Dispersion Change of orbit with momentum offset, mainly in the horizontal plane, created by the dipoles.

DOROS Low noise BPM. Currently can't be used with other BPMs due to synchronization issues.

Dynamic Aperture Maximum stable aperture. Above that size, the particles become unstable and become lost.

Glossary

Emittance (ϵ) Unit describing the beam in phase space. A low emittance indicates a beam with a small momentum offset and confined to a small distance.

Landau Octupole Octupoles that introduce a spread in the beam, making it more stable.

LBDS LHC Beam Dump System.

Orbit Feedback System responsible for acquisition and correction of the orbit.

Rigid Waist Shift Doing a waist shift by powering all the triplets at once. No individual trim.

Waist Location where the β -function is at its minimum in an IP. β^* refers to β_{waist} .

Waist Shift Changing the waist to have $\beta^* = \beta_{IP}$.

Acronyms

LHC Large Hadron Collider.

Symbols

action Action used as coordinate blabla.

1

Introduction

1.1. Motivation

1.2. Thesis Outline

1.3. Particle Accelerators and CERN

1.3.1. Particle Accelerators

GPT

The history of particle accelerators is a captivating narrative that spans over a century of scientific innovation and discovery. It is a journey that has fundamentally transformed our understanding of the universe's fundamental particles and their interactions. The concept of accelerating particles to high speeds originated in the late 19th century, with early experiments conducted by pioneers such as J.J. Thomson and Ernest Rutherford, who utilized basic devices like cathode ray tubes to propel electrons. One of the earliest breakthroughs in accelerator technology was the Cockcroft-Walton accelerator, introduced in 1932 by John Cockcroft and Ernest Walton. This pioneering device employed voltage multipliers to accelerate protons and ions, enabling the first artificial nuclear disintegration—a milestone that earned them the Nobel Prize in Physics in 1951. Building upon this achievement, the development of the synchrotron in the 1940s and 1950s by scientists like Edwin McMillan and Vladimir Veksler marked a significant stride. Synchrotrons harnessed magnetic fields to bend and accelerate charged particles in circular paths, advancing the study of particle properties. A key turning point emerged with the establishment of CERN (the European Organization for Nuclear Research) in 1954, which culminated in the creation of the Proton Synchrotron (PS) in 1959. This marked the emergence of a powerful era in accelerator science, enabling the discovery of novel particles and laying the

1. Introduction

groundwork for the formulation of the Standard Model of particle physics. Throughout the 1960s and 1970s, the advent of bubble chambers and bubble chamber detectors provided researchers with the ability to trace the paths of charged particles, leading to the revelation of various particles and their intricate interactions. Yet, the true marvel of accelerator technology came to the forefront with the construction of the Large Hadron Collider (LHC) at CERN, which commenced operation in 2008. The LHC, an awe-inspiring 27-kilometer ring of superconducting magnets, propels protons and heavy ions to velocities nearing the speed of light. The LHC's monumental achievement—the discovery of the Higgs boson in 2012—marked a crowning moment in particle physics, solidifying the vital role of particle accelerators in unraveling the fabric of the cosmos. As particle physicists peer into the future, the quest continues. Concepts such as linear colliders and advanced circular colliders are on the horizon, promising to delve even deeper into the enigmatic realm of fundamental particles and the forces that govern them. The history of particle accelerators underscores the profound human endeavor to explore the most intricate mysteries of the universe, revealing the intricate dance of particles that shape the cosmos and expanding the horizons of human knowledge.

1.3.2. The CERN Complex

GPT The CERN complex, located near Geneva, Switzerland, is a prominent center for particle physics research. Its centerpiece is the Large Hadron Collider (LHC), the world's largest particle accelerator with a 27-kilometer circumference. Here, protons and heavy ions are accelerated to near light speed and collide at various points for fundamental particle studies. Surrounding the LHC are significant particle detectors, including ATLAS, CMS, ALICE, and LHCb, designed to capture and analyze particles generated during these collisions. CERN also includes linear accelerators, the Proton Synchrotron (PS), Super Proton Synchrotron (SPS), and Antiproton Decelerator (AD), contributing to particle acceleration and antimatter research. Alongside these facilities, CERN houses the Theoretical Physics Department, where theorists collaborate with experimentalists. With research, administrative buildings, laboratories, and workshops, CERN provides a comprehensive environment for scientific exploration. Its history, including the 2012 discovery of the Higgs boson, underscores its importance in advancing particle physics and highlighting international scientific cooperation.

1.3.3. The Large Hadron Collider

The Large Hadron Collider (LHC), is a circular particle accelerator primarily designed to collide protons for fundamental particle physics research. It can, occasionally over the year, also collide ions such as oxygen or lead for specifics studies. At the time of writing, in 2024, it holds several records, such as being the largest and most powerful accelerator in the world. The LHC is composed of two beams pipes, being able to accelerate two particle beams from an injection energy of 450GeV to an energy of 6,800GeV, before colliding them in four detectors: ATLAS, CMS, Alice and LCHb.

Well publicized, the LHC is often depicted via its superconducting dipole magnets, housed in a blue cryostat, aimed at cooling the coils. Fig. 1.1 shows a 3D cut of such magnets. The LHC is in majority composed of those *main* dipoles, as it holds 1,232 of them, being each about 14 meters long. Superconducting materials like Niobium-Titanium (NbTi) are utilized, as conventional materials such as copper would melt under the current strain. There are indeed around 12,000 amperes supplied to generate the magnetic fields necessary for bending the trajectory of the particles. Those particles travel at nearly the speed of light (more precisely, 99.9999905% of it), effectively going around the tunnel about 11,200 times per second.

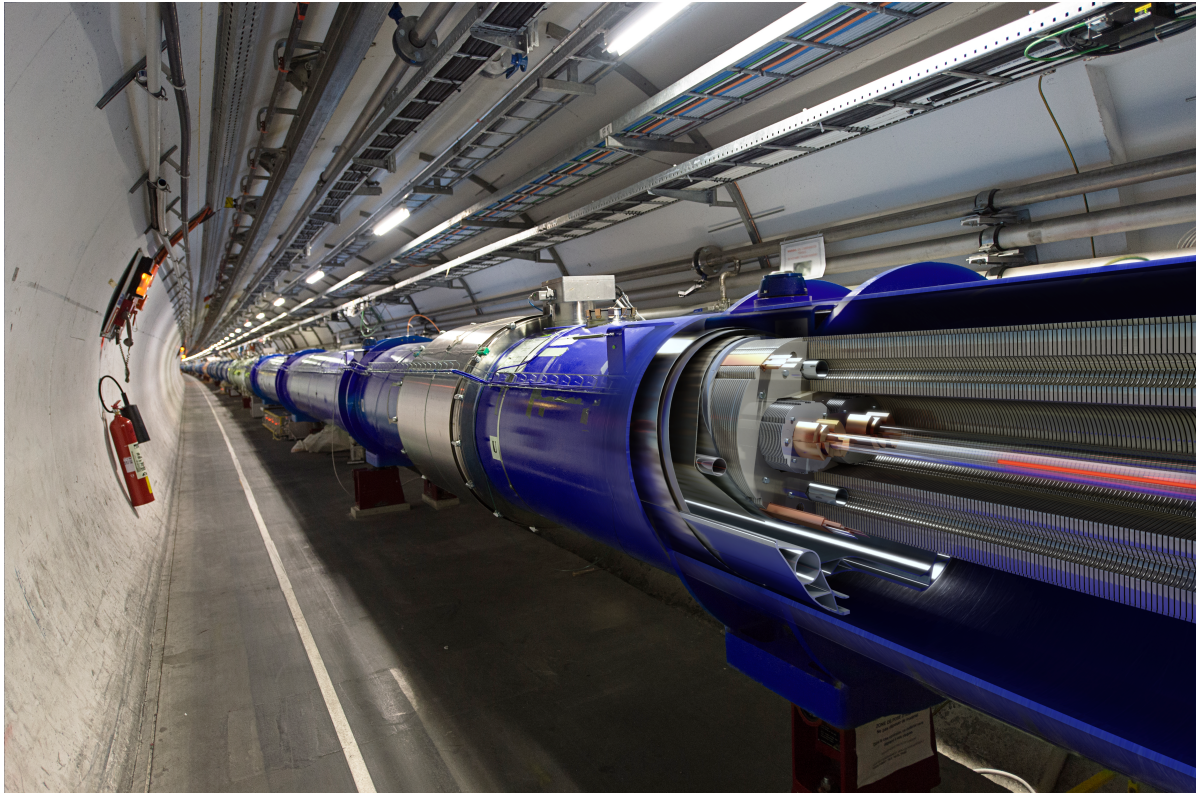


Figure 1.1.: 3D cut of a main LHC dipole [1]. Both beam pipes can be seen surrounded by the coils, strongly clamped by the yokes.

Straight Sections and Arcs The LHC is not a perfect circle. It is indeed composed of four *straight* sections, called the *Interaction Regions* (IPs) where detectors or instrumentation are placed. Connecting those sections, the *arcs* are where the majority of the magnets are placed, housing dipoles, quadrupoles, sextupoles, octupoles and their respective correctors. Fig. 1.2 shows how the instrumentation, detectors and arcs are distributed along the ring.

1. Introduction

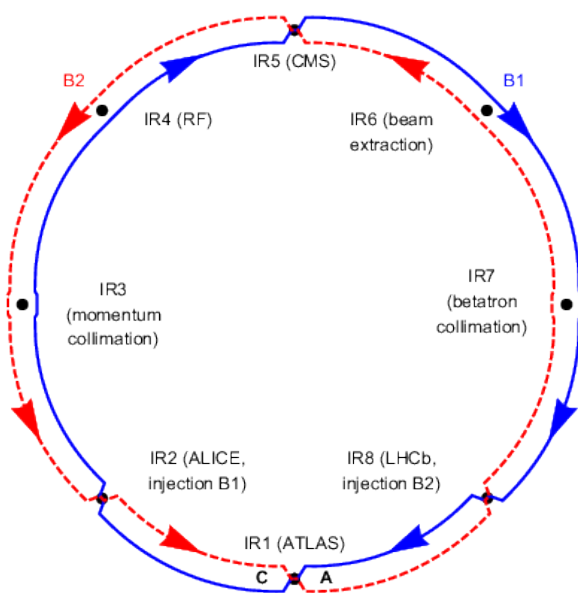


Figure 1.2.: Schematic of the LHC layout.

Arc Cells Each arc is made up of 23 cells. Magnets are organized in a standard FoDo structure (see 2.3.2), as shows Fig. 1.3. *Dipoles* are responsible for bending the trajectory of the particles. Their associated correctors, the orbit correctors, mitigate any possible drift in path. *Quadrupoles* are used to control the beam size along the ring. Their effect is focusing in one plane and defocusing in the other. Their associated correctors control the oscillations of the beam (see tune, 2.3.2) and possible field imperfections. *Sextupoles* correct chromaticity, being a misfocus from quadrupoles due to particles having a different momentum than the reference particle. *Octupoles* are used to stabilize the beam by introducing Landau Damping [2]. The associated correctors correct higher order chromaticity effects as well as amplitude dependant tune shifts. *Decapoles* correctors aim at correcting even a higher chromaticity order.

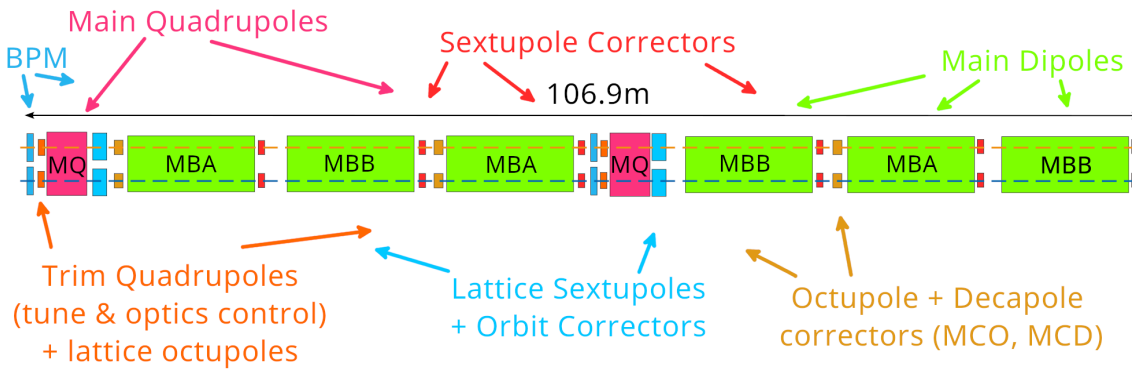


Figure 1.3.: Schematic of an LHC Arc cell [3].

Parameters

optics, pilot bunches

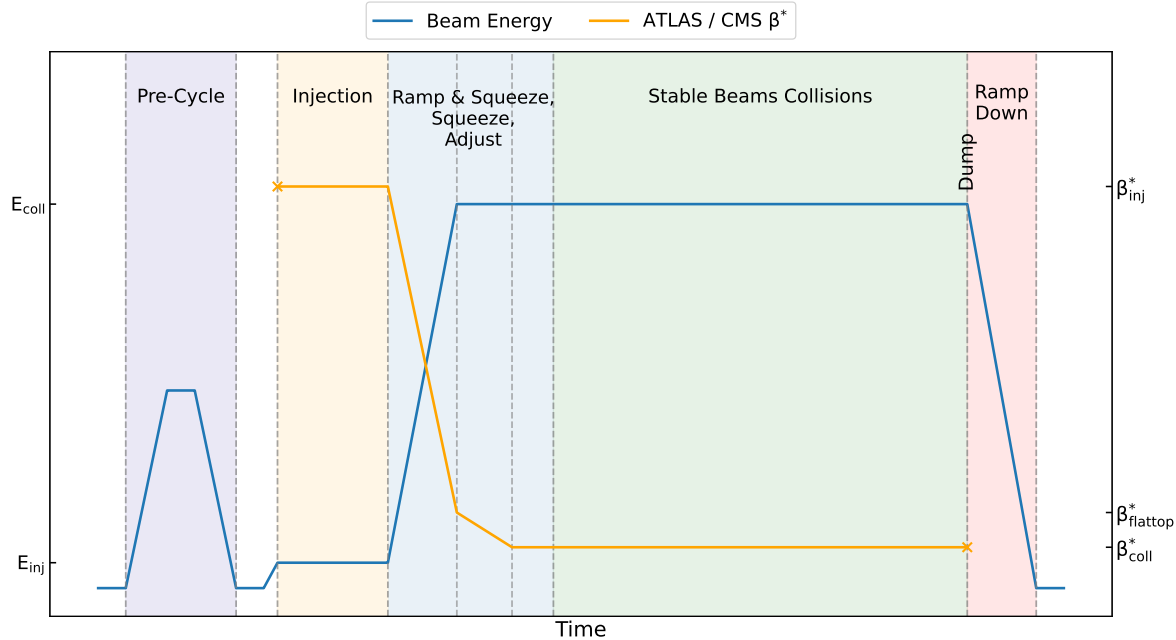


Figure 1.4.: Simplified illustration of a standard LHC cycle. Courtesy of Félix Soubélet [4]

1. Introduction

Harmonics and Field Errors

Real-life magnets never have a single field as one would like. Instead, so called *allowed harmonics* exist due to the geometry of the coil. As such, the main dipoles of the LHC can exhibit fields similar to sextupoles, decapoles, decatetrapoles and so on [5]. Manufacturing imperfections also add fields errors outside of the scope of the allowed ones. Dipoles are indeed found to generate octupolar field errors.

During the design of the LHC, the main dipoles have been identified to generate significant field errors. Magnetic measurements of those various fields were thus taken and magnetic tables built based on real-life magnets nowadays installed in the machine. Those magnetic tables, computed for each LHC configuration by WISE [cite](#) are used by simulation softwares. Predictions of field errors and compensating strength for the correctors is computed by the Field Description for the LHC (*FiDeL*, [6]). FiDeL is used in the LHC control system in operation to steer the LHC.

1.4. Tools and Softwares

Concepts of Accelerator Physics

1. Dynamic Aperture

2.1. Introduction

2.2. Magnetic Fields

2.2.1. Nomenclature

Several notations coexist to denote magnetic fields. In this thesis, the *European Convention* [7] is used for field indices, as shown in Tab. 2.1. MAD-X, and MAD-NG, however, use the *American Convention*.

Multipole	MAD-X	Index	Normalized Strength
Dipole	0	1	K_1
Quadrupole	1	2	K_2
Sextupole	2	3	K_3
Octupole	3	4	K_4
Decapole	4	5	K_5
Dodecapole	5	6	K_6
Decatetrapole	6	7	K_7

Table 2.1.: Relation between field indices and multipoles.

As such, unless explicitly stated, quantities such as the magnetic strength b and normalized strength K will be expressed with this notation.

2.2.2. Multipole Expansion

A 2 dimension magnetic field in the planes x and y can be described as a sum of the normal and skew field gradients \mathcal{B} and \mathcal{A} with multipoles of order n , given by [8]:

$$B_y + iB_x = \sum_{n=1}^{\infty} (\mathcal{B}_n + i\mathcal{A}_n) (x + iy)^{n-1} \quad (2.1)$$

An ideal magnet would produce either a sole normal or skew field. However, this is not applicable to real-life magnets that are imperfect, due to design and manufacturing constraints. Field errors are thus introduced, relative to the main field of the ideal 2N-pole magnet at a reference radius r_{ref} [7], as shown in Eq. (2.2). The coefficients of the normal and skew relative field errors, referred to as a_n and b_n , are dimensionless but often given in units of 10^{-4} .

$$B_y + iB_x = \begin{cases} \mathcal{B}_N \cdot \sum_{n=1}^{\infty} (b_n + ia_n) \left(\frac{x+iy}{r_{ref}}\right)^{n-1}, & \text{for normal magnets} \\ \mathcal{A}_N \cdot \sum_{n=1}^{\infty} (b_n + ia_n) \left(\frac{x+iy}{r_{ref}}\right)^{n-1}, & \text{for skew magnets} \end{cases} \quad (2.2)$$

The normal and skew field components of order n for an imperfect 2N-pole magnet is thus given by the following equation:

$$\begin{aligned} \mathcal{B}_n &= \mathcal{B}_N \cdot \frac{b_n}{r_{ref}^{n-1}}, \\ \mathcal{A}_n &= \mathcal{A}_N \cdot \frac{a_n}{r_{ref}^{n-1}}. \end{aligned} \quad (2.3)$$

The unit of the field is relative to the multipole order n : [Tm $^{1-n}$].

2.2.3. Beam Rigidity and Normalization

Beam Rigidity

The beam rigidity refers to the resistance of a particle moving through the accelerator to the bending applied by the magnetic fields. It is derived from the Laurentz force [7] and relates the magnetic field B , the radius of curvature ρ to the momentum p and charge q of the particle:

$$B\rho = \frac{p}{q} \quad (2.4)$$

It is of interest when designing an accelerator to set the maximum field as well as the required radius of curvature for a specific momentum and particle. An interesting metric of an accelerator is also its *filling factor*, or percentage of dipoles in the machine. It can be calculated via the radius of curvature: $f = \rho/r$. A low filling factors means more space for other magnets, collimators, beam instrumentation, etc.

Field Normalization

The Beam Rigidity is also used as a way to normalize magnetic field strengths in particle accelerators where the momentum of the particle changes (i.e. acceleration). Normalized Normal and Skew components K_n and J_n are given by [8]:

$$\begin{aligned} K_n &= \frac{q}{p}(n-1)!\mathcal{B}_n, \\ J_n &= \frac{q}{p}(n-1)!\mathcal{A}_n. \end{aligned} \quad (2.5)$$

2.2.4. Hamiltonian

The Hamiltonian describing the motion for the transverse planes of a given multipole or order n is given by [9–11]:

$$\begin{aligned} H &= \frac{q}{p}\Re\left[\sum_{n>1}(\mathcal{B}_n + i\mathcal{A}_n)\frac{(x+iy)^n}{n}\right] \\ &= \Re\left[\sum_{n>1}(K_n + iJ_n)\frac{(x+iy)^n}{n!}\right]. \end{aligned} \quad (2.6)$$

Quite often, when studying the effect of a magnet on the beam, only one component is required, and the sum can thus be dropped. The normal and skew fields can also be isolated in order to consider their effect only:

$$\begin{aligned} N_n &= \frac{1}{n!}K_n\Re[(x+iy)^n] \\ S_n &= -\frac{1}{n!}J_n\Im[(x+iy)^n]. \end{aligned} \quad (2.7)$$

2.3. Coordinate Systems

In circular accelerators, particle dynamics are represented using a traveling coordinate system. A reference orbit is determined by the lattice and its magnet strengths, forming the *optics*. In the case of a synchrotron, like the LHC, where the particles return to their original location after some turns, the reference orbit is also called the closed orbit.

2.3.1. Frenet-Serret System

The Frenet-Serret coordinate system moves along the ring on the reference orbit. The coordinates are then transverse: x and y , and longitudinal in the direction of travel: s . Figure 2.1 shows those coordinates.

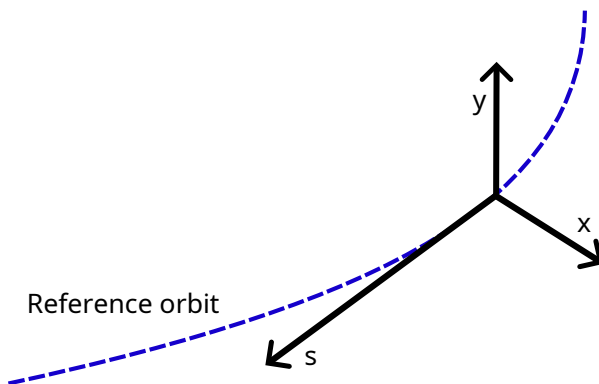


Figure 2.1.: Frenet-Serret coordinate system, commonly used in accelerator physics. The system moves along the reference orbit.

This coordinate system is widely used to simply describe either an element's or a particle's position in the accelerator. Without any explicit mention, those are coordinates used in this thesis. It is frequent to use the variable z to refer to either x or y in equations.

2.3.2. Linear Lattice

Courant-Snyder Parameters

A circular accelerator is composed of many multipoles of different orders. A basic design only requires dipoles and quadrupoles in order to operate. Dipoles are used to bend the particles in order to form the ring, whereas quadrupoles are used to focus the beam to a focal point, similar to light optics. Those elements can be arranged in a particular order, to form a FoDo cell. Such cells present an alternating

placement of focusing and defocusing quadrupoles with dipoles in between, as shown in Fig.2.2, and are usually repeated many times along the ring.

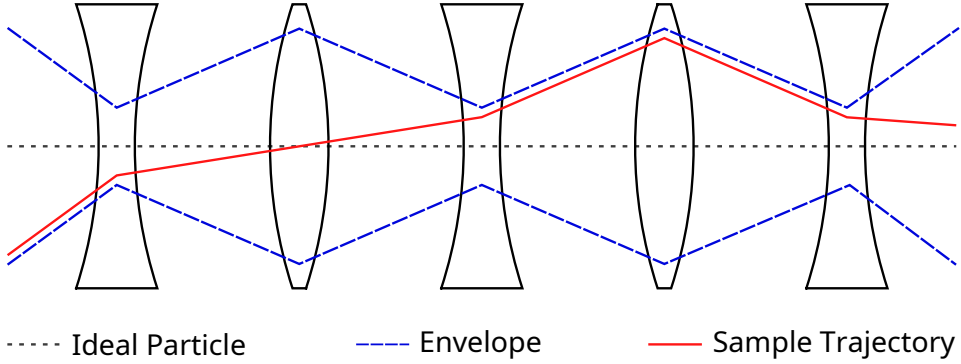


Figure 2.2.: Line composed of FoDo cells, a basic cell present in most accelerators, composed of a Focusing and a Defocusing quadrupole. The envelope is a factor of the β -function and the action J .

A lattice composed of only dipoles and quadrupoles, is referred to as a *linear* lattice. In a synchrotron, a circular particle accelerator, particles undergo transverse and longitudinal oscillations. As such, particles do not go back to their initial position before a certain number of turns. Taking into account those oscillations, the phase-space ellipse of a particle at a position s in the ring can be described with a new system: the Courant-Snyder parameters, also known as Twiss parameters or the *optics functions* [12], as shown in Fig. 2.3.

J , the action, an invariant of motion at a given energy, is related to the other quantities by:

$$J_z = \frac{1}{2}(\gamma_z \cdot z^2 + 2\alpha_z p_z \cdot z + \beta_z p_z^2). \quad (2.8)$$

The action can be related to the area in phase space, called the emittance: $\epsilon = 2J$. As the β parameter varies along the ring, it is referred to as the β -function and is related to the amplitude of the oscillations. Thus, the smaller is the β -function, the smaller is also the envelope of the beam. The number of oscillations per turn is called the *tune*, and is closely related to the β -function:

$$Q_{x,y} = \frac{1}{2\pi} \oint \frac{1}{\beta_{x,y}(s)} ds. \quad (2.9)$$

It is common to express the position of a particle using *action-angle* variables, allowing to switch between the Courant-Snyder parameters and the Frenet-Serret system:

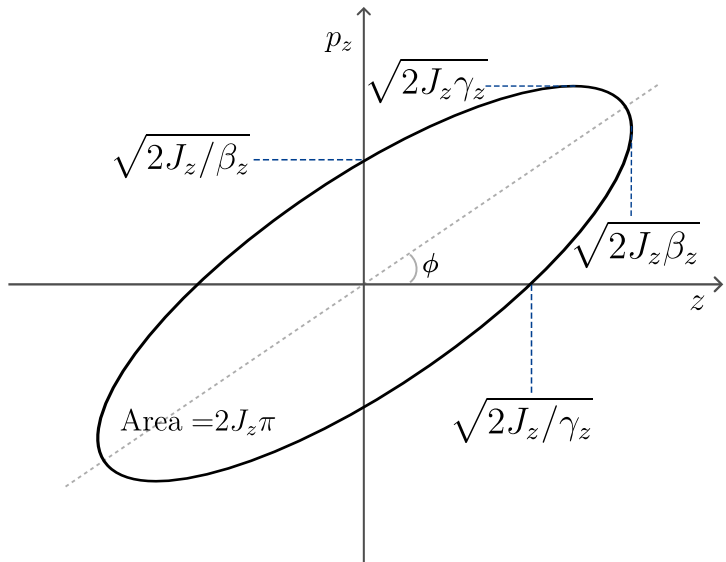


Figure 2.3.: Phase-space ellipse of a linear machine, parametrized by the Courant-Snyder parameters α , β and γ .

$$\begin{aligned} z &= \sqrt{2J_z\beta_z} \cos \phi_z \\ p_z &= -\sqrt{\frac{2J_z}{\beta_z}} (\sin \phi_z + \alpha_z \cos \phi_z). \end{aligned} \quad (2.10)$$

Normalized Coordinates

In order to simplify the description of the linear motion in a ring, a transformation can be applied to the previously seen coordinates. Figure Fig. 2.4 shows a phase-space described in both coordinates. The new coordinates, \hat{z} , and \hat{p}_z , are then expressed as factors of the α and β functions:

$$\begin{pmatrix} \hat{z} \\ \hat{p}_z \end{pmatrix} = \begin{pmatrix} \frac{1}{\sqrt{\beta_z}} & 0 \\ \frac{\alpha_z}{\sqrt{\beta_z}} & \sqrt{\beta_z} \end{pmatrix} \begin{pmatrix} z \\ p_z \end{pmatrix}. \quad (2.11)$$

This allows to describe the motion as a simple rotation, the new coordinates being only dependent on the invariant J_z and the phase ϕ_z :

$$\begin{aligned} \hat{z} &= \sqrt{2J_z} \cos (\phi_z), \\ \hat{p}_z &= \sqrt{2J_z} \cos (\phi_z). \end{aligned} \quad (2.12)$$

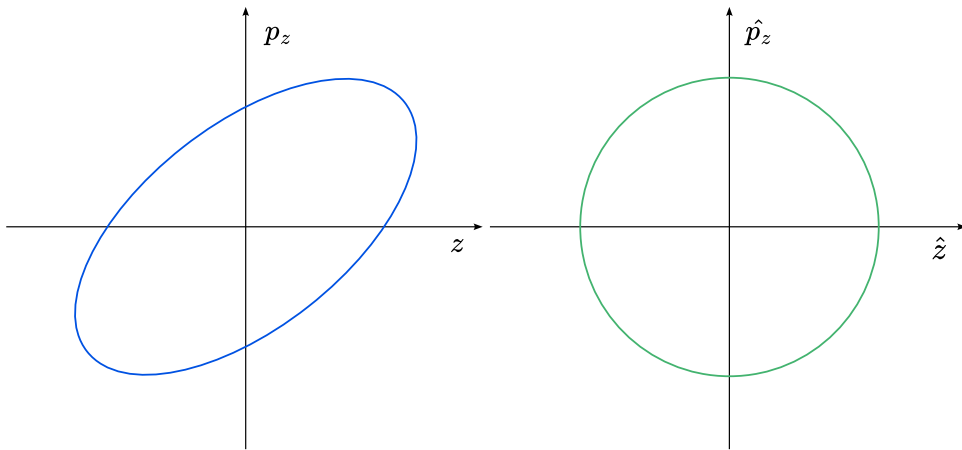


Figure 2.4.: Phase space described in both regular and normalized coordinates

Linear Transfer Maps

It is possible to describe the final position of a particle after going through an element via *transfer maps*. In linear optics, such linear maps are matrices. Those maps are symplectic, meaning they preserve the phase-space area. For a matrix M and positions z at the initial location and s , the general formula reads [13]:

$$\begin{pmatrix} z \\ z' \end{pmatrix}_s = M \cdot \begin{pmatrix} z \\ z' \end{pmatrix}_0 \quad (2.13)$$

This formalism assumes that the magnetic field is constant along the element in the longitudinal direction. Basic elements such as drifts, dipoles, quadrupoles can then be described by a simple 2×2 matrix:

$$M_{drift} = \begin{pmatrix} 1 & L \\ 0 & 1 \end{pmatrix}, \quad (2.14)$$

$$M_{dipole} = \begin{pmatrix} \cos(L/\rho) & \rho \sin(L/\rho) \\ -1/\rho \sin(L/\rho) & \cos(L/\rho) \end{pmatrix}, \quad (2.15)$$

$$M_{focusing quad.} = \begin{pmatrix} \cos(\sqrt{k_2}L) & 1/\sqrt{k_2} \sin(\sqrt{k_2}L) \\ -\sqrt{k_2} \sin(\sqrt{k_2}L) & \cos(\sqrt{k_2}L) \end{pmatrix}, \quad (2.16)$$

$$M_{\text{defocusing quad.}} = \begin{pmatrix} \cosh(\sqrt{|k_2|}L) & 1/\sqrt{|k_2|}\sinh(\sqrt{|k_2|}L) \\ \sqrt{|k_2|}\sinh(\sqrt{|k_2|}L) & \cosh(\sqrt{|k_2|}L) \end{pmatrix}, \quad (2.17)$$

where L is the length of the element, ρ the radius of curvature of the orbit and k_2 the normalized strength of quadrupoles. In the case of quadrupoles, a focusing matrix should be used in the horizontal plane for focusing quadrupoles, where defocusing matrices should be used in the vertical plane. The opposite goes for defocusing quadrupoles.

Transfer matrices can be combined together to describe a larger group of elements, as the FoDo cell seen previously. Its transfer matrix can then be expressed as:

$$M_{\text{FoDo}} = M_{\text{focusing quad.}} \cdot M_{\text{drift}} \cdot M_{\text{defocusing quad.}} \cdot M_{\text{drift}}. \quad (2.18)$$

For a closed machine, a full revolution can be described by a so-called *one-turn map*, being the transfer matrix of the whole machine, denoted \mathcal{M} . Such a map can potentially contain thousands of elements.

Symplecticity An important property of any transformation is that they need to be symplectic. A symplectic transformation preserves the volume in phase space.

2.3.3. Non-Linear Lattice

So far, Courant-Snyder parameters were a good way to describe the distribution of positions and velocities of particles in the transverse plane. One caveat of using this formalism is that it is restrained to linear optics and does not describe non-linear beam dynamics such as resonances or the effects arising from an arrangement of several multipoles together.

Lie Algebra

One way to describe non-linear effects is to introduce Lie Algebra [14], a powerful algebra able to describe transformations, symmetries and their associated conserved quantities.

The Lie algebra is a vector space, denoted \mathfrak{g} , equipped with a binary operation called the *Lie bracket* and denoted $[x, y]$ for two vectors x and y . Any vector space equipped with a Lie bracket (or commutator) satisfying the following conditions is called a Lie algebra:

- Bilinearity:

$$\begin{aligned} [ax + by, z] &= a[x, z] + b[y, z], \\ [z, ax + by] &= a[z, x] + b[z, y], \quad \forall x, y, z \in \mathfrak{g} \text{ and } a, b \text{ scalars} \end{aligned} \quad (2.19)$$

- Alternativity:

$$[x, x] = 0, \quad \forall x \in \mathfrak{g} \quad (2.20)$$

- Anticommutativity:

$$[x, y] = -[y, x], \quad \forall x, y \in \mathfrak{g} \quad (2.21)$$

- The Jacobi identity:

$$[x, [y, z]] + [y, [z, x]] + [z, [x, y]] = 0, \quad \forall x, y, z \in \mathfrak{g} \quad (2.22)$$

The *Lie bracket*, plays a central role in the Lie algebra. It describes how dynamical variables evolve under infinitesimal symplectic transformations.

Poisson Brackets

To create a Lie algebra, an operation satisfying the previous conditions needs to be found. In accelerator physics, *Poisson brackets* are chosen [14, 15]. Poisson brackets are used to describe continuous symmetries, conserved quantities, and the evolution of the dynamical variables in the system.

Let's consider position and momentum coordinates $q_1 \cdots q_n$ and $p_1 \cdots p_n$ of a 2n-dimensional phase space. Usually, those would be x, y, p_x and p_y for transverse coordinates. The Poisson brackets of two functions f and g is then defined by:

$$[f, g] = \sum_{i=1}^n \frac{\partial f}{\partial q_i} \frac{\partial g}{\partial p_i} - \frac{\partial f}{\partial p_i} \frac{\partial g}{\partial q_i}. \quad (2.23)$$

The evolution of coordinates and momenta in time is described by Hamilton's equations of motion, which can be naturally expressed with Poisson brackets:

$$\begin{aligned} \frac{dq_i}{dt} &= \frac{\partial H}{\partial p_i} = [q_i, H] \\ \frac{dp_i}{dt} &= -\frac{\partial H}{\partial q_i} = [p_i, H]. \end{aligned} \quad (2.24)$$

Lie Operator

Given a function f , a differential operator called *Lie operator* is defined, and is closely related to the previously seen Poisson bracket:

The action of this operator on a function g is equivalent to the Poisson brackets, as in:

$$:f:g = [f, g]. \quad (2.26)$$

A particular power series of this Lie operator can now be defined, called *Lie transformation*:

$$\begin{aligned} e^{:f:}g &= \sum_{l=0}^{\infty} \frac{1}{l!} :f:^l g \\ &= g + [f, g] + \frac{1}{2!}[f, [f, g]] + \dots . \end{aligned} \quad (2.27)$$

Non-Linear Transfer Maps

As introduced in 2.3.2, the dynamics of a particle beam in a circular accelerator can be described by *transfer maps*. A symplectic *One Turn Map* \mathcal{M} that includes N non-linear elements is defined [14] as:

$$\mathcal{M} = e^{:h_N:} \cdot e^{:h_{N-1}:} \cdots e^{:h_1:} \cdot \mathcal{R} \quad (2.28)$$

where \mathcal{R} is a matrix describing the linear motion over one turn and the h_i terms representing the Hamiltonian of each non-linear elements of the machine. Via the Baker-Campbell-Hausdorff (BCH) theorem [16, 17], previous Lie transformations can be combined and simplified via Eq. (2.29) and Eq. (2.30). Further orders can be found and computed via [17].

$$e^{:h_1:} \cdot e^{:h_2:} = e^{:h:} \quad (2.29)$$

with

$$\begin{aligned} h &= h_1 + h_2 && \Rightarrow 1^{\text{st}} \text{ order} \\ &+ \frac{1}{2}[h_1, h_2] && \Rightarrow 2^{\text{nd}} \text{ order} \\ &+ \frac{1}{12}[h_1, [h_1, h_2]] - \frac{1}{12}[h_2, [h_1, h_2]] && \Rightarrow 3^{\text{rd}} \text{ order} \\ &+ \dots . \end{aligned} \quad (2.30)$$

The one turn map is thus expressed as a single Lie transformation:

$$\mathcal{M} = e^{\cdot h \cdot} \cdot \mathcal{R}. \quad (2.31)$$

In most cases, where the non-linear perturbations are small, the above series converges quickly and only the two first terms of Eq. (2.30) are used [18]. The resulting expression is then more elegant, being a simple sum of the Hamiltonians of the N non-linear elements:

$$\mathcal{M} = e^{\cdot h_1 + h_2 + \dots + h_N \cdot} \cdot \mathcal{R}. \quad (2.32)$$

It is though to be noted that in this thesis experimental measurements show the evidence of higher order contributions. In order to fully understand the combined effect of multipoles, the BCH expansion needs to be expended further than the first two terms.

something about -L:H:

Normal Form

As non-linearities are introduced in the machine, the phase-space becomes distorted, resulting in J_z no longer being an invariant of motion. The previously seen normalization does not work anymore and the phase-space is no longer a simple circle. A new normalization is then introduced, called the *normal form*, with complex coordinates ζ , depending on new action and angle coordinates I_z and ψ_z :

$$\zeta_{z,\pm} = \sqrt{2I_z} e^{\mp i\psi_z}. \quad (2.33)$$

An exaggerated vision of such a phase-space in Courant-Snyder, normalized, and normal form coordinates can be seen in Fig. 2.5.

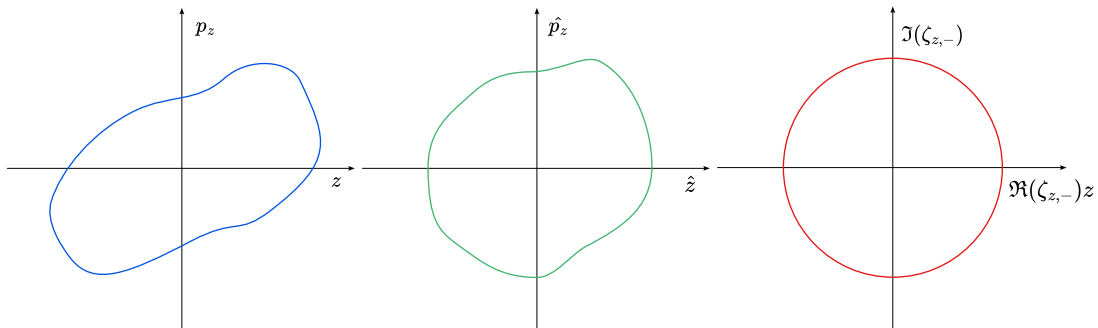


Figure 2.5.: Exaggerated phase space distorted by non-linearities described in regular, normalized and normal form coordinates.

The map defined previously in Eq. (2.31) can be rewritten in order to retrieve an invariant of motion I_z by introducing a generating function F :

$$\tilde{\mathcal{M}} = e^{:-F:} \mathcal{M} e^{:F:} \quad (2.34)$$

Such a generating function includes all the non-linearities, simplifying the calculations. Going back and forth from normalized to normal forms coordinates is then straightforward, as depicted in Fig. 2.6. The hamiltonian H is now only dependent on the action I_z .

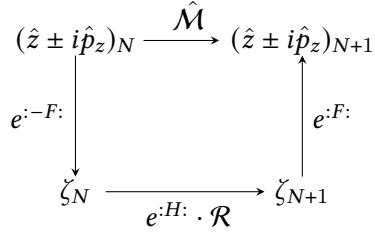


Figure 2.6.: A one turn map from turn N to N+1 solved using a generating function F , transforming to normal form coordinates ζ , applying the linear rotation R and transforming back to normalized coordinates.

The function F is defined as

$$F = \sum_{jklm} f_{jklm} \zeta_{x,+}^j \zeta_{x,-}^k \zeta_{y,+}^l \zeta_{y,-}^m, \quad (2.35)$$

where f_{jklm} are the so-called Resonance Driving Terms (RDTs). The summation $jklm$ is done over all the combinations of j, k, l and m with $j + k + l + m = n$ for a multipole of order n , as shown in Eq. (2.36):

$$\sum_{jklm} = \sum_{j=0}^n \sum_{k=0}^n \sum_{l=0}^n \sum_{m=0}^n ; \quad j + k + l + m = n. \quad (2.36)$$

The expression of the resonance driving terms is given by the global hamiltonian term h_{jklm} by

$$f_{jklm} = \frac{h_{jklm}}{1 - e^{i2\pi[(j-k)Q_x + (l-m)Q_y]}}, \quad (2.37)$$

where this coefficient is a summation over the hamiltonian terms of elements w in the lattice,

The expression of $h_{w,jklm}$ is itself derived from the general hamiltonian of Eq. (2.6) by applying a binomial expansion on the coordinates [11] as shows Eq. (2.39). Derivations and more information on resonance driving terms can be found in Appendix C.

$$h_{w,jklm} = -\Re \left[\frac{K_{w,n} + iJ_{w,n}}{j!k!l!m!2^{j+k+l+m}} t^{l+m} \beta_{w,x}^{\frac{j+k}{2}} \beta_{w,y}^{\frac{l+m}{2}} \right] \quad (2.39)$$

Transforming from the normal form coordinates back to the original normalized coordinates can be done using the right side of Fig. 2.6. Which is written, to second order, as:

$$\begin{aligned} h_z^\pm &= e^{\dot{F}} \cdot \zeta_z^\pm \\ &\simeq \zeta_z^\pm + [F, \zeta_z^\pm] + \frac{1}{2!} [F, [F, \zeta_z^\pm]]. \end{aligned} \quad (2.40)$$

Using this equation to the first order and Eq. (2.33), the normalized coordinates can be expressed after N turns in Eq. (2.41).

$$\begin{aligned} (x - ip_x)(N) &= \sqrt{2I_x} e^{i(2\pi Q_x N + \psi_{x_0})} - \\ &\quad 2i \sum_{jklm} j f_{jklm} (2I_x)^{\frac{j+k-1}{2}} (2I_y)^{\frac{l+m}{2}} e^{i[(1-j+k)(2\pi Q_x N + \psi_{x_0}) + (m-l)(2\pi Q_y N - \psi_{y_0})]} \\ (y - ip_y)(N) &= \sqrt{2I_y} e^{i(2\pi Q_y N + \psi_{y_0})} - \\ &\quad 2i \sum_{jklm} l f_{jklm} (2I_x)^{\frac{j+k}{2}} (2I_y)^{\frac{l+m-1}{2}} e^{i[(k-j)(2\pi Q_x N + \psi_{x_0}) + (1-l+m)(2\pi Q_y N - \psi_{y_0})]}. \end{aligned} \quad (2.41)$$

It is to be observed that some f_{jklm} terms will not contribute to the motion of the particle in a given plane due to the dependence on j or l .

2.4. Examples of Maps

It is important to remember that two expansions are used when creating non linear transfer maps. When referring to the order of a map, it is the order of the BCH formula, used to combine Hamiltonians, that is referred to. The Lie transformation to transport the coordinates themselves is usually only taken to the first order.

2.4.1. Non-Linear Transfer of a Single Sextupole

Here, we are interested on the effect of a single sextupole on the regular frenet-serret coordinates x, y, p_x and p_y . Let's consider a sextupole with strength K_3 and a normal field,

$$H_3 = \frac{1}{6}K_3(x^3 - 3xy^2). \quad (2.42)$$

A transfer map, from longitudinal coordinate s_0 to s_1 , consisting of only this element is the following:

$$\begin{pmatrix} x \\ p_x \\ y \\ p_y \end{pmatrix}_{s_1} = e^{L:H_3:} \begin{pmatrix} x \\ p_x \\ y \\ p_y \end{pmatrix}_{s_0}, \quad (2.43)$$

where L is the length of the multipole. Using Eq. (2.27) to expand the Lie transformation to the first order, it can be rewritten as

$$\begin{aligned} e^{L:H_3:}x &= x + [L \cdot H_3, x], \\ e^{L:H_3:}p_x &= p_x + [L \cdot H_3, p_x], \\ e^{L:H_3:}y &= y + [L \cdot H_3, y], \\ e^{L:H_3:}p_y &= p_y + [L \cdot H_3, p_y]. \end{aligned} \quad (2.44)$$

Applying the poisson bracket of Eq. (2.23) on x or y yields 0, as neither the Hamiltonian nor x and y are dependent on p_x and p_y .

$$\begin{aligned} [L \cdot H_3, x] &= \overbrace{\frac{\partial(L \cdot H_3)}{\partial x} \frac{\partial x}{\partial p_x}}^0 - \overbrace{\frac{\partial(L \cdot H_3)}{\partial p_x} \frac{\partial x}{\partial x}}^0 + \underbrace{\frac{\partial(L \cdot H_3)}{\partial y} \frac{\partial x}{\partial p_y}}_0 - \underbrace{\frac{\partial(L \cdot H_3)}{\partial p_y} \frac{\partial x}{\partial y}}_0 \\ &= 0. \end{aligned} \quad (2.45)$$

The poisson bracket applied on p_x or p_y though evaluates to a non-zero value, as the momentum is present in $p_{x,y}$ while x, y are present in the Hamiltonian:

$$\begin{aligned}
 [L \cdot H_3, p_x] &= \frac{\partial(L \cdot H_3)}{\partial x} \frac{\partial p_x}{\partial p_x} - \underbrace{\frac{\partial(L \cdot H_3)}{\partial p_x} \frac{\partial p_x}{\partial x}}_0 + \underbrace{\frac{\partial(L \cdot H_3)}{\partial y} \frac{\partial p_x}{\partial p_y}}_0 - \underbrace{\frac{\partial(L \cdot H_3)}{\partial p_y} \frac{\partial p_x}{\partial y}}_0 \\
 &= \frac{1}{2} K_3 L (x^2 - y^2)
 \end{aligned} \tag{2.46}$$

The same method is used for p_y . The final form of the transfer map Eq. (2.43) is then the following:

$$\begin{pmatrix} x \\ p_x \\ y \\ p_y \end{pmatrix}_{s_1} = \begin{pmatrix} 1 & & & \\ & 1 + \left(\frac{1}{2p_x} K_3 L (x^2 - y^2) \right) & & \\ & & 1 & \\ & & & 1 - \left(\frac{1}{p_y} K_3 L x y \right) \end{pmatrix} \begin{pmatrix} x \\ p_x \\ y \\ p_y \end{pmatrix}_{s_0}. \tag{2.47}$$

It is not necessary to go higher than the first order, as the second order of the expansion of the Lie transformation is 0 ; p_x is indeed not present in the result of the first poisson bracket:

$$\begin{aligned}
 \frac{1}{2!} [L \cdot H_3, [L \cdot H_3, p_x]] &= \frac{1}{2!} \left[L \frac{1}{6} K_3 (x^3 - 3xy^2), \left[L \frac{1}{6} K_3 (x^3 - 3xy^2), p_x \right] \right] \\
 &= \frac{1}{2!} \left[L \frac{1}{6} K_3 (x^3 - 3xy^2), \frac{1}{2} K_3 L (x^2 - y^2) \right] \\
 &= \frac{1}{2!} \cdot 0 \\
 &= 0
 \end{aligned} \tag{2.48}$$

2.4.2. Non-Linear Transfer of Two Sextupoles

We saw previously that a single sextupole only acts as a sextupole when it is alone in the transfer map, which is expected. Let's now consider two sextupoles which hamiltonians are denoted H_1 and H_2 .

Creating a map consisting of only two sextupoles does not make much sense, as it finally results in one sextupole as their coordinates are the same. Instead, a drift is added between the two elements. The Hamiltonian of a drift of length L_D is given by [19],

$$D = -\frac{L_D}{2} (p_x^2 + p_y^2). \tag{2.49}$$

The application of the lie transformation on the canonical coordinates is then very simple, as no higher orders arise ($[D, [D, x]] = 0$):

$$\begin{aligned} e^{iD}x &= x + L_D p_x, \\ e^{iD}p_x &= p_x. \end{aligned} \quad (2.50)$$

The transfer map of such a line is then the following,

$$\mathcal{M} = e^{iZ} = e^{iH_2} \cdot e^{iD:H_1}, \quad (2.51)$$

describing the evolution of coordinates from a longitudinal position s_0 to s_1 ,

$$\begin{pmatrix} x \\ p_x \\ y \\ p_y \end{pmatrix}_{s_1} = \mathcal{M} \cdot \begin{pmatrix} x \\ p_x \\ y \\ p_y \end{pmatrix}_{s_0} \quad (2.52)$$

In order to combine those elements, the BCH formula from Eq. (2.30) is used, presented here to the third order for two elements,

$$Z = \underbrace{H_2 + H_1}_{\text{First order}} + \underbrace{\frac{[H_2, H_1]}{2}}_{\text{Second order}} + \underbrace{\frac{[H_2, [H_2, H_1]]}{12} - \frac{[H_1, [H_2, H_1]]}{12}}_{\text{Third order}} \quad (2.53)$$

First Order To the first order, the resulting effective hamiltonian is only the summation of two sextupoles.

Second Order The drift added to change the coordinates of H_1 allows the poisson bracket to evaluate to a non-zero value. Octupolar-like terms indeed appear in the effective hamiltonian. From this, it can be inferred that two sextupoles will interact together and introduce effects like amplitude detuning, second order chromaticity and RDTs. Details of the derivation can be found in Appendix A.

Third Order To the third order, even higher orders such as decapolar-like effects appear. Such effects include the third order chromaticity, chromatic amplitude detuning and RDTs.

Remark It is to be noted that while sextupoles do introduce higher-order terms, these are typically small in comparison to those brought by the actual higher-order multipoles, making them thus often negligible.

2.5. Observables

2.5.1. Dispersion

Treating a beam as a single particle having the design momentum p_0 leads to a machine with no apparent ill effect related to that momentum. However, when considering a particle beam where each particle follows a distribution in momentum, a few effects arise from this deviation, called the *momentum offset*, δ . It is defined as a relative difference to the design momentum:

$$\delta = \frac{p - p_0}{p_0}. \quad (2.54)$$

Those effects are referred to as *chromatic aberrations*. The first and most important to consider is the *dispersion*. Dispersion results from a particle with a momentum offset being deflected differently by the dipoles compared to a particle at the design momentum. Figure 2.7 shows an example of deflection.

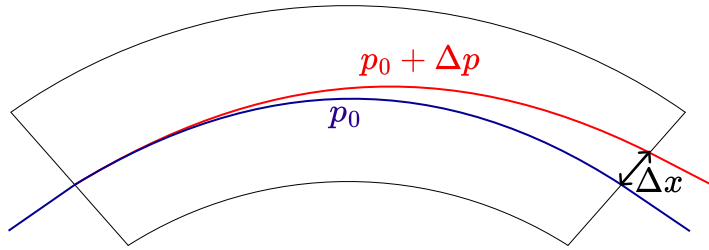


Figure 2.7.: Particles with a momentum offset will be deflected differently by dipoles. This offset in position can be described by the dispersion function.

The particle is still subject to the other properties of the lattice, but with a different orbit, described by Eq. (2.7).

$$\begin{aligned} D_x(s) &= \frac{\Delta x(s)}{\delta} \\ D_y(s) &= \frac{\Delta y(s)}{\delta} \end{aligned} \quad (2.55)$$

2.5.2. β -function

As seen previously in 2.3.2, the β -function is related to the amplitude of oscillations of the beam. Figure 2.8 shows how the β -function oscillates along the ring due to quadrupoles focusing and defocusing properties. The β -function is an important quantity found as a factor in several other observables that will be described later in this thesis.

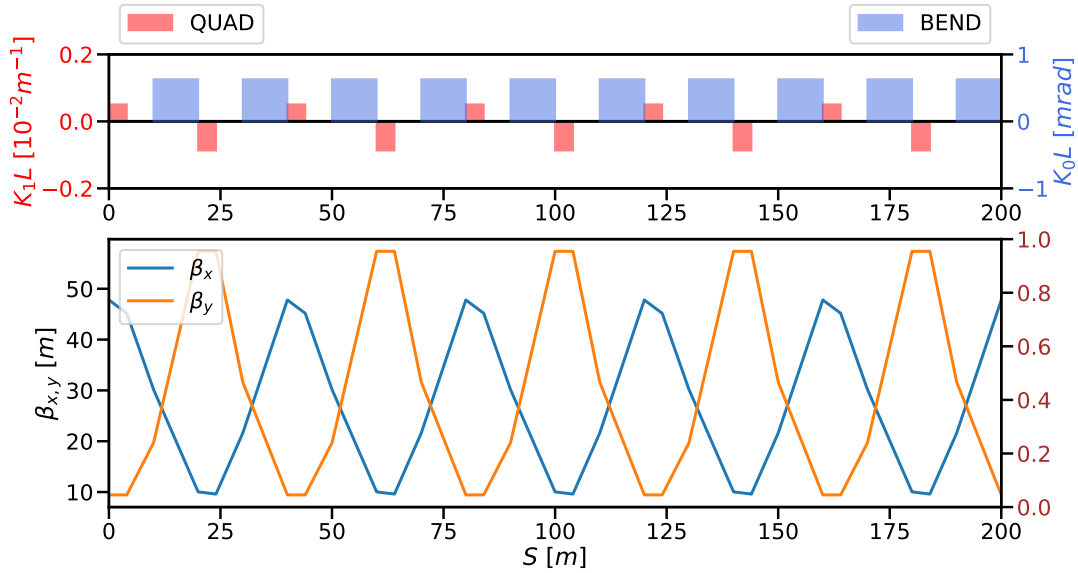


Figure 2.8.: Evolution of the β -function along the lattice. Horizontal and vertical beatings are usually opposite given the focusing and defocusing properties of quadrupoles in each plane.

A difference in β -function compared to the design leads to possibly unstable and larger beams, degrading its properties and making it harder to control. The relative difference in β -function is called the beta-beating, expressed in percents:

$$\beta\text{-beating [\%]} = \frac{\beta_z(s) - \beta_z(s)_{model}}{\beta_z(s)_{model}}. \quad (2.56)$$

2.5.3. Coupling

In a perfect scenario, the particle motion of each transverse plane is independent, or *uncoupled*. In practice, this transverse motion can be altered by some magnetic elements, giving rise to *betatron coupling* where the motion of each plane is not independent anymore. Such elements can be quadrupoles, mounted with a roll error introducing skew-quadrupolar fields, which are the main source of coupling in the LHC [4]. Field imperfections, solenoids and feed-down from higher orders can also contribute to coupling.

The resonances $Q_x + Q_y$ and $Q_x - Q_y$, called the *sum* and *difference* resonances, are mainly excited by skew quadrupoles. When coupling is present in the machine, the former may lead to unstable motion while the latter introduces an periodic exchange of emittance between the planes, keeping it stable. They can be characterized by the RDTs f_{1010} and f_{1001} .

Effects of normal multipoles start showing their skew counterpart (and vice versa) as the motion of transverse planes become coupled. This is demonstrated in Chapter 6 with skew-octupolar RDTs contributed to by normal octupoles in the presence of coupling.

2.5.4. Momentum Compaction Factor

In synchrotrons, particles with a deviation in momentum with respect to the reference particle will experience a different path length due to the bending of the dipoles. This effect is characterized by the *momentum compaction factor* [9],

$$\alpha_c = \frac{\Delta C/C}{\delta}, \quad (2.57)$$

relating the circumference of the ring C to the momentum offset δ . A positive momentum compaction factor indicates a longer path traveled by particles with a positive momentum offset, and vice versa.

The momentum compaction factor can also be broken down into orders as an infinite sum, where the constant term is often referred to as the first order,

$$\alpha_c = \underbrace{\alpha_{c,0}}_{\text{Constant term}} + \underbrace{\sum_{i \geq 1} \alpha_{c,i} \delta^i}_{\text{Linear and non linear terms}}. \quad (2.58)$$

In the LHC, the contribution from the non constant terms is negligible [9]. Further details can be found in Section 5.2.1.

2.6. Detuning Effects

2.6.1. Chromaticity

Chromaticity is the tune change ΔQ relative to the momentum offset δ . Chromaticity can be described by a Taylor expansion, given by

$$Q(\delta) = Q_0 + Q' \delta + \frac{1}{2!} Q'' \delta^2 + \frac{1}{3!} Q''' \delta^3 + O(\delta^4). \quad (2.59)$$

Or, more generally, rewritten as a sum to include all orders up to n :

$$Q(\delta) = Q_0 + \sum_{i=1}^n \frac{1}{i!} Q^{(i)} \delta^i. \quad (2.60)$$

2. Concepts of Accelerator Physics

The first order of the chromaticity expansion, Q' , is generally simply referred to as *chromaticity*, sometimes as *linear chromaticity*. The other terms are thus referred to as *non-linear chromaticity*. It is to be noted when referring to a chromaticity order, that the preceding fraction and δ are usually *not* included in the term.

The chromaticity change induced by a single element of order n and length L can be derived from the Hamiltonian of Eq. (2.6), averaging over the phase variables and differentiating relative to the actions $J_{x,y}$ and the momentum offset δ :

$$\Delta Q_{x,y}^{(n)} = \frac{\partial^n Q_{x,y}}{\partial^n \delta} = \frac{1}{2\pi} \int_L \left\langle \frac{\partial^{(n+1)} H}{\partial J_{x,y} \partial^n \delta} \right\rangle ds. \quad (2.61)$$

Detailed derivations can be found in [20].

Natural Chromaticity from Quadrupoles In a purely linear lattice, the linear chromaticity, Q' , is a result of the momentum dependence of the quadrupoles' focusing. It is in this case called the *natural chromaticity* and can be derived from the normal hamiltonian of Eq. (2.7) and expressing the normalized magnet strength K with a dependence on δ via P as $P_0(1 + \delta)$:

$$K_n = \frac{q}{P_0} \frac{1}{1 + \delta} (n - 1)! B_n \quad (2.62)$$

The normal field of a quadrupole is then given by

$$\mathcal{N}_2(x, y) = \frac{1}{2} \frac{q}{P_0} \frac{1}{1 + \delta} B_2 (x^2 - y^2) \quad (2.63)$$

By operating a variable change to the angle coordinates ($x \rightarrow \sqrt{2J_x\beta_x} \cos \phi_x$ and $y \rightarrow \sqrt{2J_y\beta_y} \cos \phi_y$), the following equation linking the β -function and δ to the normal field is obtained:

$$\mathcal{N}_2(x, y) = \frac{1}{2} \frac{q}{P_0} \frac{1}{1 + \delta} B_2 \left[\left(\sqrt{2J_x\beta_x} \cos \phi_x \right)^2 - \left(\sqrt{2J_y\beta_y} \cos \phi_y \right)^2 \right]. \quad (2.64)$$

Following Eq. (2.61), the natural chromaticity Q' induced by quadrupoles is given by:

$$\begin{aligned} \Delta Q'_x &= \frac{1}{2\pi} \int_L \frac{\partial^2 \langle \mathcal{N}_2 \rangle}{\partial J_x \partial \delta} ds \quad ; \quad \Delta Q'_y &= \frac{1}{2\pi} \int_L \frac{\partial^2 \langle \mathcal{N}_2 \rangle}{\partial J_y \partial \delta} ds \\ &= -\frac{1}{4\pi} \frac{q}{P_0} B_2 L \beta_x && = \frac{1}{4\pi} \frac{q}{P_0} B_2 L \beta_y \end{aligned} \quad (2.65)$$

Linear Chromaticity from Sextupoles The first order chromaticity Q' is contributed to by sextupoles in the presence of off-momentum particles. The normal field of a sextupole, following Eq. (2.7) is given by

$$\mathcal{N}_3(x, y) = \frac{1}{3!}(x^3 - 3xy^2). \quad (2.66)$$

As the momentum offset δ introduces a change in orbit via dispersion [21], a variable change can be operated on both x and y , as shown in Eq. (2.67). In this thesis, vertical dispersion will be though neglected.

$$\begin{aligned} x &\rightarrow x + \Delta x = x + D_x \delta \\ y &\rightarrow y + \Delta y = y + D_y \delta \end{aligned} \quad (2.67)$$

The positions x and y can once be replaced, using the twiss parameters, giving the full expression:

$$\begin{aligned} \mathcal{N}_3(x + \Delta x, y) &= \frac{1}{6}K_3 \left[\left(\sqrt{2J_x\beta_x} \cos \phi_x \right)^3 \right. \\ &\quad + 3 \left(\sqrt{2J_x\beta_x} \cos \phi_x \right)^2 D_x \delta \\ &\quad + 3 \left(\sqrt{2J_x\beta_x} \cos \phi_x \right) D_x^2 \delta^2 \\ &\quad \left. + D_x^3 \delta^3 \right. \\ &\quad - 3 \left(\sqrt{2J_x\beta_x} \cos \phi_x \right) \left(\sqrt{2J_y\beta_y} \cos \phi_y \right)^2 \\ &\quad \left. - 3D_x \delta (\sqrt{2J_y\beta_y} \cos \phi_y)^2 \right] \end{aligned} \quad (2.68)$$

Averaging over the phase variables removes any odd cosine:

$$\begin{aligned} \langle \mathcal{N}_3(x + \Delta x, y) \rangle &= \frac{1}{6}K_3 \left(3J_x\beta_x D_x \delta \right. \\ &\quad \left. + D_x^3 \delta^3 \right. \\ &\quad \left. - 3D_x \delta J_y \beta_y \right) \end{aligned} \quad (2.69)$$

The chromaticity can then be obtained by differentiating relative to the action $J_{x,y}$ to retrieve the

tune, and finally by the momentum offset δ .

$$\begin{aligned}\Delta Q'_x &= \frac{1}{2\pi} \int_L \frac{\partial^2 \langle N_3 \rangle}{\partial J_x \partial \delta} ds & ; \quad \Delta Q'_y &= \frac{1}{2\pi} \int_L \frac{\partial^2 \langle N_3 \rangle}{\partial J_y \partial \delta} ds \\ &= \frac{1}{2\pi} L \frac{1}{2} K_3 \beta_x D_x & &= -\frac{1}{2\pi} L \frac{1}{2} K_3 \beta_y D_x \\ &= \frac{1}{4\pi} K_3 L \beta_x D_x & &= -\frac{1}{4\pi} K_3 L \beta_y D_x\end{aligned}\tag{2.70}$$

From this last equation, it is apparent that sextupoles are not a source of chromaticity of higher orders in the presence of linear dispersion. In the presence of second order dispersion [21], sextupoles can generate some amount of Q'' , usually negligible.

Non-Linear Chromaticity Higher orders of the chromaticity function are described in [20] and follow the same logic as for the linear chromaticity from sextupoles. A general formula can be found for the chromaticity of order n , $n > 2$:

$$\begin{aligned}\Delta Q_x^{(n)} &= \frac{1}{4\pi} K_{n+2} L \beta_x D_x^n \\ \Delta Q_y^{(n)} &= -\frac{1}{4\pi} K_{n+2} L \beta_y D_x^n\end{aligned}\tag{2.71}$$

2.6.2. Amplitude Detuning

Amplitude detuning is a tune shift induced by the amplitude of oscillations of a particle. This detuning is directly related to the emittance and can be described via a Taylor expansion around the emittance of both planes, ϵ_x and ϵ_y . Equation (2.72) shows this expansion up to the second order. Further expansions can be found in [20].

$$\begin{aligned}Q_z(\epsilon_x, \epsilon_y) &= Q_{z0} + \left(\frac{\partial Q_z}{\partial \epsilon_x} \epsilon_x + \frac{\partial Q_z}{\partial \epsilon_y} \epsilon_y \right) \\ &\quad + \frac{1}{2!} \left(\frac{\partial^2 Q_z}{\partial \epsilon_x^2} \epsilon_x^2 + 2 \frac{\partial^2 Q_z}{\partial \epsilon_x \partial \epsilon_y} \epsilon_x \epsilon_y + \frac{\partial^2 Q_z}{\partial \epsilon_y^2} \epsilon_y^2 \right) + \dots\end{aligned}\tag{2.72}$$

The first order terms of amplitude detuning are generated by octupoles, and to some extent by sextupoles when considering their higher order contributions. Those higher contributions are usually measurable but small compared to the ones of normal octupoles. It is to be noted that each order does not correspond directly to a multipole order, like for chromaticity seen previously. While it is the case for the simple partial derivatives, the crossterms are instead generated by multipoles of higher orders. Further derivations can be found in ??.

2.6.3. Chromatic Amplitude Detuning

Similar to amplitude detuning, *chromatic amplitude detuning* is a tune shift induced by the amplitude of oscillations of a particle but with an additional dependence on the momentum offset. This effect can be described by a Taylor expansion around the emittance of both planes ϵ_x , ϵ_y , and the momentum offset δ . Eq. (2.73) shows this expansion up to the second order. Both the emittance ϵ and the action J can be seen to describe the chromatic amplitude detuning. Terms are interchangeable with $\epsilon_{x,y} = 2J_{x,y}$.

$$\begin{aligned} Q_z(\epsilon_x, \epsilon_y, \delta) = Q_{z0} + & \left[\frac{\partial Q_z}{\partial \epsilon_x} \epsilon_x + \frac{\partial Q_z}{\partial \epsilon_y} \epsilon_y + \frac{\partial Q_z}{\partial \delta} \delta \right] \\ & + \frac{1}{2!} \left[\frac{\partial^2 Q_z}{\partial \epsilon_x^2} \epsilon_x^2 + \frac{\partial^2 Q_z}{\partial \epsilon_y^2} \epsilon_y^2 + \frac{\partial^2 Q_z}{\partial \delta^2} \delta^2 \right. \\ & \quad \left. + 2 \frac{\partial^2 Q_z}{\partial \epsilon_x \partial \epsilon_y} \epsilon_x \epsilon_y + 2 \frac{\partial^2 Q_z}{\partial \epsilon_x \partial \delta} \epsilon_x \delta + 2 \frac{\partial^2 Q_z}{\partial \delta \partial \epsilon_y} \delta \epsilon_y \right] \\ & + \dots \end{aligned} \quad (2.73)$$

Sextupolar contributions To the first order, the terms of the chromatic amplitude detuning are shared with the classic amplitude detuning, which are not contributed to by sextupoles. The last term however is the linear chromaticity, seen previously in 2.6.1.

Octupolar contributions Similar to the sextupolar contributions, to the first order, the terms are shared with amplitude detuning. The first terms $\frac{\partial Q_z}{\partial \epsilon_x} \epsilon_x$ and $\frac{\partial Q_z}{\partial \epsilon_y} \epsilon_y$ are then contributed to by octupoles. The second order chromaticity Q'' appears when expanding to the second order.

Decapolar contributions So far, only terms with amplitude detuning and chromaticity have been seen. The terms highlighted in orange, in Eq. (2.74), are the terms contributed to by decapoles. Terms depending on both the emittance and the momentum offset are present, as well as the third order chromaticity Q''' .

$$\begin{aligned} Q_z(\epsilon_x, \epsilon_y, \delta) = Q_{z0} + & \left[\frac{\partial Q_z}{\partial \epsilon_x} \epsilon_x + \frac{\partial Q_z}{\partial \epsilon_y} \epsilon_y + \frac{\partial Q_z}{\partial \delta} \delta \right] \\ & + \frac{1}{2!} \left[\frac{\partial^2 Q_z}{\partial \epsilon_x^2} \epsilon_x^2 + \frac{\partial^2 Q_z}{\partial \epsilon_y^2} \epsilon_y^2 + \frac{\partial^2 Q_z}{\partial \delta^2} \delta^2 \right. \\ & \quad \left. + 2 \frac{\partial^2 Q_z}{\partial \epsilon_x \partial \epsilon_y} \epsilon_x \epsilon_y + 2 \frac{\partial^2 Q_z}{\partial \epsilon_x \partial \delta} \epsilon_x \delta + 2 \frac{\partial^2 Q_z}{\partial \delta \partial \epsilon_y} \delta \epsilon_y \right] \\ & + \frac{1}{3!} \left[\frac{\partial^3 Q_z}{\partial \delta^3} \delta^3 + \frac{\partial^3 Q_z}{\partial \epsilon_x^3} \epsilon_x^3 + \frac{\partial^3 Q_z}{\partial \epsilon_y^3} \epsilon_y^3 + \dots \right] \end{aligned} \quad (2.74)$$

Further derivations can be found in ??.

2.6.4. Feed-Down

When a particle passes off-center through a magnet, an effect called *feed-down* appears. Feed-down is a lower order contribution created by either mis-aligned magnets or an off-center orbit of the beam. A particle with an orbit offset will then experience the main field of the magnet and effects similar to those of lower order multipoles.

2.7. Resonances

2.7.1. Tune Diagram

The resonances discussed in this thesis are related to the optics of the accelerator. Such resonances create unstable motion and can lead to loosing particles. Those perturbations arise from particles oscillating at frequencies excited by certain multipoles.

Fig. 2.9 shows a tune diagram where the fractional part of tunes Q_x and Q_y can be related to resonance lines excited by multipoles up to decapoles ($n = 5$). It becomes apparent that the diagram fills quickly when considering further orders. Thankfully, the higher the multipole order, the weaker the resonances are. This makes choosing a working point possible, even if some particles are hitting resonance lines.

When considering the resonance driving terms f_{jklm} from Eq. (2.37), it can be noted that the term diverges for particular tune values. This leads to a disproportionate increase in particles position in phase-space, eventually leading to loosing them. Resonant conditions due to the tunes can thus be described by the following condition:

$$(j - k)Q_x + (l - m)Q_y = p \quad , \quad j, k, l, m, p \in \mathbb{Z}. \quad (2.75)$$

2.7.2. Frequency Spectrum

As seen in Eq. (2.41), resonance driving terms have an impact on the transverse position of a particle. This means that performing a FFT on such a signal will reveal spectral lines in the frequency spectrum. Each RDT f_{jklm} can thus be observed in either one or both the frequency spectrums of the horizontal and vertical planes, at multiples of $Q_x \pm Q_y$. Eq. (2.76) shows where those lines would appear:

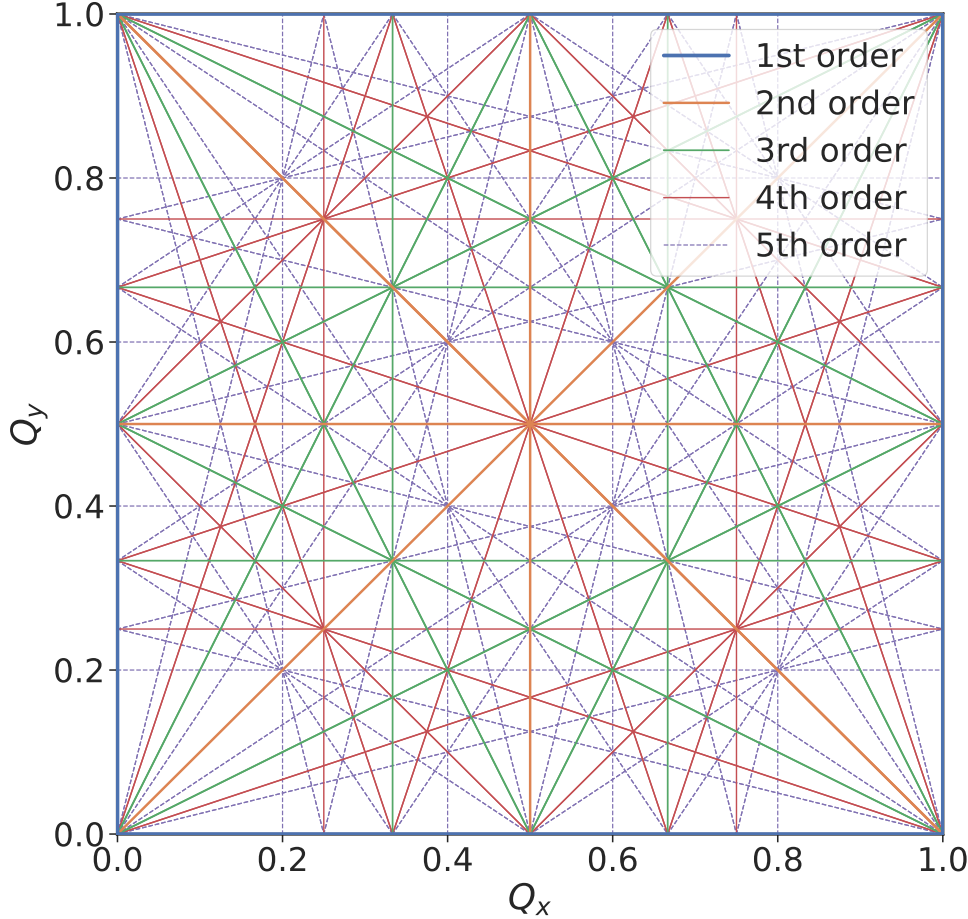


Figure 2.9.: Tune diagram with resonances lines excited by multipoles up to decapole ($n \leq 5$). The working point of the machine is chosen in an area where few lines are present.

$$\begin{aligned} H_{jklm} & \text{ at } (1-j+k)Q_x + (m-l)Q_y & ; & \quad j \neq 0 \\ V_{jklm} & \text{ at } (k-j)Q_x + (1-l+m)Q_y & ; & \quad l \neq 0. \end{aligned} \quad (2.76)$$

The RDT f_{3000} coming from sextupoles can for example be seen in the horizontal spectrum at $(1-3+0)Q_x + (0-0)Q_y = -2Q_x$. For a value $Q_x = 0.27$, the line is seen at 0.46. in a spectrum bound in $[0, 0.5]$. No line can be seen in the vertical spectrum due to $l = 0$. Detailed tables of such lines for RDTs up to order 6 can be found in Appendix C.

The amplitude of each line will depend on the action I_z and the amplitude of the RDT [22]:

$$\begin{aligned}|H_{f_{jklm}}| &= 2j(2I_x)^{\frac{j+k-1}{2}}(2I_y)^{\frac{l+m}{2}}|f_{jklm}| \\ |V_{f_{jklm}}| &= 2l(2I_x)^{\frac{j+k}{2}}(2I_y)^{\frac{l+m-1}{2}}|f_{jklm}|.\end{aligned}\tag{2.77}$$

2.7.3. Resonance Driving Terms

By reworking the previous Eq. (2.77), it can be seen that RDTs are factors of the line amplitude and the actions I_x and I_z :

$$\begin{aligned}|f_{jklm}| &= \frac{|H_{f_{jklm}}|}{2j(2I_x)^{\frac{j+k-1}{2}}(2I_y)^{\frac{l+m}{2}}} \\ |f_{jklm}| &= \frac{|V_{f_{jklm}}|}{2l(2I_x)^{\frac{j+k}{2}}(2I_y)^{\frac{l+m-1}{2}}}.\end{aligned}\tag{2.78}$$

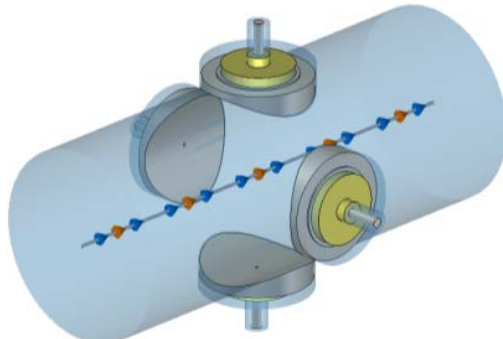
In practice, an approximation of $J = I$ is done. The RDT is then related to the fit of the line amplitude versus the action.

Optics Measurements and Corrections

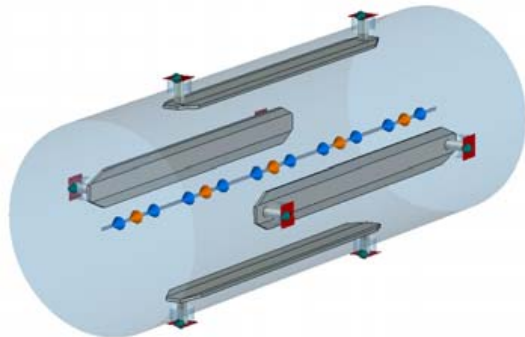
3.1. Beam Instrumentation

3.1.1. Beam Position Monitors

Beam Position Monitors (BPMs) are one of the most utilized and essential elements of beam diagnostics in particle accelerators. In the LHC, most of the BPMs are dual plane, and thus composed of four electrodes, distributed as two per plane. The BPM system consists of over than 550 BPMs per beam, distributed along the ring, in the arcs and the IPs. The most common type, the *curved-button*, shown in Fig. 3.1a, is typically placed near quadrupoles [23].



(a) Curved-button "BPM" type BPM of the LHC [23].



(b) Stripline "BPMSW" type BPM of the LHC [23].

Other pickups such as the *stripline*, shown in Fig. 3.1b, albeit more complex and expensive, offer a

3. Optics Measurements and Corrections

better signal to noise ratio and are capable of identifying the direction of the beam [23]. Such features are essential for the LHC, were both beams travel through the same aperture at the IPs.

The BPM response is not linear with the beam position, which requires a post-processing not systematically implemented in accelerators beam diagnostics systems. LHC's BPMs have been simulated and polynomials fitted to minimize this response error [24].

3

3.1.2. Collimators

3.1.3. Beam Loss Monitors

Beam Loss Monitors are detectors mounted on various elements of the accelerator, such as magnets or collimators, to detect abnormal losses of particles. They play a crucial role in the protection of the machine, triggering a dump when losses exceed the threshold set for their respective element. BLMs use ionization chambers, working on the same principle as simple Geiger counters: a tube filled with gas, in presence of a high voltage.

Dashboards in the control room are regularly used to monitor the losses along the ring when performing optics measurements, as those prove to often be destructive.

3.1.4. AC-Dipole

The AC dipole of the LHC is a crucial component for optics studies. Its primary function is to excite the beam into large coherent oscillation, achieved by applying a sinusoidally oscillating dipole field [25]. By ramping up and down adiabatically the field, large coherent oscillations can be produced without any decoherence or emittance growth. Figure 3.2 shows an example of a measurement made with an AC-Dipole. Exciting the beam to large amplitudes make the study of linear optics, such as beta-beating easier, and that of non linear optics such as resonances possible.

The AC-Dipole is set to oscillate at a frequency Q_d , different from the natural tune of the machine Q and thus introduces systematic effects that needs to be compensated during the optics analysis. The new orbit of a particle under the influence of the AC-Dipole, at turn number n and observation point s , is given by [26]:

$$z(s, n) = \frac{BL}{4\pi\rho\delta_z} \cdot \sqrt{\beta_z(s)\beta_{z,0}} \cdot \cos(2\pi Q_{d,z}n + \phi_z(s) + \phi_{z,0}), \quad (3.1)$$

where B is the amplitude of the oscillating magnetic field, L the length of the AC-Dipole, $B\rho$ the magnetic rigidity, δ the difference between Q_d and Q , β and β_0 the beta function at the observed point and the AC-Dipole, ϕ and ϕ_0 the phase advance at the observed point and of the AC-Dipole.

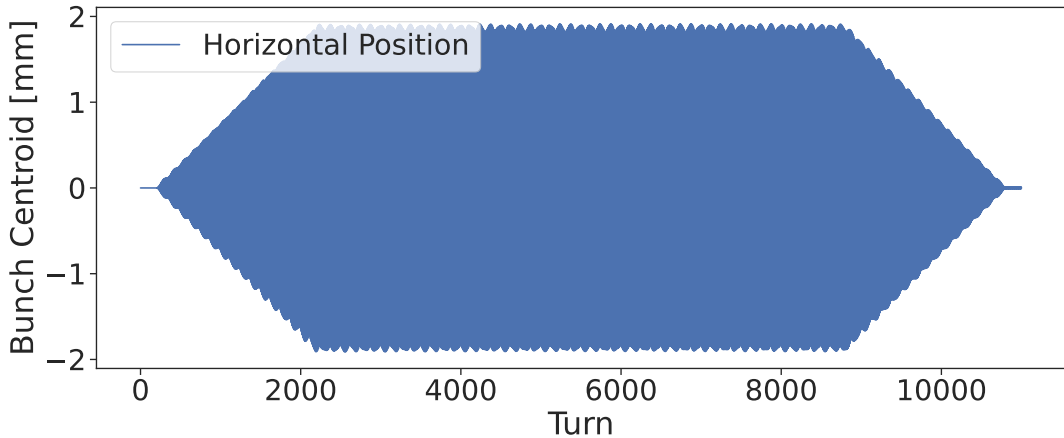


Figure 3.2.: Simulated turn by turn data with an AC-Dipole first ramping up then down.

3.2. Correction Principles

3.2.1. Response Matrix

A response matrix is a linear equation system that describes the change of an observable for a set of individual multipole strengths. By taking the pseudo-inverse of this matrix and multiplying it to the measured observables, a set of corrector strengths is obtained that can replicate the measured value. Taking the opposite sign then gives a correction. This technique is routinely used to correct, amongst others, β -beating as well as Resonance Driving Terms. In situations where measurements are taken at each BPM for a particular observable, the corresponding response matrix ends up containing over 500 values per corrector, for a single beam.

Individual MAD-X simulations are run with a single multipole powered at a time. The resulting parameter values (e.g. β -beating) are then compared to those obtained from a simulation without any powering, allowing to determine the specific impact of each multipole.

A response matrix is thus created following Eq. (3.2), for a matrix of observables O , a reference matrix of observables without any corrector O_R and a fixed multipole strength k . Given measured data M , the set of correctors needed to compensate the values can be obtained by taking the pseudo-inverse of the matrix in Eq. (3.3).

$$R = (O - O_R) \cdot \frac{1}{k} \quad (3.2)$$

3. Optics Measurements and Corrections

$$\begin{bmatrix} k_1 \\ \vdots \\ k_n \end{bmatrix} = -(R^+ \cdot M) \quad (3.3)$$

Response matrices are very versatile and can combine several observables to be corrected by the same multipoles. One example, detailed later in this thesis, is the third order chromaticity and the resonance driving term f_{1004} , both contributed to by decapoles.

Example

In this example, simulations are run with MAD-X PTC to correct the third chromaticity in the LHC. Q''' is taken from `ptc_normal1` for each beam and axis, with MCDS, decapole correctors, powered with a fixed strength one at a time. A scaling factor is applied to get the change of chromaticity for one unit of K_5 . 8 correctors are used, which strengths are denoted k_1 through k_8 . Transposes are only used to make the equations easier to display.

The values in Tab.3.1 are corrected via Eq. (3.5) after having built the response matrix in Eq. (3.4).

Observable	Value
Q_x'''	-666111
Q_y'''	121557

Table 3.1.: Example chromaticity values to correct via a response matrix

$$R = \left(\text{Individual simulations} \left\{ \underbrace{\begin{bmatrix} Q_x''' & Q_y''' \end{bmatrix}}_T - \underbrace{\begin{bmatrix} 5135 \\ 8470 \end{bmatrix}}_{\text{Reference}} \right\} \underbrace{\begin{bmatrix} 1 \\ -1000 \end{bmatrix}}_{\text{Corrector strength}} \right). \quad (3.4)$$

$$\begin{bmatrix} -155899 & 122004 \\ -254584 & 138368 \\ -122715 & 106709 \\ -218597 & 110686 \\ -134140 & 106463 \\ -245791 & 118951 \\ -147035 & 116544 \\ -219537 & 112317 \end{bmatrix}$$

$$\begin{aligned} k_1 & \begin{pmatrix} -1235 \\ 1032 \end{pmatrix} \\ k_2 & \begin{pmatrix} -1394 \\ 1449 \end{pmatrix} \\ k_3 & \begin{pmatrix} -1043 \\ 1864 \end{pmatrix} \\ k_4 & \begin{pmatrix} -1187 \\ 1369 \end{pmatrix} \\ k_5 & = -R^+ \cdot \begin{pmatrix} -666111 \\ 121557 \end{pmatrix} \end{aligned} \quad \text{Measured values} \quad (3.5)$$

3.2.2. Chromaticity

As per the placement of the MCO and MCD spool piece correctors in the LHC layout [27], β -functions at their location are slightly different from arc to arc. This slight imbalance leads theoretically to the possibility of correcting the horizontal and vertical axes of the second and third order chromaticity independently, via a response matrix approach. In practice, the required strength to do so would exceed those of the design of the correctors.

Another way to correct the chromaticity is via a global uniform trim, where every available corrector is powered to the same strength. Simulations are run with `ptc_normal` via MADX-PTC to obtain the response in chromaticity for a given strength. Chromaticity being linear with multipole strength, an affine function can be determined for each axis. Figure 3.3 shows a simulation with several MCD strengths, highlighting this linear relation between $Q'''_{x,y}$ and K_5 , while Equation (3.6) shows an example of such functions computed at injection energy for the 2022 optics.

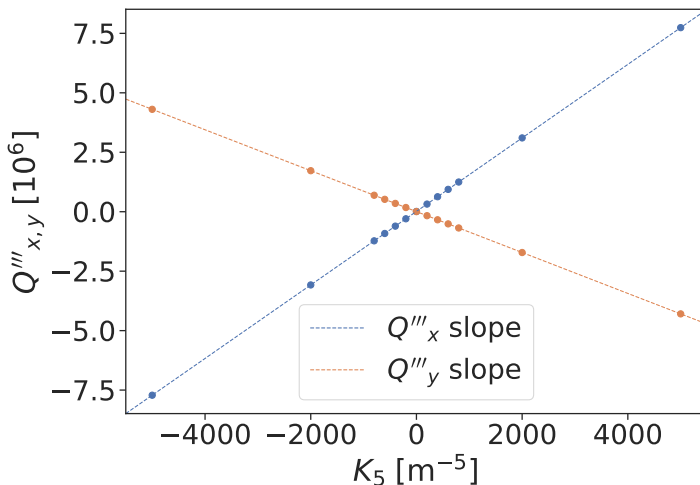


Figure 3.3.: Linear relation between the third order chromaticity and decapole corrector strengths, simulated with MADX-PTC.

$$\begin{aligned} Q_x''' &= 1533 \cdot \Delta K_5 + 6680 \\ Q_y''' &= -860 \cdot \Delta K_5 + 5647 \end{aligned} \quad (3.6)$$

Only the linear part is relevant, as the offset is generated by other multipoles and field errors. It is thus constant for a configuration where only the relevant spool pieces are used.

Corrections involve minimizing both axes, typically where Q_x''' meets Q_y''' :

$$\Delta K_5 = -\frac{(Q_x''' - Q_y''')}{\text{slope}_{Q_x'''} - \text{slope}_{Q_y'''}} \quad (3.7)$$

3.3. Optics Measurements

3.3.1. Turn-by-Turn Data

Data is typically acquired turn by turn while exciting the beam with an AC-Dipole. This is usually done with a *pilot bunch*, with a reduced intensity of 10^9 protons compared to an operation bunch of 10^{11} . This allows for higher amplitude oscillations while remaining safe for the machine.

A spectral analysis is then performed via a *FFT*, making apparent the driven tunes from the AC-Dipole, the transverse tunes and the possible resonance lines, as shown in Fig. 3.4.

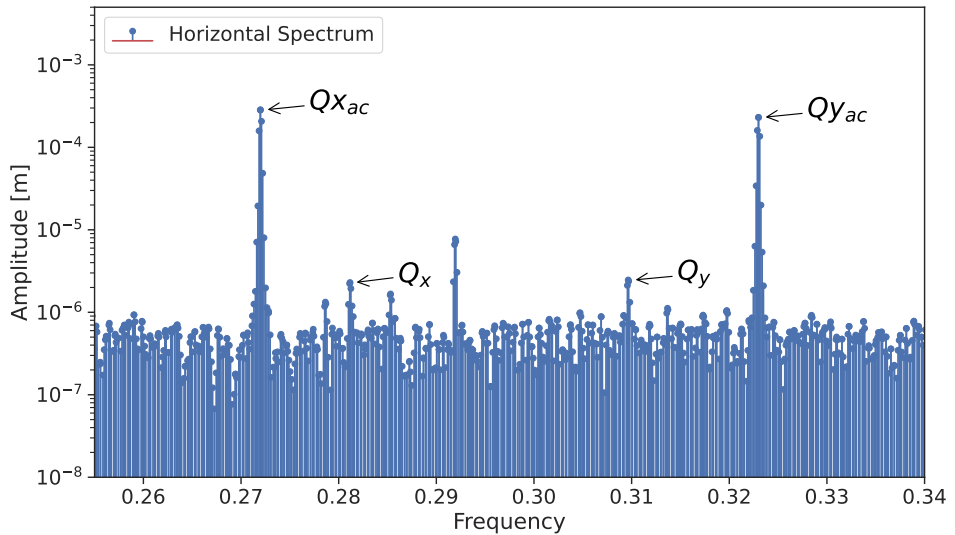


Figure 3.4.: Horizontal frequency spectrum of a turn-by-turn measurement in the LHC. The *driven* tunes of the AC-Dipoles have the highest amplitudes while the natural tune can be seen close to it. Other lines are often created by resonances.

From this, the *optics* such as β -beating, dispersion, coupling and Resonance Driving Terms can be reconstructed [28].

3.3.2. Chromaticity

Procedure

Chromaticity measurements are typically performed by varying the RF frequency to induce a change of momentum offset δ , while measuring the tune. The momentum offset δ being related to the RF frequency, the Lorentz factor γ and the momentum compaction factor α_c [9]:

$$\delta = - \left(\frac{1}{\gamma^{-2} + \alpha_c} \right) \cdot \frac{\Delta f_{\text{RF}}}{f_{\text{RF,nominal}}} \quad (3.8)$$

In the LHC, the Lorentz factor γ is here negligible, as the energy is large even at injection. At 450GeV, $\gamma^{-2} \approx 10^{-6}$, which is two orders of magnitude smaller than α_c .

Frequency steps of 20Hz every 30 secondes are usually taken to compromise between number of data points, precision of the tune estimate, and duration of the measurement. Once beam losses, registered by the BLMs are deemed too high, the frequency is reverted back to its nominal value in larger steps. The same procedure is then re-applied in the negative. Figure 3.5 shows a typical RF scan performed to measure chromaticity in the LHC.

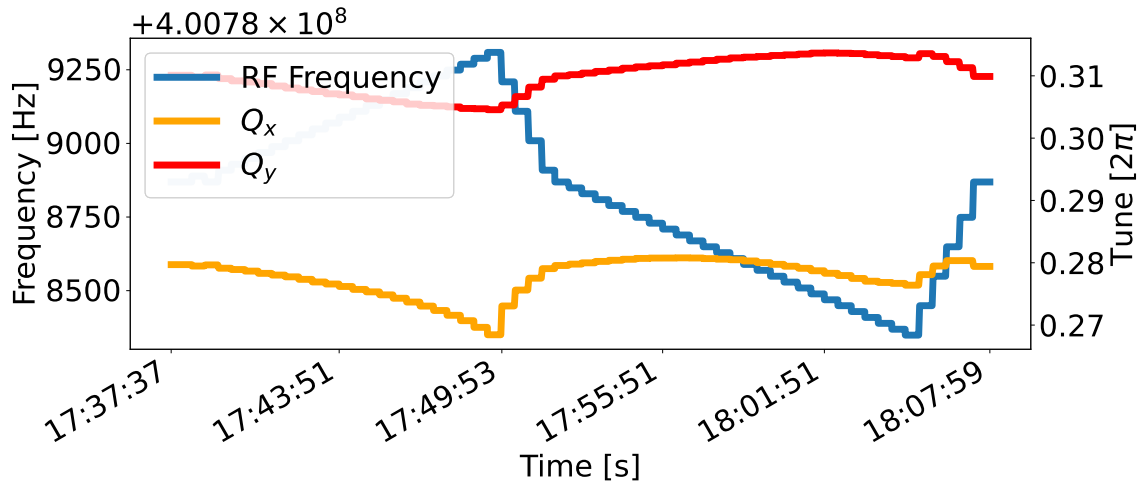


Figure 3.5.: Observation of the tune dependence on momentum offset, created by a shift of RF frequency.

Analysis

Once the tunes have been acquired and the momentum offset computed via Eq. (3.8), the chromaticity function (see Eq. (2.59)) can be used to fit the measured data and retrieve each order.

As part of work for this thesis, a custom tool was developed, in order to ease such analysis of chromaticity measurements. This tool, the Non-Linear Chromaticity GUI [29], is composed of several parts:

- Data extraction from CERN data servers (Timber, NXCAL)
- Tune cleaning and standard deviation calculation
- Chromaticity fit up to 7th order
- Corrections of chromaticity and resonance driving terms

Decapolar Fields

4.1. Introduction

4.1.1. Motivation

Beam-based measurements have been carried in the LHC since Run 1 to better understand the decapolar fields. Those have been carried out via chromaticity measurements [30–32]. The third order of the non-linear chromaticity, Q''' , generated for the most part by decapoles, has shown a consistent discrepancy at injection energy between its expected value from simulations and that observed. Figure 4.1 highlights this discrepancy.

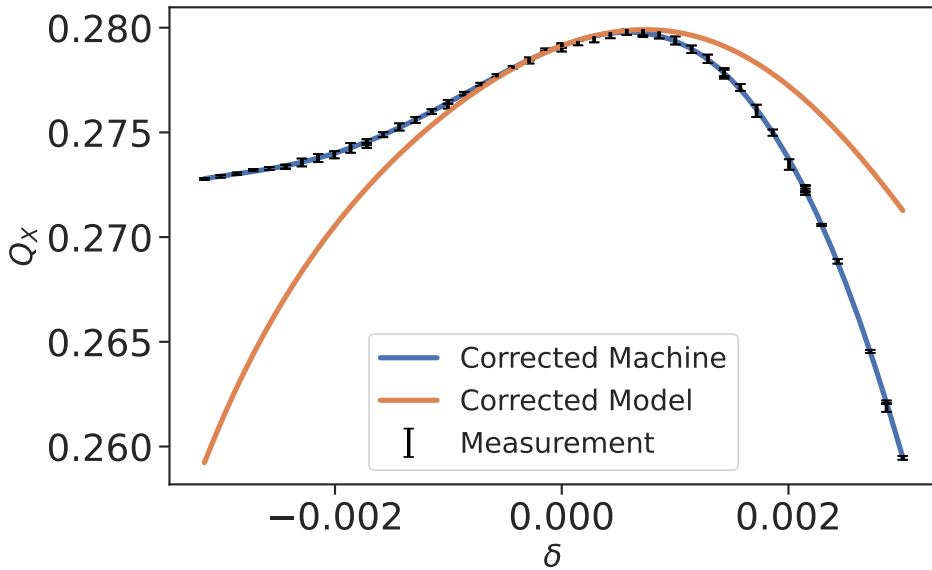


Figure 4.1.: Measured and simulated chromaticity with application of the nominal decapolar corrections from FiDeL. It can be seen that although the corrections should diminish Q''' , it is not well corrected in practice.

The FiDeL magnetic model is used during operation to correct various multipole errors, including octupolar and decapolar. The operational corrections being based on this magnetic model and simulations, the residual Q''' value is expected to be small, which is however not the case. Chromaticity measurements have thus been repeated during LHC's Run 3 and corrections made routine, aimed at correcting the observed discrepancy.

The study of non-linear chromaticity has proven valuable in quantifying decapolar fields, yet it does not permit alone to understand the exact origins of the observed discrepancy. In an effort to gain deeper insights, additional measurements were performed focusing on novel observables that had not been previously explored. *Bare chromaticity* involves measuring chromaticity with the octupolar and decapolar correctors deactivated ; this approach aims to isolate the machine effects from those of the correctors. *Chromatic amplitude detuning*, evaluates how the tune varies with both the beam's action and the momentum offset ; this methods has the benefit of having a different expression than of the chromaticity.

Complementing those measurements, studies of decapolar Resonance Driving Terms have been undertaken for the first time in the LHC. Contributing to resonances close to the working, those RDTs also have benefited from corrections.

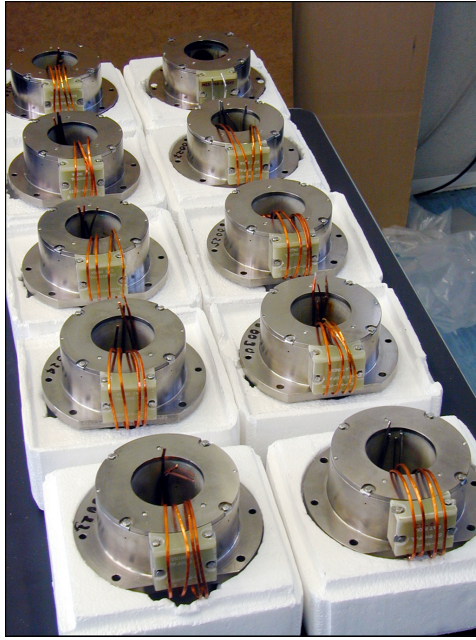


Figure 4.2.: Decapoles on a test bench, being inspected after manufacturing [34].

4.1.2. Decapolar Correctors

As seen in Fig. 1.3, the LHC is equipped with decapoles. Those magnets are part of the design report, aiming at correcting the field errors of the main dipoles. Those correctors, denominated *MCD*, are specific to each beam and are placed after every second dipole, totaling 1232 in number [33]. MCDs are nested with octupolar correctors, *MCO*. The pair of those correctors of often referred to as *MCDO*. It is not possible to individually power each corrector. Rather, a circuit consists of a whole arc. There are in total 16 circuits to control the correctors of both beams and 8 arcs. Fig. 4.2 shows a picture taken of decapoles on a test bench.

The important characteristics of the magnetic fields of correctors are their main field transfer function (or *response*), the field quality and possible crosstalk, as MCOs and MCDs are nested [33]. In order to better understand the decapolar fields, the decapole correctors themselves need to be studied.

Strengths at Injection At injection energy, the decapoles are powered to a static strength. New optics introduced throughout the years often have for effect to vary slightly the β -function along the ring, having thus an impact on the chromaticity, as seen in Eq. (2.71). New corrections are then computed via FiDeL to account for it. Although those corrections vary throughout the years, the shift is in practice fairly negligible. Table 4.10, a bit further in this chapter, shows the strength of the correctors and the related circuits at injection energy for the optics deployed in 2024.

Circuit	$K_5 [m^{-5}]$
Beam 1	
RCD.A12B1	-4582
RCD.A23B1	-5106
RCD.A34B1	-4855
RCD.A45B1	-4577
RCD.A56B1	-4125
RCD.A67B1	-5166
RCD.A78B1	-6827
RCD.A81B1	-5500
Beam 2	
RCD.A12B2	-4490
RCD.A23B2	-5155
RCD.A34B2	-4825
RCD.A45B2	-4619
RCD.A56B2	-4064
RCD.A67B2	-5066
RCD.A78B2	-6866
RCD.A81B2	-5446

Table 4.1.: Strength of decapolar correctors at injection energy for FiDeL corrections.

4.2. Response of correctors

Expression The full third term of the chromaticity function is highlighted in Eq. (4.1). Details on chromaticity are given in Section 2.6.1.

$$Q(\delta) = Q_0 + Q'\delta + \frac{1}{2!}Q''\delta^2 + \boxed{\frac{1}{3!}Q''' \delta^3} + O(\delta^4). \quad (4.1)$$

This third order, mainly contributed to by decapoles, is related to the β -function, the dispersion and the strength of the multipole:

$$\begin{aligned} \Delta Q_x''' &= \frac{1}{4\pi} K_5 L \beta_x D_x^3 \\ \Delta Q_y''' &= - \frac{1}{4\pi} K_5 L \beta_x D_x^3. \end{aligned} \quad (4.2)$$

Measurements and Corrections In order to assess the accuracy of corrections, measurements have to be done to gauge the response of the decapolar correctors, *MCDs*. During Run 3's commissioning, measurements and corrections of Q'' and Q''' have been made routine. Those corrections give the opportunity to study the response of the correctors. Fig. 4.3 shows the chromaticity function measured during Run 3's commissioning in 2022 with the nominal corrections via FiDeL and beam-based corrections computed analytically based on top of FiDeL.

4. Decapolar Fields

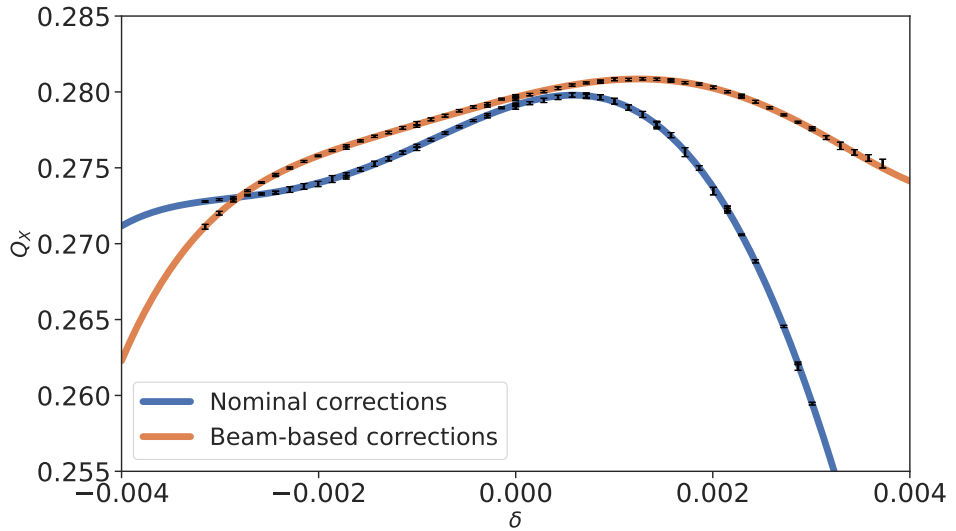


Figure 4.3.: Chromaticity of the horizontal plane of Beam 1 during Run 3's commissioning, with nominal corrections based on the magnetic model and beam-based corrections aimed at correcting Q'' and Q''' .

The nominal and corrected Q''' values are shown in Table 4.2. The shift in Q''' is shown in Table 4.3 for each beam and axis, and is showing a good agreement between the measurements and simulations. The slight imbalance can be attributed to higher order effects of the octupole correctors, whose correction was implemented after that of Q''' .

Plane	$Q'''[10^6]$	
	Nominal	Beam-Based
Beam 1		
X	-3.36 ± 0.04	-1.02 ± 0.03
Y	1.62 ± 0.05	0.12 ± 0.02
Beam 2		
X	-2.72 ± 0.08	-0.64 ± 0.03
Y	1.54 ± 0.06	0.14 ± 0.03

Table 4.2.: Third order chromaticity obtained during Run 3 commissioning, with nominal and beam-based corrections aimed at correcting Q'' and Q''' .

Plane	$\Delta Q'''[10^6]$	
	Measurement	Simulation
Beam 1		
X	2.3 ± 0.1	2.5
Y	-1.5 ± 0.1	-1.4
Beam 2		
X	2.1 ± 0.1	2.5
Y	-1.4 ± 0.1	-1.4

Table 4.3.: Response of the third order chromaticity upon application of corrections on top of the nominal ones used in operation for both measurements and simulations.

This agreement between the simulations and the measurements indicates that our decapole correctors function as intended. No noticeable cross-talk between magnets or hysteresis have been identified.

4.3. Bare Chromaticity

Previous studies [32] have demonstrated that octupole and decapole correctors were contributing to an observed octupolar discrepancy in the machine via hysteresis and feed-down. To evaluate the possible effect of decapole correctors on the third order chromaticity Q''' , a measurement was taken with these elements turned off.

4. Decapolar Fields

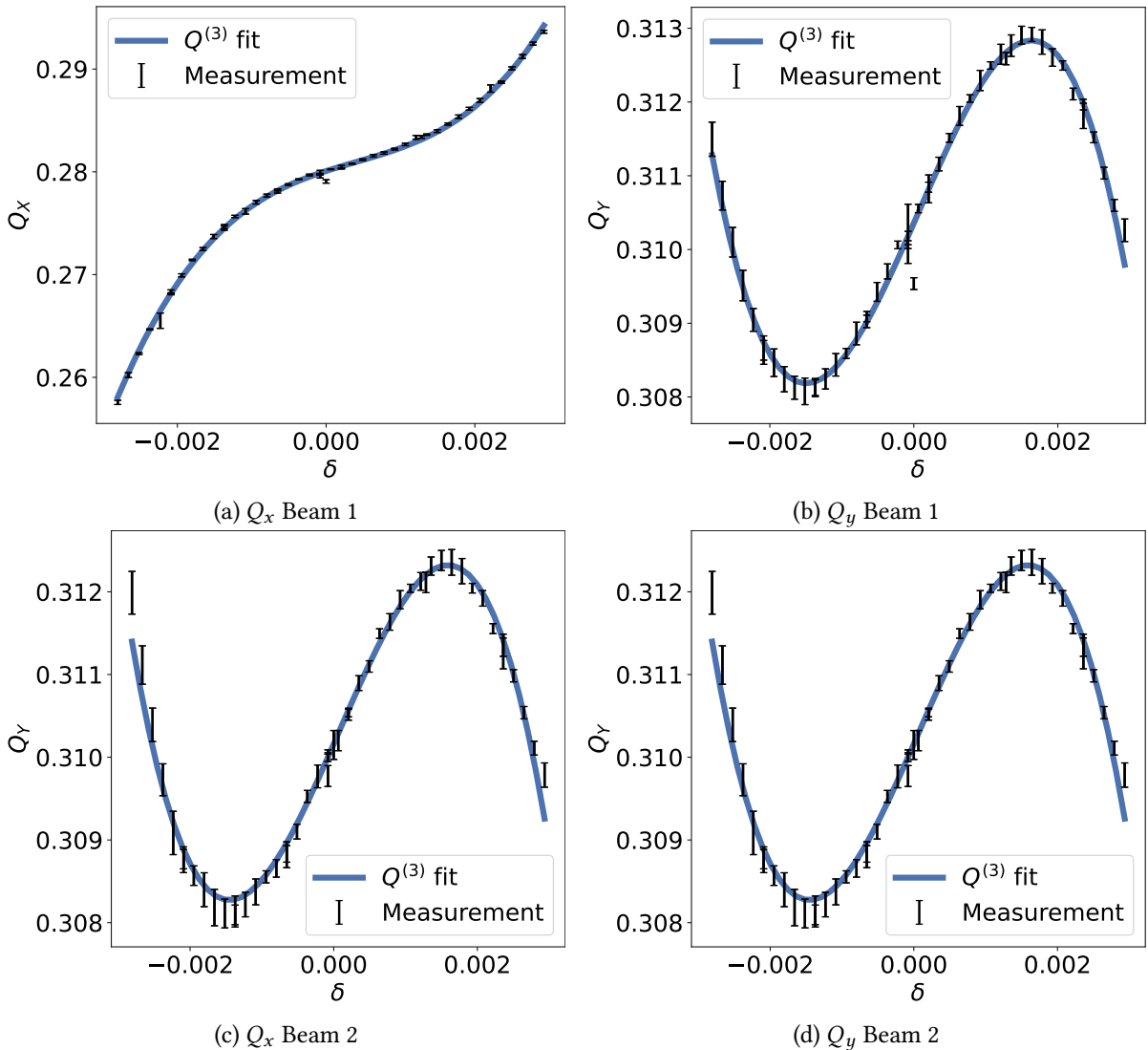


Figure 4.4.: Fit of the chromaticity function for the chromaticity measurement performed with octupole and decapole correctors powered off. The fit includes all orders up to third.

Simulations have been run with MAD-X and PTC including fields errors from b_3 to b_8 . The expected Q''' values are presented in Table 4.4 and compared to the measured ones along with the ratio between the two.

A consistent ratio is observed for every beam and plane between the measurement and the model. This result, supplemented by the correct response of the correctors, indicates that the decapolar correctors do not generate unwanted fields. Those correctors can thus be discarded as the potential source of discrepancy.

Quantity	Measured [10 ⁶]	Simulated [10 ⁶]	Ratio
Beam 1			
Q_x'''	2.95 ± 0.04	6.94 ± 0.02	0.43 ± 0.01
Q_y'''	-1.82 ± 0.04	-4.29 ± 0.01	0.42 ± 0.01
Beam 2			
Q_x'''	3.06 ± 0.07	7.03 ± 0.02	0.44 ± 0.01
Q_y'''	-1.72 ± 0.02	-4.27 ± 0.01	0.42 ± 0.01

Table 4.4.: Measured and simulated third order chromaticity with octupole and decapole correctors turned off. The simulations include field errors from sextupoles to decahexapole (b_3 to b_8).

4.4. Chromatic Amplitude Detuning

The Chromatic Amplitude Detuning is the tune shift dependant on both the actions and the momentum offset, whose decapole contributed terms are described via a Taylor expansion in Eq. (4.3). More information and derivations can be found in Section 2.6.3 and Appendix B.

$$\Delta Q(J_x, J_y, \delta) = \frac{\partial^2 Q}{\partial J_x \partial \delta} \cdot J_x \delta + \frac{\partial^2 Q}{\partial J_y \partial \delta} \cdot J_y \delta + \frac{1}{3!} \frac{\partial^3 Q}{\partial \delta^3} \cdot \delta^3. \quad (4.3)$$

The last term is more commonly referred to as the third order chromaticity, Q''' . Each of those terms depend on the β -functions, the horizontal dispersion D and the normalized decapole field gradient K_5 for a single source of length L ,

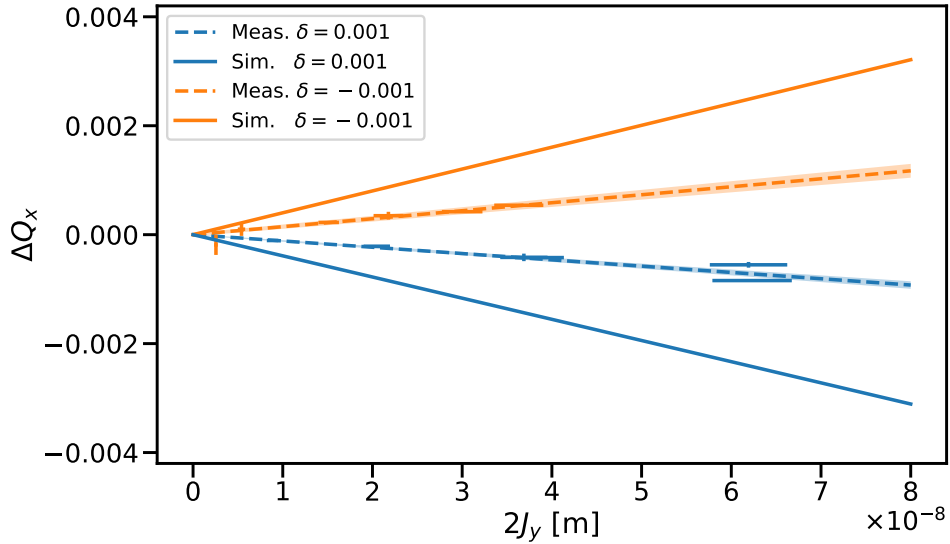
$$\begin{aligned} \frac{\partial^2 Q_x}{\partial J_x \partial \delta} &= \frac{1}{16\pi} K_5 L \beta_x^2 D, & \frac{\partial^2 Q_x}{\partial J_y \partial \delta} &= -\frac{1}{8\pi} K_5 L \beta_x \beta_y D, \\ \frac{\partial^3 Q_x}{\partial \delta^3} &= \frac{1}{4\pi} K_5 L \beta_x D^3, & \frac{\partial^2 Q_y}{\partial J_x \partial \delta} &= -\frac{1}{8\pi} K_5 L \beta_x \beta_y D, \\ \frac{\partial^2 Q_y}{\partial J_y \partial \delta} &= \frac{1}{16\pi} K_5 L \beta_y^2 D, & \frac{\partial^3 Q_y}{\partial \delta^3} &= -\frac{1}{4\pi} K_5 L \beta_y D^3. \end{aligned} \quad (4.4)$$

The action dependant terms can be measured by exciting the beam with an AC-dipole with increasing strengths at different momentum-offsets.

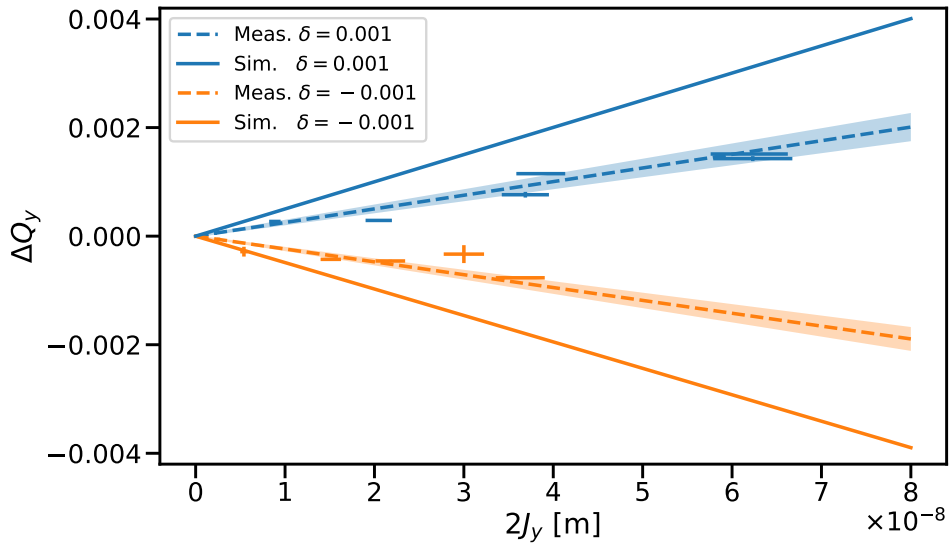
Such a measurement was taken with octupole and decapole correctors turned off to measure the bare machine. Some data could not be collected due to machine availability issues, restricting the measurement to low intensity kicks. Nevertheless, the terms $\frac{\partial^2 Q_x}{\partial J_y \partial \delta}$ and $\frac{\partial^2 Q_y}{\partial J_y \partial \delta}$ for beam 2 were measured for the first time in the LHC. The momentum-offsets measured at were -0.001 and 0.001 , respectively roughly equal to a trim of $+140\text{Hz}$ and -140Hz of the RF.

4. Decapolar Fields

Fig. 4.5a and Fig. 4.5b show a fit of those terms to measured $Q_{x,y}$ vs J_y at two different momentum offsets. Expected shifts from MADX-PTC simulations, that include field errors ranging from sextupoles to decahexapoles (b_3 to b_8 and a_4 to a_8) are shown as a comparison.



(a) Horizontal tune shift depending on the vertical action: $\frac{\partial^2 Q_x}{\partial J_y \partial \delta}$.



(b) Vertical tune shift depending on the vertical action: $\frac{\partial^2 Q_y}{\partial J_y \partial \delta}$.

Figure 4.5.: Measured and simulated tune shift due to a change of action via an AC-Dipole at two different momentum offsets. Each fit corresponds to a chromatic amplitude detuning term evaluated at a certain δ .

Type	$\frac{\partial^2 Q_x}{\partial J_y \partial \delta} [10^4 \text{m}^{-1}]$	$\frac{\partial^2 Q_y}{\partial J_y \partial \delta} [10^4 \text{m}^{-1}]$
$\delta = +0.001$		
Meas.	-1.16 ± 0.08	1.26 ± 0.15
Sim.	-3.82 ± 0.01	2.47 ± 0.01
Ratio	0.30 ± 0.02	0.51 ± 0.06
$\delta = -0.001$		
Meas.	1.47 ± 0.12	-1.18 ± 0.13
Sim.	3.92 ± 0.01	-2.41 ± 0.01
Ratio	0.38 ± 0.03	0.49 ± 0.05

Table 4.5.: Comparison of the measured and simulated terms $\frac{\partial^2 Q_x}{\partial J_y \partial \delta}$ and $\frac{\partial^2 Q_y}{\partial J_y \partial \delta}$ via PTC, at two discrete momentum offsets. Simulations include errors from b_3 to b_8 and a_4 to a_8 .

A consistent difference between simulation and measurement is observed, which values and ratios of measurement to model can be found in Table 4.5. The observed ratios of measurement to model for the chromatic amplitude detuning show slight discrepancies compared to the bare chromaticity ones. These discrepancies could be due to the low intensity kicks, which don't allow for a better fit. However, the similarity of the ratios suggests an issue with the decapolar error model of the main dipoles, with measurements showing values about half of those predicted by the magnetic model.

4.5. Accounting for Decay

FiDeL, the field model used in operation, aims at correcting the field errors at various energies. Measurement field errors but also decay estimates with respect to time are used when computing corrections. Decay happens after cycles in the magnets powering. This happens for example when ramping down from an energy of 6.8TeV to 0 and then going back to injection energy at 450GeV. Some components of the magnetic field will persist and gradually change over time until they reach their final value.

Such corrections thus vary with time as decay changes the field errors of the magnets. For the main dipoles, the sextupolar component b_3 increased relative to time while the b_5 component decreases [5].

While sextupolar decay is used by FiDeL, it has been observed that this was not the case for the decapolar component b_5 . The average b_5 field in the main dipoles, taken from the WISE tables and used by FiDeL, is about 1.145 ± 0.5 . Decay measurements for various elements relative to time can be seen in Fig. 4.6. Table 4.6 shows the decay expected

Time [m]	Δb_5
17	-0.38
33	-0.44
50	-0.46
67	-0.47
83	-0.47
167	-0.47

Table 4.6.: Decay of the b_5 component after injection for long time periods [5].

4. Decapolar Fields

at injection energy after a typical cycle of machine operation. From this table, it is clear that decay accounts for a large part of the b_5 at injection. $\approx 40\%$ of the compensated b_5 at injection in the main dipoles can indeed be attributed to the decay.

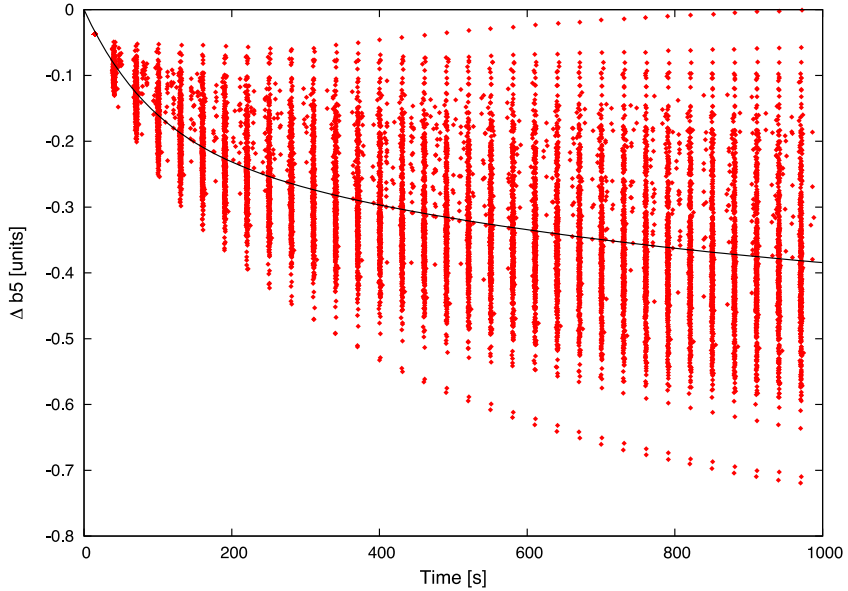


Figure 4.6.: Measured decay of the integrated decapolar field in LHC's main dipoles at injection energy. The fit is shown in black [5].

Chromaticity It has been shown in the previous sections, and particularly in Table 4.4 that measurements and simulations were off regarding the third order chromaticity Q''' . New simulations have hence been conducted to evaluate the effect of this decay on chromaticity. Table 4.7 compares simulations with and without the decay of the b_5 component. The simulations use the 100 available error seeds to calculate error bars.

Condition	$Q'''_x [10^6]$	$Q'''_y [10^6]$
No Decay	6.93 ± 0.04	-4.32 ± 0.02
$\Delta b_5 = -0.47$	4.05 ± 0.04	-2.54 ± 0.02

Table 4.7.: Comparison of Q'''_x and Q'''_y for Beam 1 with and without decay of the b_5 component of the main dipoles at injection energy. Fields errors range from normal and skew sextupoles ($n = 3$) to icosapole ($n = 10$).

Integrating the decay of the b_5 component of the main dipoles in the simulations shows a large reduction of the third order chromaticity Q''' . Using the values from the bare chromaticity measurement and updating Table 4.4 with the newly obtain data provides a more accurate comparison of the model to the measurement, as shown in Table 4.8.

Quantity	Measured [10 ⁶]	Simulated [10 ⁶]	Ratio
Beam 1			
Q_x'''	2.95 ± 0.04	4.05 ± 0.04	0.73 ± 0.01
Q_y'''	-1.82 ± 0.04	-2.54 ± 0.02	0.72 ± 0.02
Beam 2			
Q_x'''	3.06 ± 0.07	4.27 ± 0.03	0.72 ± 0.02
Q_y'''	-1.72 ± 0.02	-2.55 ± 0.01	0.67 ± 0.01

Table 4.8.: Measured and simulated third order chromaticity with octupole and decapole correctors turned off. The simulations include field errors from normal and skew sextupoles to icosapole ($n = 3$ to $n = 10$). The b_5 component of the main dipoles has been updated to include decay.

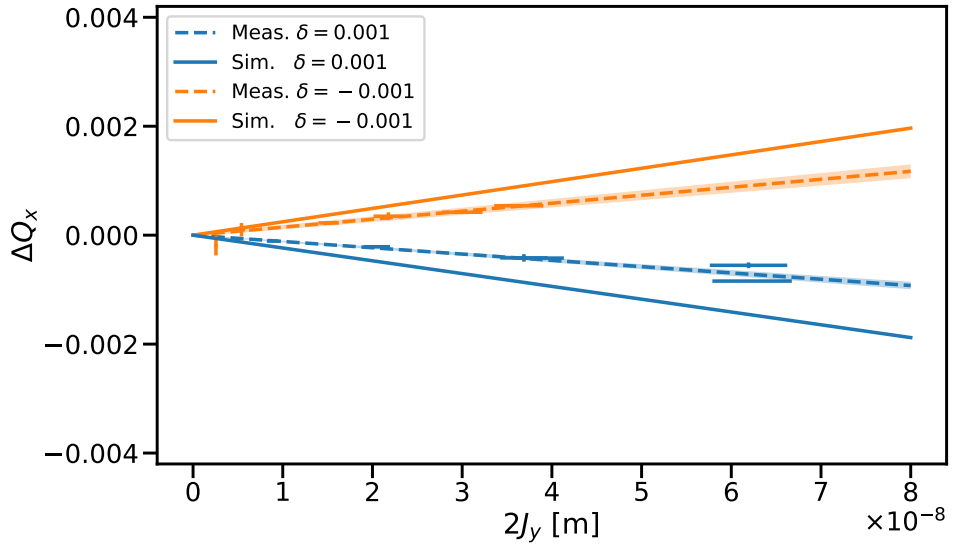
Chromatic Amplitude Detuning Similar to chromaticity, new simulations have been conducted for chromatic amplitude detuning. Table 4.9 gives an overview of the newly computed values and the related ratios relative to the measurements, while Fig. 4.7 gives a visual clue.

Type	$\frac{\partial^2 Q_x}{\partial J_y \partial \delta} [10^4 \text{m}^{-1}]$	$\frac{\partial^2 Q_y}{\partial J_y \partial \delta} [10^4 \text{m}^{-1}]$
$\delta = +0.001$		
Meas.	-1.16 ± 0.08	1.26 ± 0.15
Sim.	-2.35 ± 0.01	1.50 ± 0.01
Ratio	0.49 ± 0.03	0.84 ± 0.10
$\delta = -0.001$		
Meas.	1.47 ± 0.12	-1.18 ± 0.13
Sim.	2.46 ± 0.01	-1.45 ± 0.01
Ratio	0.60 ± 0.05	0.82 ± 0.09

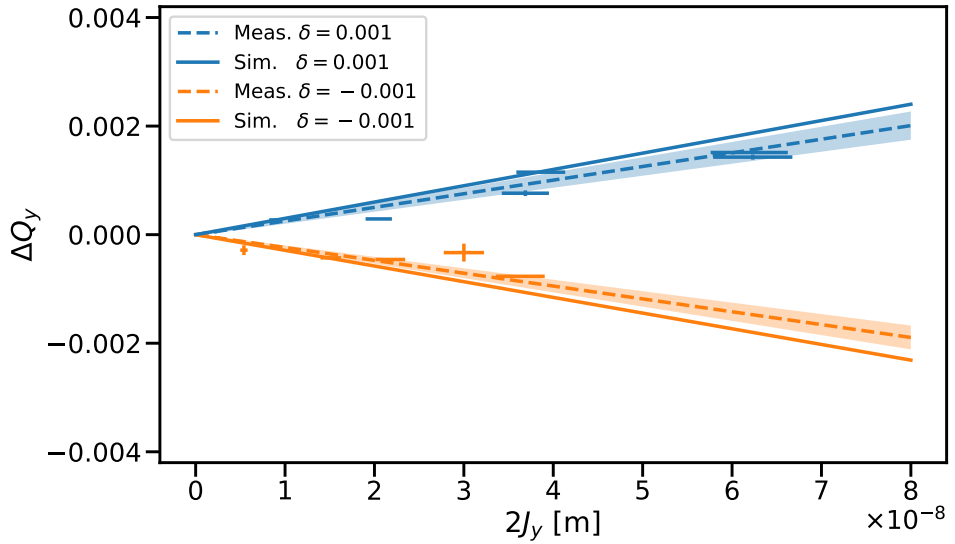
Table 4.9.: Comparison of the measured and simulated terms $\frac{\partial^2 Q_x}{\partial J_y \partial \delta}$ and $\frac{\partial^2 Q_y}{\partial J_y \partial \delta}$ via PTC, at two discrete momentum offsets. Simulations include errors from normal and skew sextupoles to icosapole ($n = 3$ to $n = 10$), as well as the decay of the b_5 component of the main dipoles.

discrepancies between horizontal and vertical ?

4. Decapolar Fields



(a) Horizontal tune shift depending on the vertical action: $\frac{\partial^2 Q_x}{\partial J_y \partial \delta}$.



(b) Vertical tune shift depending on the vertical action: $\frac{\partial^2 Q_y}{\partial J_y \partial \delta}$.

Figure 4.7.: Measured and simulated tune shift depending on the action at two different momentum offsets. Each fit corresponds to a chromatic amplitude detuning term evaluated at a certain δ . Estimates from simulations are lowered due to the b_5 decay of the main dipoles.

4.6. Resonance Driving Terms

Decapoles, due to their order, contribute to many RDTs. Indeed, 50 of them can be theoretically observed in simulations and measurements. In practice, the contributions of individual multipoles become indistinguishable as many resonances or lines overlap, making it impossible to isolate certain terms. Some resonances, described in Appendix C, are unique to certain multipoles when considering no too high orders. Those resonances, provided that they are sufficiently strong and the beam close to them, can be measured via their RDTs.

Of interest to the LHC Operation, is the RDT f_{1004} , driving the resonance $1Q_x - 4Q_y$. It can be seen in the horizontal frequency spectrum at $-4Q_y$ with an amplitude dependence on J_y^2 . Figure Fig. 4.8 shows a frequency map [35] of a simulation including decapolar field errors, where their impact on the beam is easily noticeable. The red particles evolving close to the resonance are affected by it and are subject to large tune shifts. Eventually, those particles are lost when their amplitude becomes too large.

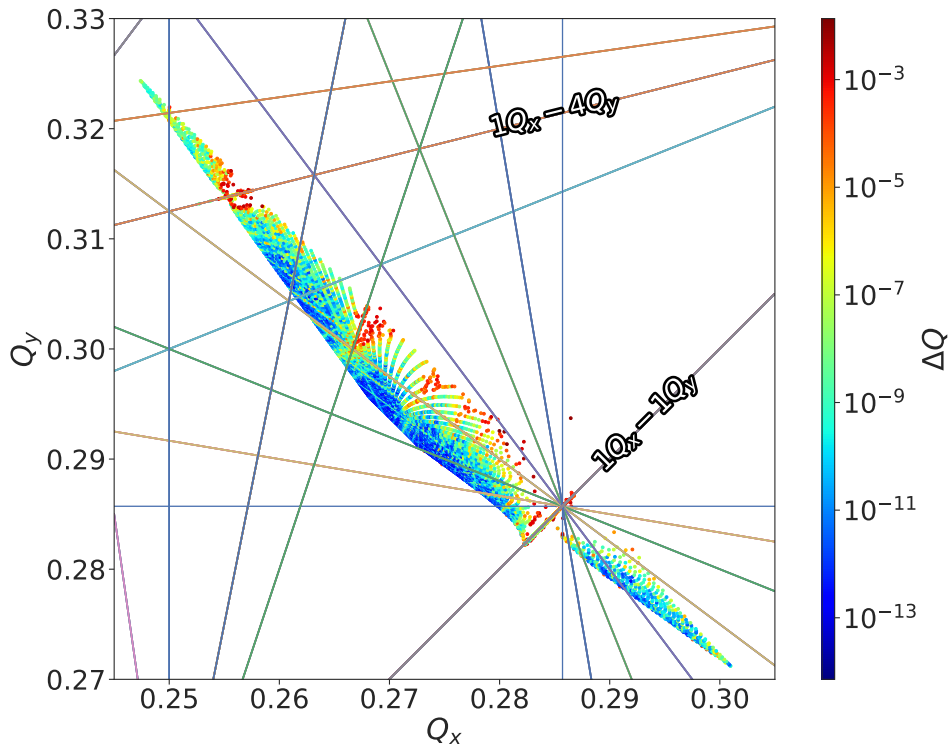


Figure 4.8.: Frequency map at injection energy, with decapolar field errors and nominal settings for landau octupoles. The highlighted resonance (1,-4), excited by decapoles, shows a degradation over 20,000 turns. The tune shift between the start and the end of the simulation is indicated in colour. [change colormap](#)

4. Decapolar Fields

Measuring turn-by-turn data without using any excitation is not a viable option as amplitudes are not large enough. Spectral lines are indeed usually impossible to discern from the noise floor, making RDTs not measurable. Measurements are hence taken with an AC-Dipole, introducing quadrupolar-like field errors in the linear regime [36] and more complex effects in the non linear regime. In practice, those effects are neglected. *Forced* RDTs are measured with an AC-Dipole and treated as *free* as no compensation is applied.

Such forced measurements were taken for the first time in the LHC to observe the f_{1004} RDT at injection energy. The frequency line of the resonance $1Q_x - 4Q_y$ is seen at $4Q_y$ in the horizontal spectrum, as shows Fig. 4.9.

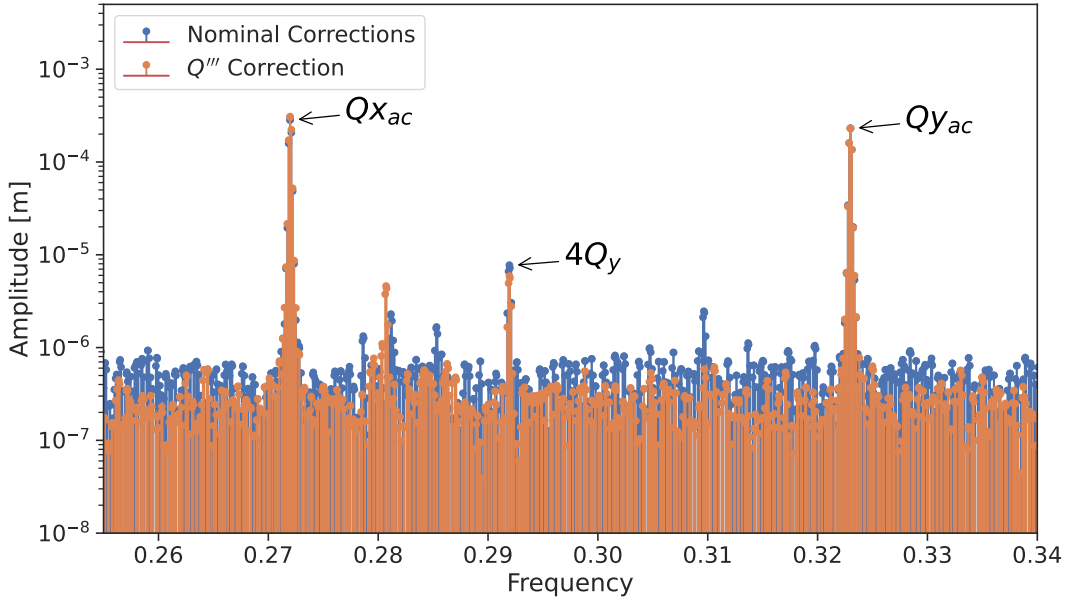


Figure 4.9.: Horizontal frequency spectrum of turn-by-turn data, with nominal and beam-based corrections for the third order chromaticity Q''' . The $1Q_x - 4Q_y$ resonance can be seen at $-4Q_y$ with different amplitudes for each correction scheme.

4.6.1. Decapolar Contribution

Decapolar fields are the main contributors to the RDT f_{1004} . As such, powering the decapolar correctors is a good way to correct the related resonances. Being linear with the strength of the correctors, the RDT can be corrected via a response matrix.

Measurements were taken in order to attempt such a correction and get a baseline for the amplitude of the RDT without decapolar correctors and with the nominal FiDeL corrections applied. Corrections were made on the base of those nominal settings and applied on top. The strength of the decapolar

correctors is shown in Table 4.10 for the FiDeL settings, the delta applied on top and the final correction values.

Circuit	$\text{FiDeL } K_5 [\text{m}^{-5}]$	$\Delta K_5 [\text{m}^{-5}]$	$K_5 [\text{m}^{-5}]$
Beam 1			
RCD.A12B1	-4582	6055	1473
RCD.A23B1	-5106	7	-5099
RCD.A34B1	-4855	3827	-1028
RCD.A45B1	-4577	-4746	-9323
RCD.A56B1	-4125	-4903	-9028
RCD.A67B1	-5166	2961	-2205
RCD.A78B1	-6827	3593	-3234
RCD.A81B1	-5500	2380	-3120
Total	-40738	9174	-31564
Beam 2			
RCD.A12B2	-4490	3639	-851
RCD.A23B2	-5155	-1147	-6302
RCD.A34B2	-4825	-1038	-5863
RCD.A45B2	-4619	3986	-633
RCD.A56B2	-4064	2944	-1120
RCD.A67B2	-5066	2357	-2709
RCD.A78B2	-6866	-2952	-9818
RCD.A81B2	-5446	1825	-3621
Total	-40531	9614	-30917

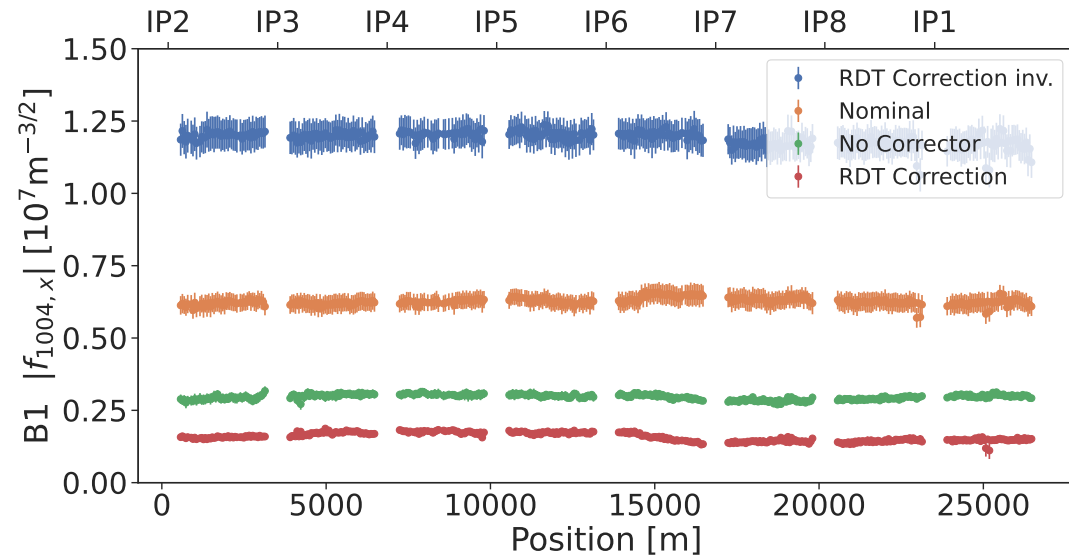
Table 4.10.: Strength of decapolar correctors with nominal FiDeL settings and after application of corrections aiming at reducing both the RDT f_{1004} and Q''' . The total value as a direct incidence on the chromaticity

This RDT correction also serves as a partial Q''' correction. To fully correct Q''' indeed approximately requires a strength of $+13,000K_5$ distributed amongst the correctors. Therefore, this new approach reduces Q''' by about 70% compared to the previous method. The chromatic amplitude detuning terms are also expected to be decreased. Result of those measurements, as well as the inverse of the correction, are shown in Fig. 4.10

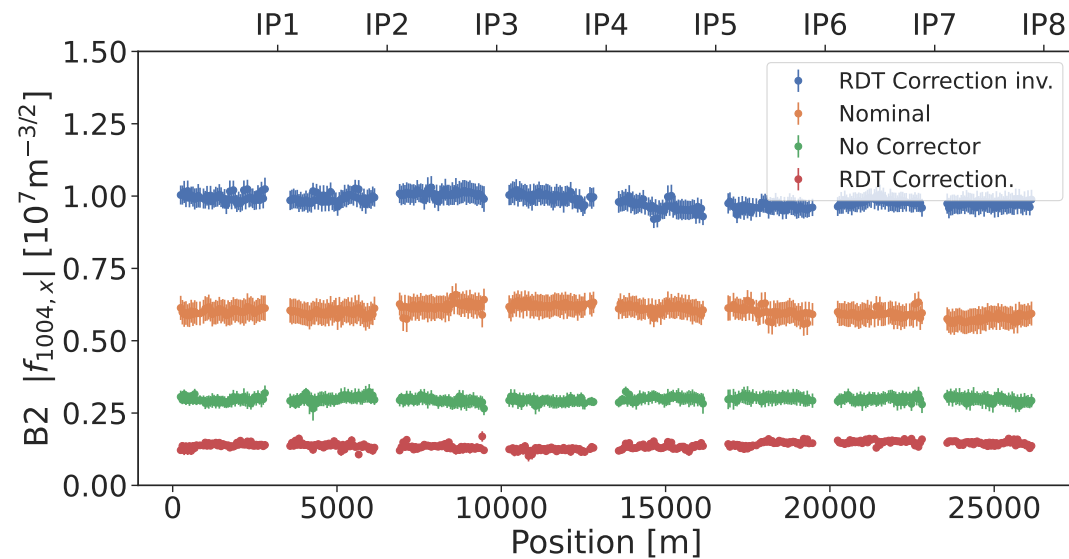
Although the FiDeL scheme was not intended to correct the RDT but rather only Q''' , it would be expected for it to lower the amplitude of the RDT. It can though be seen that it degrades the resonance compared to the machine with no decapolar correctors. On the other hand, the newly computed RDT correction does lower the amplitude of f_{1004} as expected. Its inverse has the opposite effect.

Simulations were run with decapolar correctors turned off and with the absolute value of the RDT correction. The response of the RDT between those two schemes is shown in Fig. 4.11. The difference

4. Decapolar Fields



(a) $|f_{1004}|$ for Beam 1



(b) $|f_{1004}|$ for Beam 2

Figure 4.10.: Measured f_{1004} with decapolar correctors powered off, nominal settings, and combined RDT & Q'''' correction with normal and opposite signs.

between their RMS value ratio is $\approx 6\%$, indicating that simulations correctly model the decapolar correctors.

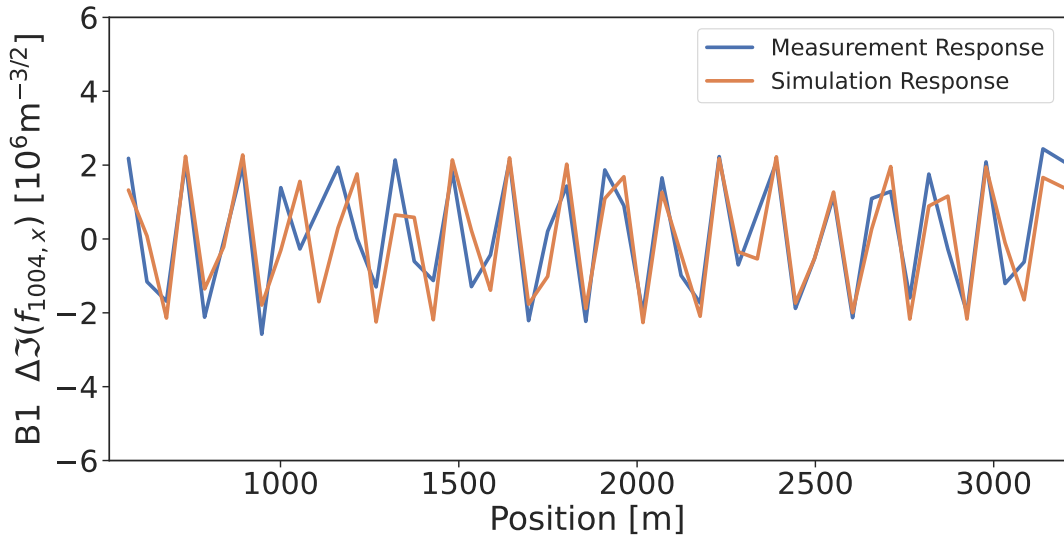


Figure 4.11.: Comparison for measurement and simulation of the response of the imaginary part of f_{1004} upon application on unpowered correctors of the RDT corrections.

4.6.2. Higher Order Contributions

To produce collisions at top energy, *crossing angles* are introduced via the orbit correctors located in the triplets, before the separation dipoles and the matching section of the interaction regions (MCBX, MCBY and MCBC) [37]. Those collisions happen with a small β^* , currently 30cm, requiring strong quadrupolar fields from the triplets.

At such β , those triplets also generate strong dodecapolar field errors. Because of the crossing-angles, feed-down appears and lower-order fields can be observed. Such feed-down to decapolar fields was observed during the first commissioning of Run 3, in 2022 [38]. Fig. 4.12 shows how the RDT f_{1004} , normally affected by decapoles, varies with the application of crossing angles.

Such a contribution is though not expected at injection energy, as the triplets aren't powered as much as at top energy, β^* being set at around 10m.

4.6.3. Lower Order Contributions

First Observation

As described in Appendix A, multipoles can combine to create fields that are seen as higher orders when considering higher orders of the BCH expansion. For decapoles, combinations of several sextupoles and sextupoles with octupoles give rise to decapolar-like fields, as described in Table A.3. The following parts of this section will describe those combinations.

4. Decapolar Fields

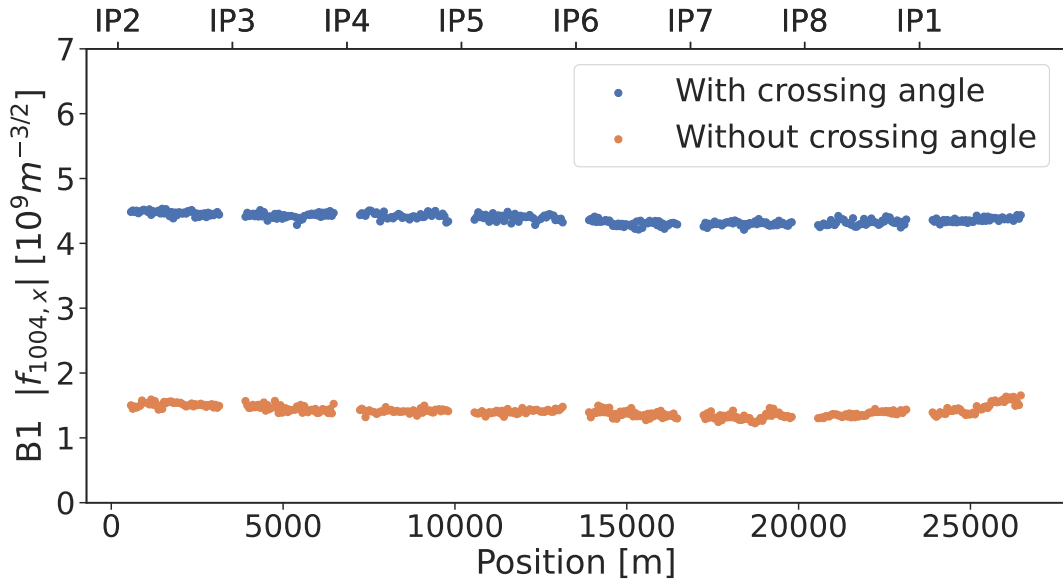


Figure 4.12.: Varying amplitude of the decapolar RDT f_{1004} depending on the activation or not of the crossing angle at the IP. Offsets in orbit create feed-down from higher orders.

This effect was observed in 2022 during Run 3's commissioning. New corrections of the non-linear chromaticity Q'' and Q''' were performed, and RDT measurements taken before and after their correction. As Q''' was corrected, the expectation was that the RDT f_{1004} would also lower with the reduction of the decapolar strengths K_5 . However, an increase of the RDT was observed, as shows Fig. 4.13.

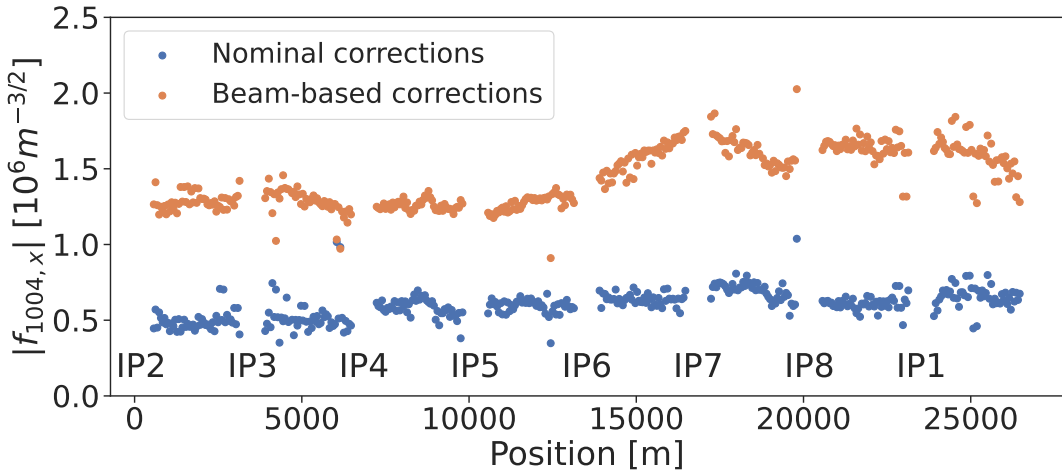


Figure 4.13.: Non intuitive increase of the RDT f_{1004} after application of both the Q'' and Q''' corrections.**redo plot**

Action Dependence and Analysis

Resonance lines in the frequency spectrum are often contributed to by several multipoles. Some lines start getting a contribution with rather high multipole orders, like the RDT f_{1004} considered here. The line $4Q_y$ in the horizontal spectrum is indeed contributed to by decapoles and then only by decatetrapoles. When the main contributing field alone is varied, it is easy to reconstruct the RDT, as its fit is only dependant its action dependence ($\propto J_x J_y^*$). Several turn-by-turn measurements at the same configuration can be taken with varying kick amplitudes, refining the RDT value with more data points for the fit.

Considering the contribution of lower order multipoles is a bit trickier, as the second order RDTs change the dependence of the frequency line [39]. In order to be able to compare the RDT from several turn by turn measurements, the same kick amplitude must then be used. Failing to do so would lead to a poor fit of the line amplitude relative to the action, resulting in an RDT with incorrect amplitude and significant noise.

Sextupoles

At the third order of the BCH expansion, the combination of two sextupoles yields a decapolar-like expression. This means that, during normal operation of the machine, decapolar observables will be altered when adjusting parameters such as the linear chromaticity Q' . Derivation of such a combination can be found in Appendix A.2.2. The resulting Hamiltonian indeed is similar to the terms of a decapole, dropping the $p_{x,y}$ terms for readability:

$$(H_3)^3 \propto \frac{1}{48} \left(x^5 - 2x^3y^2 - 3xy^4 \right) \\ \sim x^5 - 10x^3y^2 + 5xy^4. \quad (4.5)$$

To quantify the actual impact of such an equation on the LHC, a simulation was run with injection optics while varying this same linear chromaticity Q' . No higher fields than sextupoles are have been included, including field errors. The resulting effect on the RDT f_{1004} can be seen in Fig. 4.14.

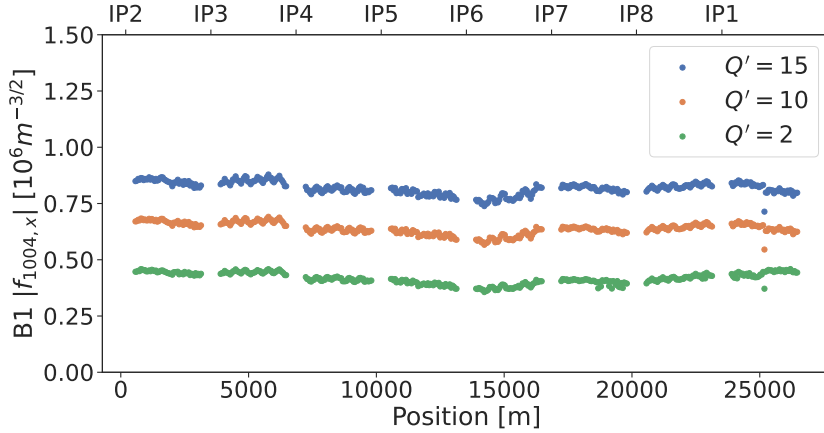


Figure 4.14.: Simulated change of the decapolar RDT f_{1004} with varying linear chromaticity Q' generated by sextupoles. The combination of sextupolar fields clearly shows a increase in decapolar RDT.

As the linear chromaticity increases, the overall K_3 strength of sextupoles actually becomes more negative. Considering the previous Eq. (4.5), a higher chromaticity is expected to increase the amplitude of the RDT f_{1004} , related to the last term xy^4 . Fig. 4.15 shows how the RDT is expected to vary, depending on the overall sextupoles strength and the linear chromaticity. It can be noted that although the relation between K_3 and Q' is linear, that of K_3 and the RDT varies with the cubed strength. Using the sum of the cubed strength is possible due to the chromaticity knob being a factor applied on all sextupoles at the same time.

To confirm what is observed in simulations, measurements were performed by varying Q' and kicking the beam with the AC-Dipole. Limited by losses, up to three measurements with distinct Q' were taken, as shows Fig. 4.16.

Like in simulations, it is observed that an increase in Q' translates to an increase in $|f_{1004}|$. The scale of the amplitude is though one order of magnitude higher than that of simulations. An offset for all measurements could be explained by non-included field-errors. The shift between them however should be similar between machine and simulations, this could be due by the interaction of the sextupolar

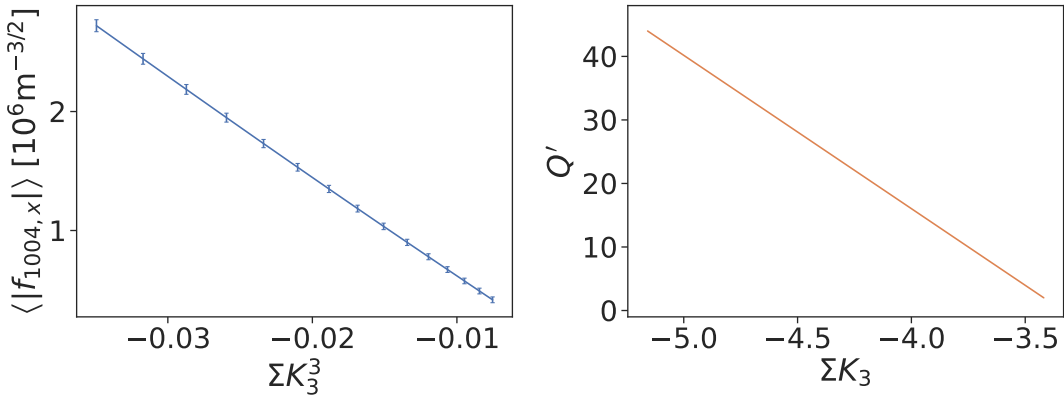


Figure 4.15.: Average amplitude of the decapolar RDT f_{1004} depending on the overall strength of the sextupoles used to control the linear chromaticity Q' . The right plot can be used to relate the RDT amplitude to a specific Q' value.

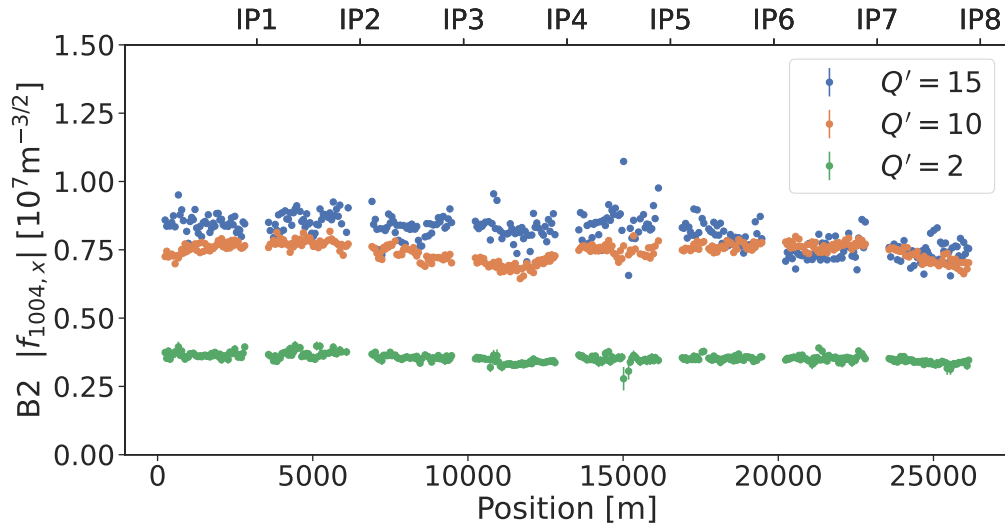


Figure 4.16.: Measured change of the decapolar RDT f_{1004} depending of the desired linear chromaticity Q' generated by sextupoles. It is to be noted that the vertical axis is one order of magnitude higher than the previous simulations' plot.

fields with octupoles, as detailed in the following section. More data points with varying Q' at similar kick amplitudes would be required to further investigate.

Sextupoles and Octupoles

At the second order of the BCH expansion, the combination of a sextupole and an octupole yields a decapolar-like expression. Like sextupoles, octupoles are used in operation, thus contributing to decapolar fields. This happens amongst other when correcting the second order chromaticity Q'' and most importantly with the Landau Octupoles, which are powered to high strengths at injection energy to introduce Landau damping [2]. Derivation of such a combination can be found in Appendix A.2.3. The resulting Hamiltonian indeed is similar to the terms of a decapole, dropping the $p_{x,y}$ terms for readability:

$$\begin{aligned} H_3H_4 &\propto \frac{1}{24} (x^5 + 2x^3y^2 + xy^4) \\ &\sim x^5 - 10x^3y^2 + 5xy^4. \end{aligned} \quad (4.6)$$

In order to assess the previous equation, simulations were run with several configurations. As seen previously, a combination of two sextupoles creates a decapolar-like field, varying their field is thus not needed. Rather, a set of two configurations was run to check the impact of octupoles alone. The first configuration is ran with all sextupoles of the machine turned off, while octupoles are powered. The second configuration turns off all sextupoles and octupoles. Fig. 4.17 shows the resulting RDT f_{1004} from these simulations. It is there apparent that varying octupoles without sextupoles does not have any effect on this RDT.

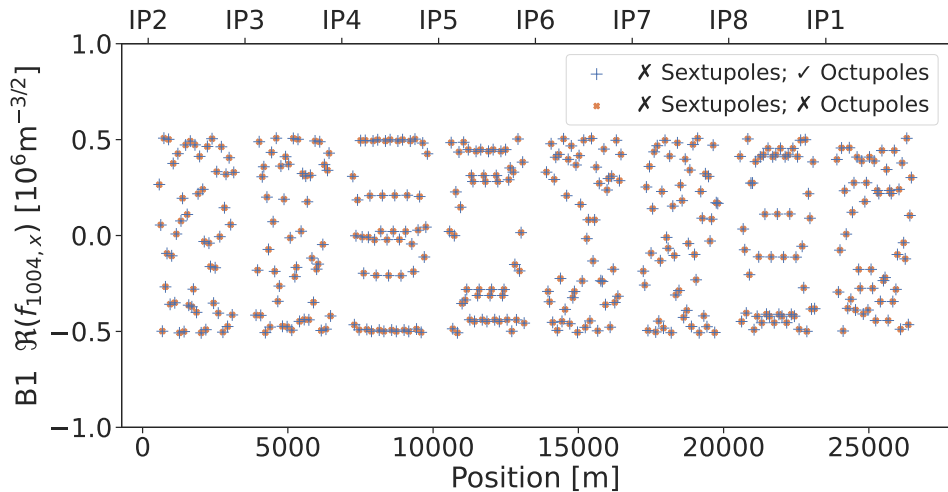


Figure 4.17.: Simulated decapolar RDT f_{1004} with two different schemes. First scheme has lattice sextupoles turned off and octupoles turned on. Second scheme has all sextupoles of the lattice turned off and octupoles turned off as well. No difference is seen, as expected from the equations.

The most powerful octupoles used in operation are the lattice octupoles, used for Landau damping. Fig. 4.18 shows a simulation ran with varying strengths of those magnets. It can be noted here that the shift of the RDT is almost of an order of magnitude, making octupoles a large contributor to the decapolar fields.

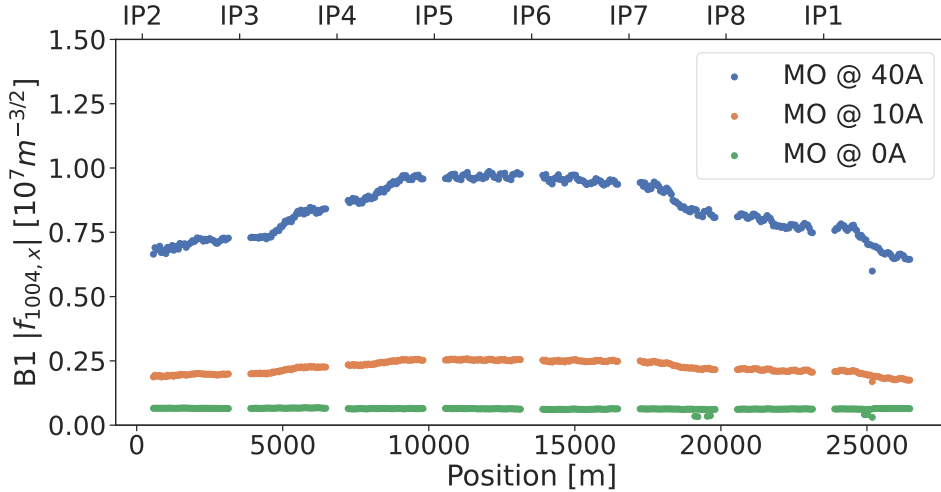


Figure 4.18.: Simulated change of the decapolar RDT f_{1004} depending of the strength of the lattice octupoles used for Landau damping.

While decapoles are expected to be the main contributors to decapolar fields, other strong sources can indeed be identified. Fig. 4.19 shows the average amplitude of the RDT f_{1004} depending on the error sources introduced in the simulations. A large contribution comes from the octupolar errors in the main dipoles, being actually larger than the decapolar errors in those magnets.

Measurements were performed to confirm and quantify the effect of octupoles coupled with sextupoles on the decapolar fields. Previous corrections, aimed at correcting the second order chromaticity Q'' , via octupolar correctors MCO, were applied with varying factors. Such corrections apply use a uniform trim on all correctors of $\approx +2.5K_4$. Fig. 4.20 shows a comparison of the resulting RDT with those corrections at factors $-10, -4, -1$ and 0 .

Table 4.11 shows the RMS of the amplitude of this RDT for the various configurations. Similar to the shift observed when powering the landau octupoles in simulations, the shift is of one order of magnitude between factors -0 and -10 . Measurements with landau octupoles were also attempted but losses made it impossible to obtain high enough amplitudes to correctly measure the RDT.

Factor	RMS $ f_{1004} $
-10	37, 308, 159
-4	6, 721, 270
0	3, 533, 796
-1	2, 333, 384

Table 4.11.: RMS of $|f_{1004}|$ depending on the factor of the Q'' corrections.

4. Decapolar Fields

4

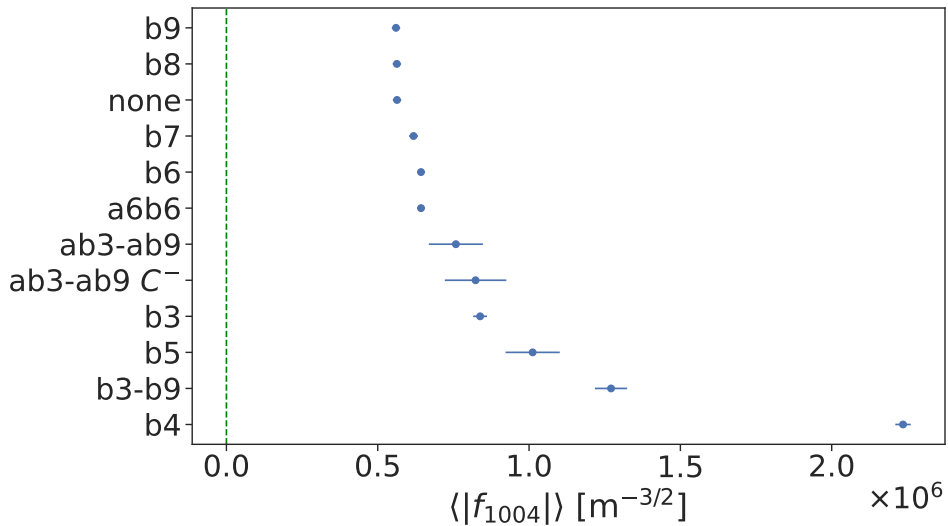


Figure 4.19.: Simulation of the amplitude of the decapolar RDT f_{1004} depending on the field errors applied on main dipoles as well as coupling (C^-). While it is apparent that some multipolar errors drive the resonance higher, some combinations actually seem to cancel each other.

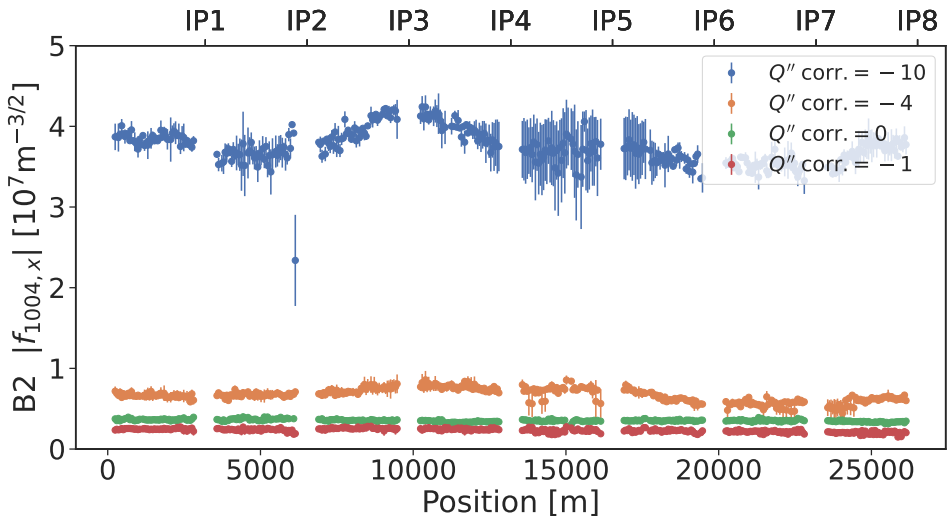


Figure 4.20.: Shift of the decapolar RDT f_{1004} depending on the factor applied on octupolar corrections for Q'' .

Simulated and observed large shifts due to octupoles are relevant to the operation of the LHC, as resonances can be greatly deteriorated, especially when powering Landau octupoles. A better understanding of the interaction between Landau octupoles and octupolar correctors could lead to improved corrections in not only octupolar but also decapolar fields in the future.

4.7. Impact of Decapolar Fields

Decapolar fields can influence the beam lifetime in several ways. Chromatic amplitude detuning and chromaticity will induce a tune shift, relative to either or both the action and the momentum offset. After such detuning, particles may move closer to certain resonances in tune space, causing their oscillations to grow, eventually leading to their loss.

4.7.1. Large RDT

As seen previously in Fig. 4.8, the resonance $1Q_x - 4Q_y$ passes through the beam in tune space, deteriorating the lifetime of the nearby particles. In order to measure the impact of this resonance on the beam, a knob was created, alternating the current of all decapole correctors in the machine arc by arc. Such a powering scheme has no impact on chromaticity as the sum of the strengths K_5 is zero. Rather, the RDT f_{1004} is impacted. Is it to be noted that this is not a correction, but purely a way to artificially increase the RDT in order to quantify the effect of the resonance.

Starting with nominal corrections for Q''' corrections, a delta of $\pm 10500K_5$ is applied on each decapolar correctors. Fig. 4.21 shows the response of the real part of the RDT for this scheme and its inverse. The amplitude of the RDT is on a similar level as the shift is significantly larger than the original level of the RDT. Table 4.12 indicates the amplitude of the RDT created with each knob value.

In order to measure the lifetime, a long period must be allocated as the signal returned from monitors can be jittery. Fig. 4.22 shows this lifetime depending on the decapolar strength scheme applied. The current of only one circuit is shown for readability. A current of ≈ 230 corresponds to a knob value of $+10500$ while a current of -45 corresponds to 0.

It is clear from this measurement that a large RDT decreases the lifetime of the beam. The first pair of trim sees the average lifetime decreasing of 0.31 ± 0.03 hours, while the second one sees a decrease of 0.36 ± 0.03 hours. This observed decrease of 20 minutes accounts for 10% of the beam lifetime at injection energy.

4.7.2. Corrections

In order to understand what can be gained from correcting decapolar fields, a lifetime measurement was taken with the corrections described in Section 4.6.1. This scheme corrects the three decapolar

ΔK_5	RMS $ f_{1004} $
0	618,947
± 10500	17,566,377
∓ 10500	17,623,867

Table 4.12.: RMS of $|f_{1004}|$ relative to the powering scheme of decapolar correctors.

4. Decapolar Fields

4

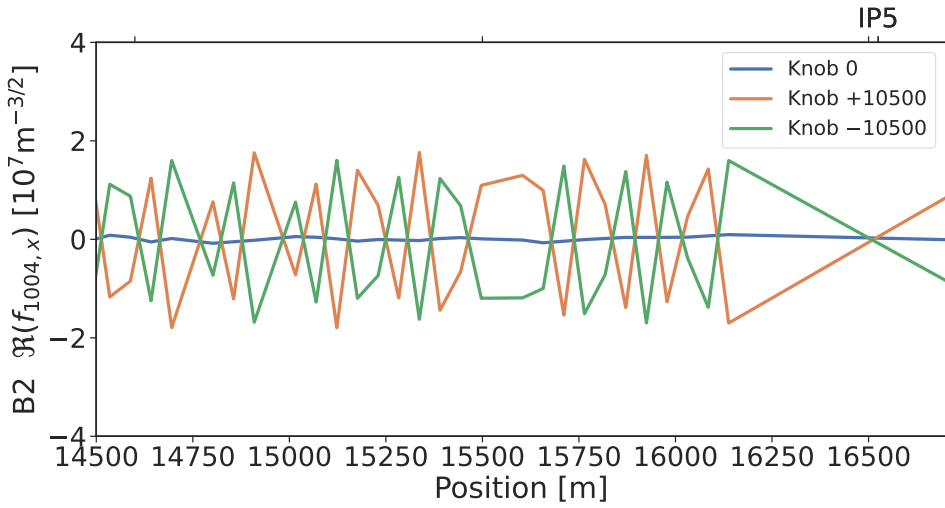


Figure 4.21.: Measured real part of the RDT f_{1004} depending on the powering scheme of the decapolar correctors.

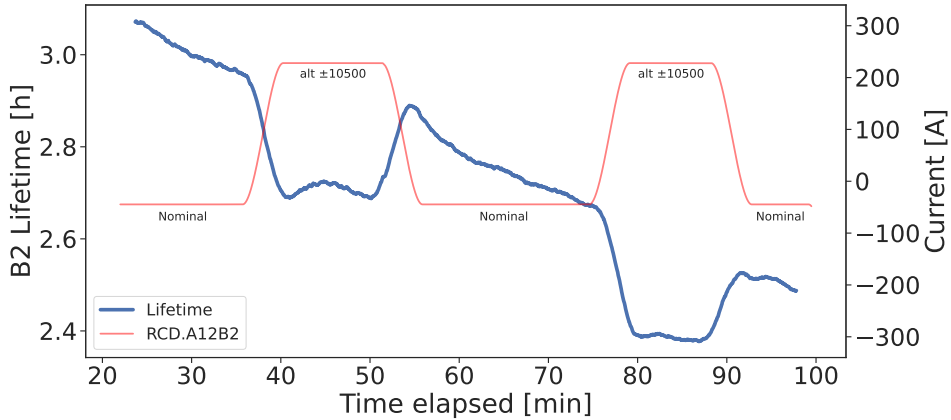


Figure 4.22.: Measured lifetime of Beam 2 upon application of two different powering schemes for decapolar correctors. One trim keeps the RDT at a low amplitude while the other greatly amplifies it.

observables, being the RDT f_{1004} linked to the resonance $1Q_x - 4Q_y$, the third order chromaticity Q''' and the chromatic amplitude detuning terms.

Fig. 4.23 shows the evolution of the lifetime, starting with corrections applied, removed and then trimmed to their opposite. A net change in lifetime for Beam 1 can be measured after each application. Acquired signal for Beam 2 has been deemed to noisy to be relevant, due to the shortness of the measurement.

4.7. Impact of Decapolar Fields

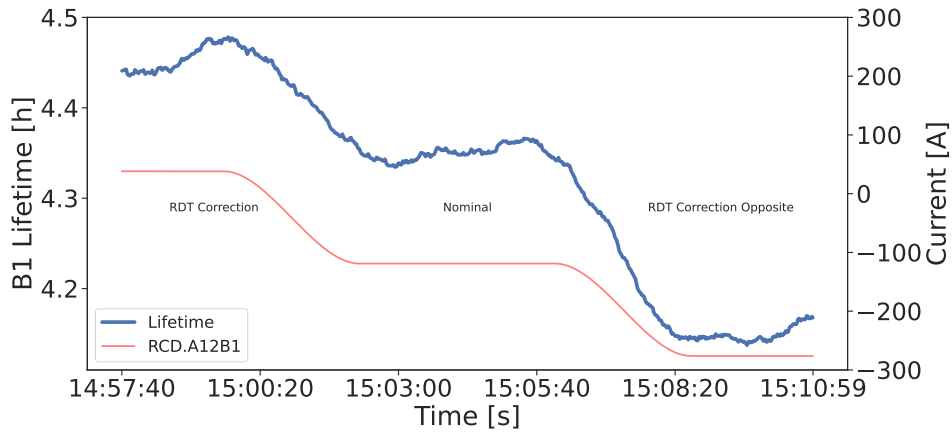


Figure 4.23.: Measured lifetime of Beam 1 with the nominal corrections for Q''' , combined correction of f_{1004} and Q''' , and its inverse.

It is apparent here that the corrections have a beneficial effect on the Beam. The lifetime improvement is of $\approx 3\%$, while the degradation after applying the opposite is of $\approx 5\%$.

Higher Order Fields

5.1. Introduction

Beam-based high order field measurements have been carried out in the LHC since its first Run^{cite}, via chromaticity studies. Those measurements, made by varying the RF frequency while observing the resulting tune change, have been performed with a momentum offset of up to $\delta = \pm 2.2 \times 10^{-3}$, which led to the observation of the third order term of the non-linear chromaticity.

During the commissioning of Run 3, a new collimator sequence has been introduced, allowing wider momentum offset measurements, within $\delta \in [-3.2 \times 10^{-3}, 3.7 \times 10^{-3}]$. This improved setup led to the observation of the fourth and fifth order terms at injection energy. Those terms, denoted $Q^{(4)}$ and $Q^{(5)}$ respectively in Eq. (5.1), are produced to first order by dodecapoles and decatetrapoles. Dodecapoles being powered off at injection and decatetrapoles being absent from the lattice, those fields originate from the field errors of the various magnets installed.

$$Q(\delta) = Q_0 + Q' \delta + \frac{1}{2!} Q'' \delta^2 + \frac{1}{3!} Q''' \delta^3 + \frac{1}{4!} Q^{(4)} \delta^4 + \frac{1}{5!} Q^{(5)} \delta^5 + O(\delta^6). \quad (5.1)$$

Completing measurements of high orders fields taken via chromaticity scans, turn-by-turn measurements were also performed. High amplitude kicks indeed made the observation of dodecapolar RDTs visible for the first time in the LHC

5.2. Chromaticity

5.2.1. Measurement Procedure

As described in Section 3.3.2, the momentum offset δ is related to the RF frequency and the momentum compaction factor. This relation is given as a simplified form in Eq. (5.2). The model α_c for the LHC injection optics is 3.48×10^{-4} for beam 1 and 3.47×10^{-4} for beam 2. Via this relation, a change of 140Hz of the RF frequency corresponds to a momentum offset of about -0.001 .

5

$$\delta = -\frac{1}{\alpha_c} \cdot \frac{\Delta f_{RF}}{f_{RF,nominal}}. \quad (5.2)$$

To properly characterize higher orders of the chromaticity function and ensure quality measurements, several steps are required. The tune measured during chromaticity scans can exhibit jitter and resonance lines may appear, requiring thorough data cleaning to either reject problematic data points or reduce error bars. The simplified Eq. (5.2), describing δ , has been sufficient for reliably measuring up to the third order chromaticity. However, this relation also needs verification.

Noise and Spectral Lines

Noise lines, due to electronics, can be seen in the raw data obtained from the BBQ tune system. Occasionally, when those resonances are strong, their frequency peak can be mistaken as the tune and logged as such by the system. This yield large uncertainties in the measurement when data points can't properly be classified as outliers. A tune measurement presenting this issue is showed in Fig. 5.1.

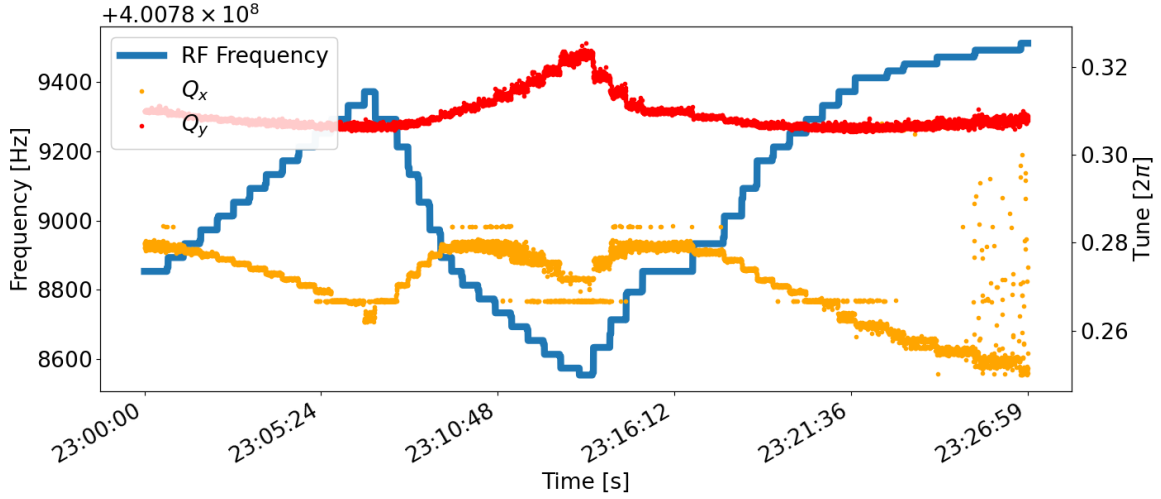


Figure 5.1.: Shift of the tune by variation of the RF. Noise lines can appear in some cases, making the tune error bar large or downright unusable.

A solution to this issue is to use the raw data extracted from the BBQ system. From there, a spectrogram clearly shows the noise lines, as seen in Fig. 5.2. Those lines have been repeatedly identified over several measurements and confirmed to be fixed. The highest peak of the spectrogram can thus be safely identified by removing those resonances, yielding a cleaner measurement. It is also to be added that the BBQ requires to set a tune window, which can be forgotten. By analyzing the raw data, it is ensured that the measurement has usable data and does not try to measure noise.

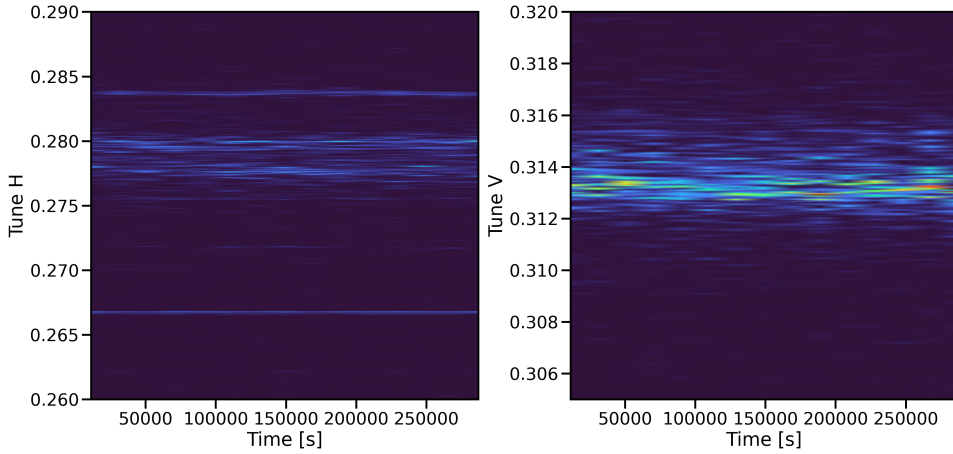


Figure 5.2.: Tune spectrogram obtained via BBQ system. Strong resonance lines can be seen above and below where the tune really is, causing the wrong frequency peak to be identified as the tune.

Momentum Compaction Factor

Rather than a constant, the momentum compaction factor can be expressed as an expansion, as detailed in Section 2.5.4. The first terms are given by the following,

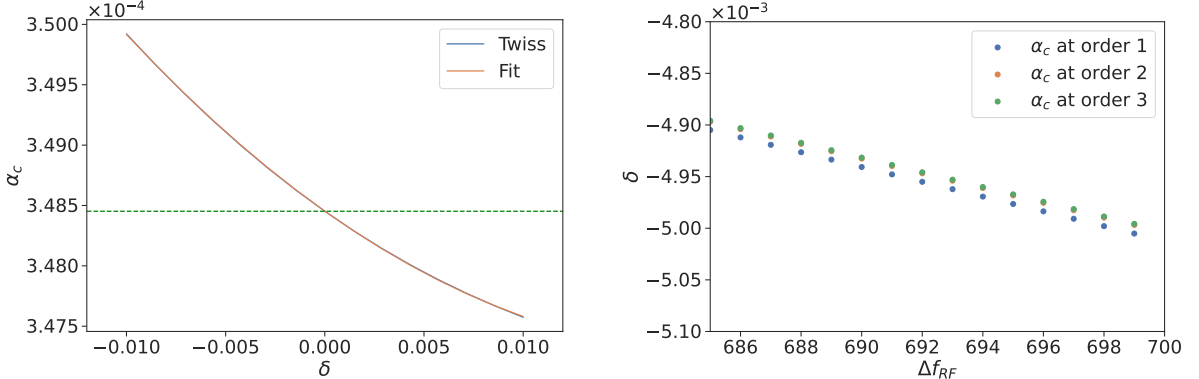
$$\alpha_c = \underbrace{\alpha_{c,0}}_{1^{\text{st}} \text{ order}} + \underbrace{\alpha_{c,1}\delta}_{2^{\text{nd}} \text{ order}} + \underbrace{\alpha_{c,2}\delta^2}_{3^{\text{rd}} \text{ order}}. \quad (5.3)$$

The expression for δ at first and second order then reads,

$$\begin{aligned} \delta &= -\frac{\Delta f_{RF}}{\alpha_0 f_{RF}} && \Rightarrow \text{Order 1} \\ \delta &= \frac{-\alpha_0 f_{RF} + \sqrt{f_{RF}(-4\Delta f_{RF}\alpha_1 + \alpha_0^2 f_{RF})}}{2\alpha_1 f_{RF}} && \Rightarrow \text{Order 2} \end{aligned} \quad (5.4)$$

5

It is assumed that only the first term is relevant as the induced difference in chromaticity is negligible as will be demonstrated later on. Fig. 5.3 shows the non linearity of the momentum compaction factor and its effect on the calculated δ via the previous formulas.

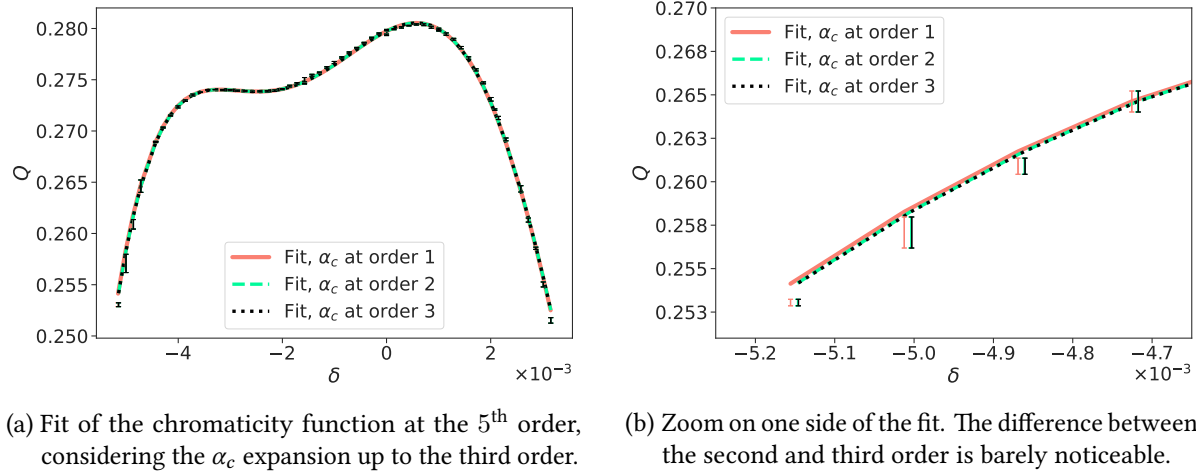


(a) Non-linear fit of α_c obtained via an evaluation at discrete δ in MAD-X. The green line represents a constant $\alpha_c = \alpha_{c,0}$.

(b) Divergence of the momentum offset when considering higher α_c orders with large RF trims.

Figure 5.3.: Non linearity of α_c and its effect on the computed δ via RF trims. The simulations are done at injection energy of 450GeV.

It is observed that while clearly depending on higher orders, the momentum compaction factor only has a small impact on the calculated δ . Fig. 5.4 shows a real-life measurement, comparing the fit of the chromaticity function with various δ , computed up to the third order of α_c .

Figure 5.4.: Fit of the chromaticity function considering several α_c orders.

The fit of the chromaticity function is barely impacted when considering the higher orders of the momentum compaction factor. The different orders of the chromaticity are collected in Table 5.1. The higher order terms of α_c can thus be neglected and are not a source of higher chromaticity orders.

Chromaticity	α_c order		
	1	2	3
$Q^{(1)}$	2.52 ± 0.03	2.53 ± 0.03	2.53 ± 0.03
$Q^{(2)}$	-3.04 ± 0.05	-3.05 ± 0.05	-3.05 ± 0.05
$Q^{(3)}$	-4.75 ± 0.03	-4.75 ± 0.03	-4.75 ± 0.03
$Q^{(4)}$	-0.33 ± 0.07	-0.32 ± 0.07	-0.32 ± 0.07
$Q^{(5)}$	2.33 ± 0.06	2.36 ± 0.06	2.36 ± 0.06

Table 5.1.: Chromaticity values obtained for the same measurement, depending on the order of the momentum compaction factor taken into account.

Momentum Offset from Orbit

During machine operation, the momentum offset, derived from the orbit, used to be logged on the servers. It was then possible to directly compute the chromaticity that way without having to use the RF and the momentum compaction factor. In 2016, measurements of the non-linear chromaticity were performed using the former method. Fig. 5.5 shows a comparison of the obtained non-linear chromaticity from both methods, while Table 5.2 shows a numerical comparison. Results being similar, it is deemed that both methods are reliable to measure the non-linear chromaticity in the LHC.

5. Higher Order Fields

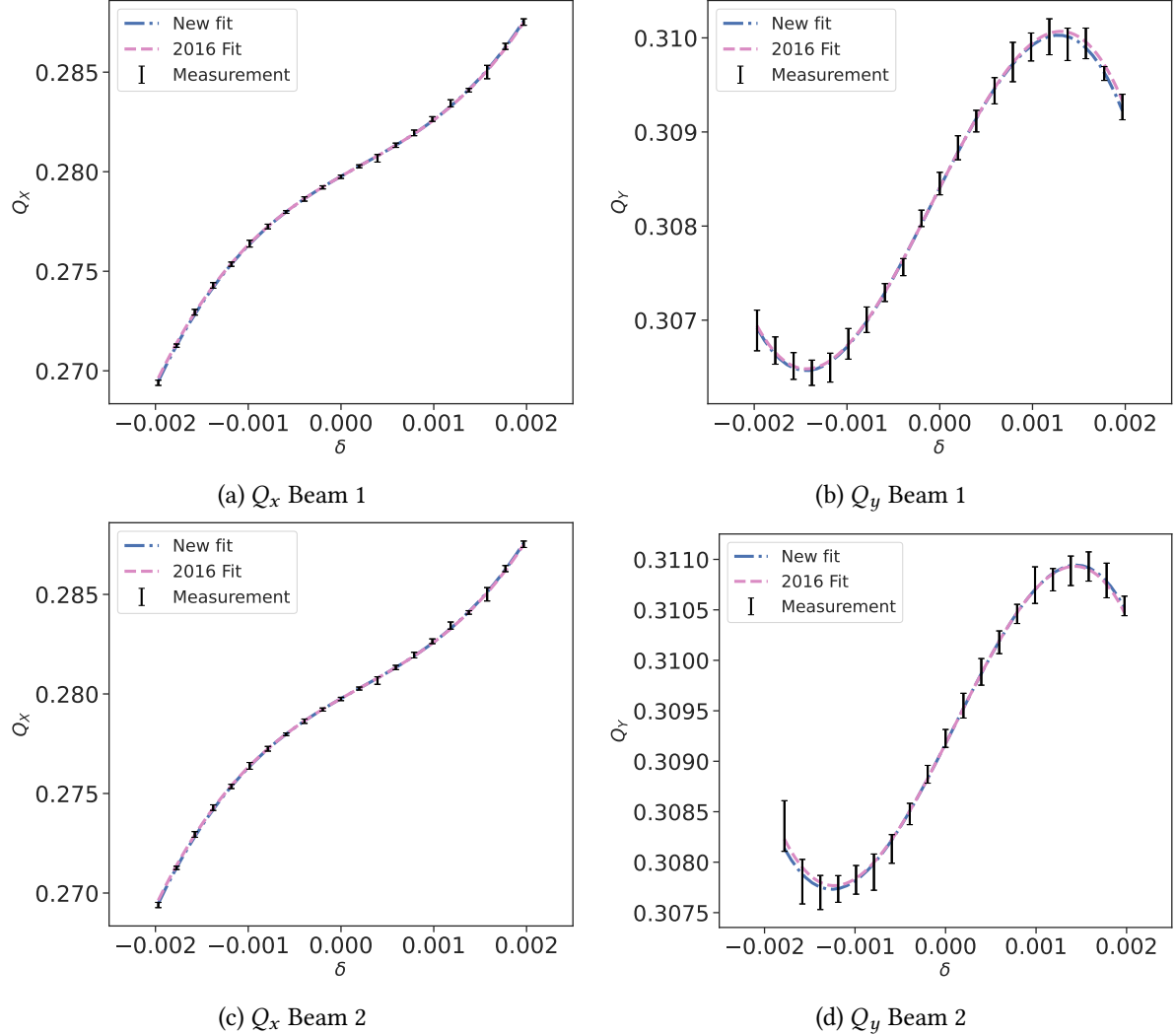


Figure 5.5.: Comparison of the non-linear chromaticity fit obtained from the computed momentum offset via the RF in 2022 and from the logged values in 2016.

5.2.2. Performed Measurements

In order to assess the correctness of the observation of higher chromaticity orders, measurement repeatability is needed. Two measurements were thus taken, with different configurations pertaining top the correction of the second and third order chromaticities Q'' and Q''' .

Those two chromaticity measurements were indeed performed with different settings. The first one used the nominal correction strengths for octupole and decapole corrector magnets, derived from magnetic measurements, where the second one used beam-based corrections for the same elements,

Plane	δ via RF		δ via orbit	
	$Q''[10^3]$	$Q'''[10^6]$	$Q''[10^3]$	$Q'''[10^6]$
Beam 1				
X	-0.64 ± 0.01	3.00 ± 0.04	-0.62 ± 0.01	2.91 ± 0.04
Y	-0.17 ± 0.01	-2.12 ± 0.04	-0.14 ± 0.01	-2.09 ± 0.04
Beam 2				
X	-1.18 ± 0.02	2.89 ± 0.06	-1.23 ± 0.03	3.13 ± 0.11
Y	0.18 ± 0.02	-1.95 ± 0.05	0.20 ± 0.02	-2.02 ± 0.06

Table 5.2.: Comparison of the chromaticity values obtained for the same measurement via two different methods to acquire δ .

computed from measurements. Those two measurements have a respective momentum-offset range of $[-3.1 \times 10^{-3}, 3.1 \times 10^{-3}]$ and $[-3.2 \times 10^{-3}, 3.7 \times 10^{-3}]$.

In order to stay consistent, both measurements saw their horizontal and vertical tunes respectively set to $Q_x = 0.28$ and $Q_y = 0.31$. The linear chromaticity Q' is set to a small value of 2 to avoid large tune shifts.

Nominal Corrections

This first chromaticity measurement was performed during the LHC beam commissioning in April 2022, as part of the routine measurements and corrections performed after every technical or long shutdown. The octupole and decapole correctors were set to their nominal settings, aimed at correcting Q'' and Q''' , as previously described in [ref decapole chapter](#).

Results of this initial measurement are shown in Tab. 5.3. Lower order chromaticities such as Q' and Q'' are consistent with previous measurements [31].

Plane	$Q^{(2)}[10^3]$	$Q^{(3)}[10^6]$	$Q^{(4)}[10^9]$	$Q^{(5)}[10^{12}]$
Beam 1				
X	-2.44 ± 0.02	-3.36 ± 0.04	-0.56 ± 0.02	1.20 ± 0.07
Y	0.97 ± 0.02	1.62 ± 0.05	0.15 ± 0.03	-0.88 ± 0.09
Beam 2				
X	-2.45 ± 0.03	-2.72 ± 0.08	-1.00 ± 0.05	0.15 ± 0.14
Y	0.79 ± 0.03	1.54 ± 0.06	0.24 ± 0.04	-0.74 ± 0.13

Table 5.3.: Terms of the high order chromaticity obtained during Run 3 commissioning in April 2022, with nominal corrections.

Due to the momentum offset being zero several times during the measurement, it was possible to

determine that the tune drift is negligible. The measurement was also performed after an extended period at injection energy, where the b_3 decay is small and not causing any change in the first order chromaticity. The fitted curve for the chromaticity function is shown in Fig. 5.6. It can be seen that a higher order polynomial is beneficial for the fit, as discussed further in "[Q^{\(4\)} and Q^{\(5\)} fit quality](#)".

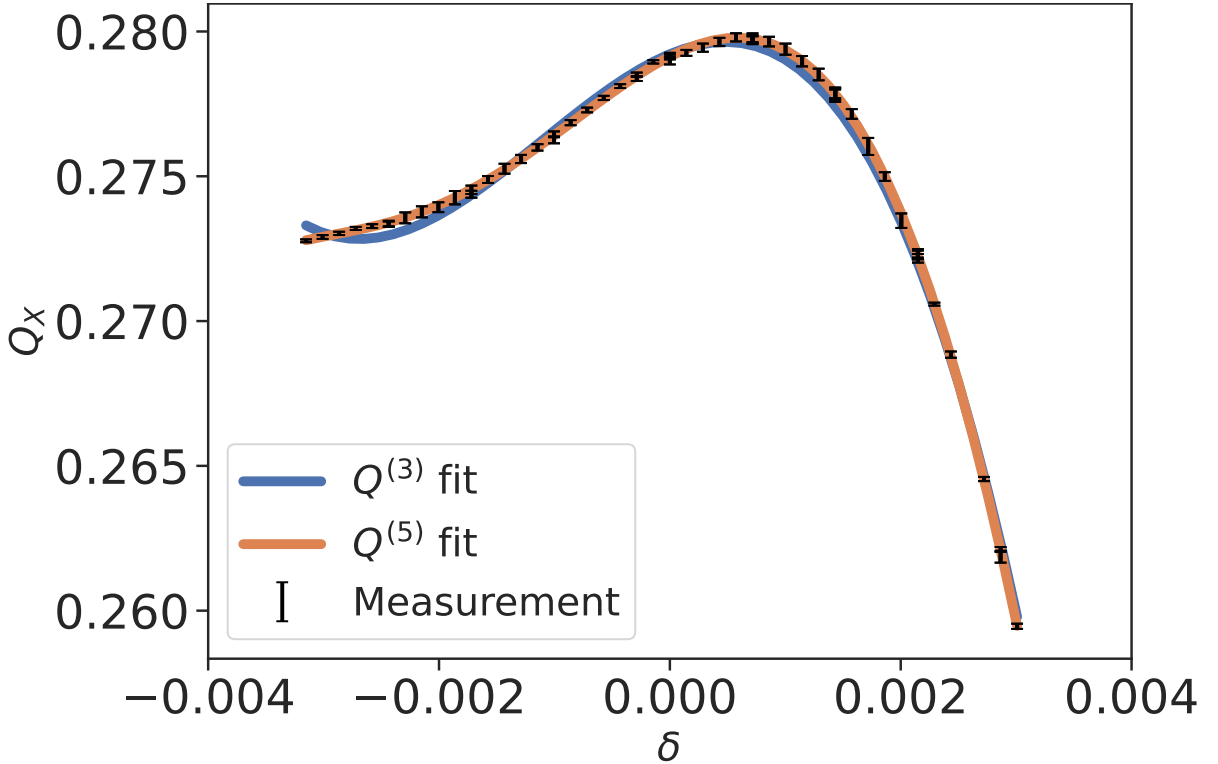


Figure 5.6.: Beam 1 measurement of higher order chromaticity terms with nominal corrections used during operation. Fits are up to the third and fifth order.

Beam-Based Corrections

After correcting the second and third order chromaticities via the octupole and decapole correctors, a second measurement was performed. A uniform trim on all the correctors of each class was applied for each beam, resulting in a global correction. A total of four circuits were unavailable for the octupoles, three for beam 1 and one for beam 2, resulting in larger corrections for beam 1. Corrections applied on top of the nominal settings [31] for the octupoles and decapoles are shown in Tab. 5.4.

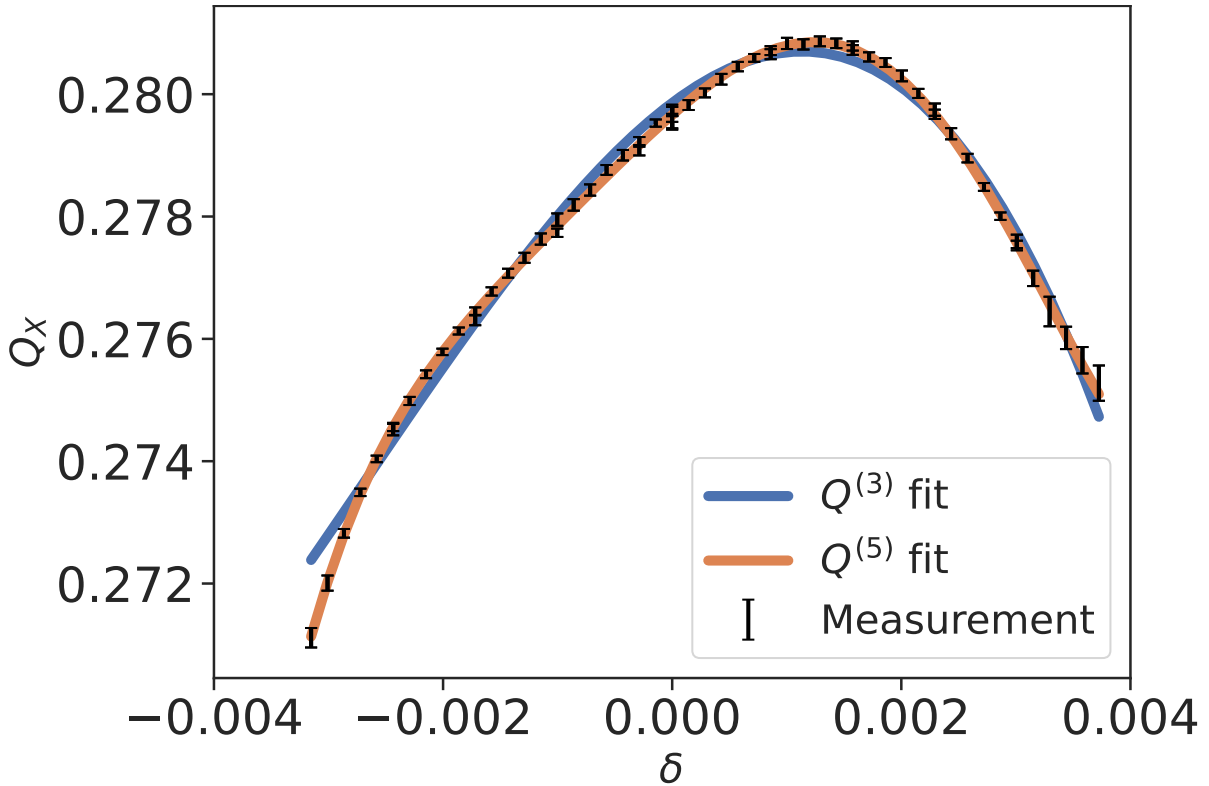
Figure 5.7 shows the chromaticity fit after the beam-based minimization of Q'' and Q''' , while Table 5.5 shows the measured chromaticity.

Previous studies of chromaticity in the LHC only considered fits up to third-order. Including fits

Beam	$K_4 [\text{m}^{-4}]$	$K_5 [\text{m}^{-5}]$
1	+3.2973	+1610
2	+2.1716	+1618

Table 5.4.: Corrections applied on top of the nominal octupole and decapole correctors strengths.

up to a fifth order increases the Q''' estimate of both measurements, while improving the fit quality. Q''' for beam 1 with only a fit to the third order would have a value of -0.38×10^6 instead of the -1.02×10^6 obtained with a fifth order fit. Accurately measuring the third order chromaticity is essential in order to correct it.

Figure 5.7.: Beam 1 measurement of high order chromaticity terms after application of Q'' and Q''' beam-based corrections on octupole and decapole correctors.

$Q^{(4)}$ and $Q^{(5)}$ fit quality

The values measured for $Q^{(4)}$ and $Q^{(5)}$ are similar across the two measurements, with nominal and beam-based corrections performed with very different lower order chromaticity and several hours

Plane	$Q^{(2)}[10^3]$	$Q^{(3)}[10^6]$	$Q^{(4)}[10^9]$	$Q^{(5)}[10^{12}]$
Beam 1				
X	-0.62 ± 0.01	-1.02 ± 0.03	-0.63 ± 0.02	1.22 ± 0.05
Y	-0.24 ± 0.01	0.12 ± 0.02	0.04 ± 0.02	-0.56 ± 0.04
Beam 2				
X	-0.85 ± 0.01	-0.64 ± 0.03	-0.58 ± 0.02	1.07 ± 0.06
Y	-0.30 ± 0.02	0.14 ± 0.03	0.16 ± 0.02	-0.66 ± 0.05

Table 5.5.: Terms of higher order chromaticity obtained during Run 3 commissioning in April 2022, with beam-based corrections for Q'' and Q''' .

apart. This reproducibility gives confidence that the measured values are robust. It is to be noted that one exception exists, for the horizontal plane of beam 2, where the measurement with nominal correction settings showed a high correlation between the fourth and fifth order terms, making the fit less reliable.

The reduced chi-square for the last measurement for each fit order is detailed in Tab. 5.6, where it can be seen that a fit above fifth order does not improve the fit quality.

Plane	$Q^{(3)}$	$Q^{(4)}$	χ_v^2	$Q^{(5)}$	$Q^{(6)}$
Beam 1					
X	17.9	12.1	1.8	1.5	
Y	3.0	2.2	0.7	0.7	
Beam 2					
X	17.3	7.1	1.8	1.8	
Y	2.9	2.8	1.0	1.0	

Table 5.6.: Reduced χ^2 values for each order of fit, taken from the last commissioning measurement.

5.2.3. NL-CHROMATICITY MODEL

The model of the LHC is based on MADX and WISE field errors [40]. To compute the chromaticity, simulations are run via the Polymorphic Tracking Code (PTC), with field errors from sextupole to decahexapole loaded and applied on all magnets. Simulation results are shown in Tab. 5.7.

Table 5.8 shows the ratio between measured and simulated high-order chromaticity. The measured $Q^{(5)}$ shows a consistent discrepancy with the model, larger by about a factor 2.

Simulations with only b_6 and b_7 field errors have been run to assess the contribution of lower order magnets to the fifth order chromaticities. The results strongly imply that the decatetrapole errors are

5.3. First Measurement of Dodecapole RDTs

Plane	$Q^{(4)} [10^9]$	$Q^{(5)} [10^{12}]$
Beam 1		
X	-0.2 ± 0.1	0.7 ± 0.1
Y	0.1 ± 0.1	-0.3 ± 0.1
Beam 2		
X	-0.2 ± 0.1	0.8 ± 0.1
Y	0.1 ± 0.1	-0.4 ± 0.1

Table 5.7.: Simulated high order chromaticity terms via PTC, including field errors from b_3 to b_8 with the previous beam-based corrections.

Plane	$Q^{(5)}$ ratio	
	First Meas.	Second Meas.
Beam 1		
X	1.8 ± 0.1	1.8 ± 0.1
Y	2.7 ± 0.3	1.7 ± 0.1
Beam 2		
X		1.6 ± 0.1
Y	2.2 ± 0.4	1.9 ± 0.2

Table 5.8.: Ratios of the measured to simulated fifth order chromaticity term for both first and second measurements. The values are taken from tables 5.3, 5.5 and 5.7. The fit with high correlation was not included.

the main contributors to $Q^{(5)}$, as can be seen in Fig. 5.8. Fringe fields and skew multipoles have been found to have a negligible impact. Ongoing studies are assessing the contribution of β -beating, linear coupling and alignment errors to those estimates.

5.3. First Measurement of Dodecapole RDTs

b6 meas from 2024 commissioning

5.4. CONCLUSIONS AND OUTLOOK

A wider momentum offset range, combined with new analysis techniques permitted the observation of fourth and fifth order chromaticity for the first time in the LHC. Reproducible values were measured with different machine configurations. Preliminary simulations show that the observed values do not

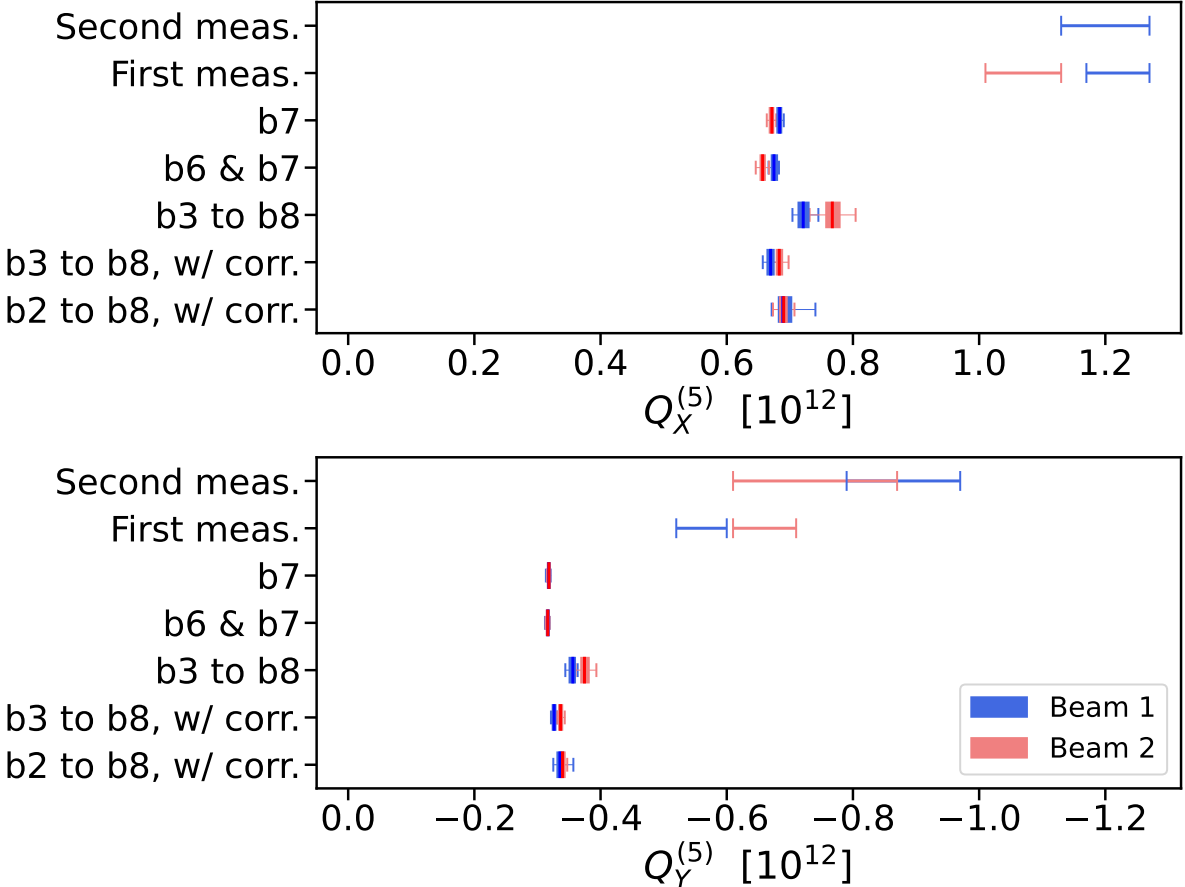


Figure 5.8.: Measured and simulated fifth order chromaticity. The simulations are done via PTC and include different multipole errors, some of them further include the nominal corrections for b_3 , b_4 and b_5 . The b_2 errors, applied on dipoles and quadrupoles, generate beta-beating. The measurement with a high correlation is not included.

match well with the LHC non-linear model. A factor 2 is observed between beams and planes for $Q^{(5)}$, which may point to a systematic error in the b_7 error model.

Correction of the measured higher order chromaticity terms is not possible, due to the lack of adequate correctors in the LHC. It is nevertheless interesting to characterize the higher order errors for an effective model and understand the effect a higher order fit has on lower order terms. Precise measurement of those lower chromaticity terms is required in order to effectively correct them. Higher order terms have thus to be taken into account.

The current range of momentum offset is deemed sufficient to measure higher order chromaticity. Attempts will, however, be taken to increase that range and assess if such a wider range can refine the estimate of $Q^{(4)}$ and $Q^{(5)}$.

Skew Octupolar Fields

6.1. Correction of skew octupole Fields at Top Energy

1. RDT Measurements
2. Orthogonality of correctors
3. Response Matrix
4. Correction
5. Comparison to 2018

6.2. Correction of Skew Octupole Fields at Injection Energy

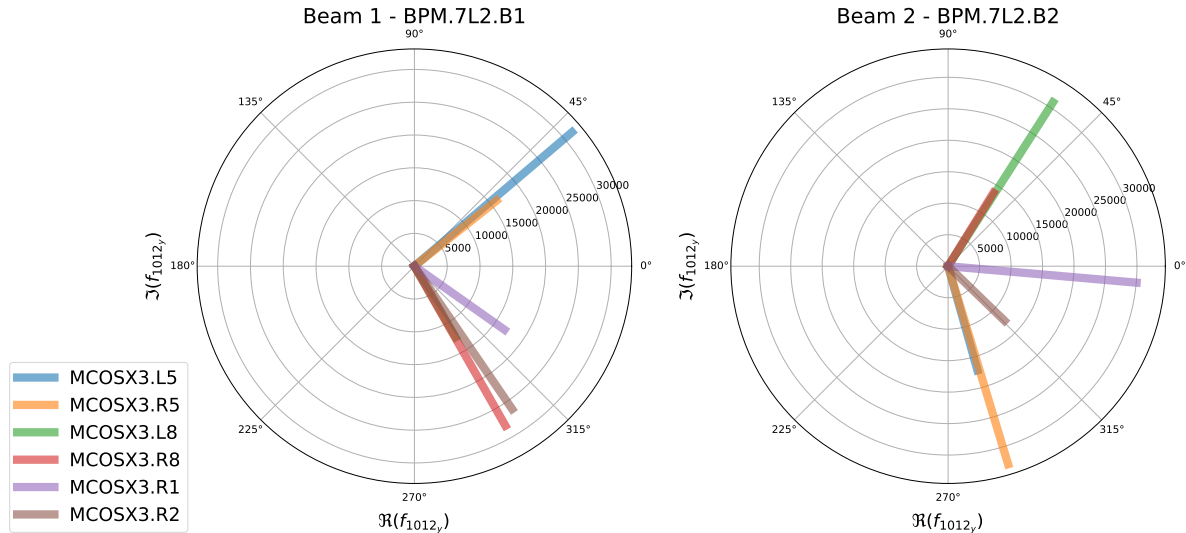


Figure 6.1.

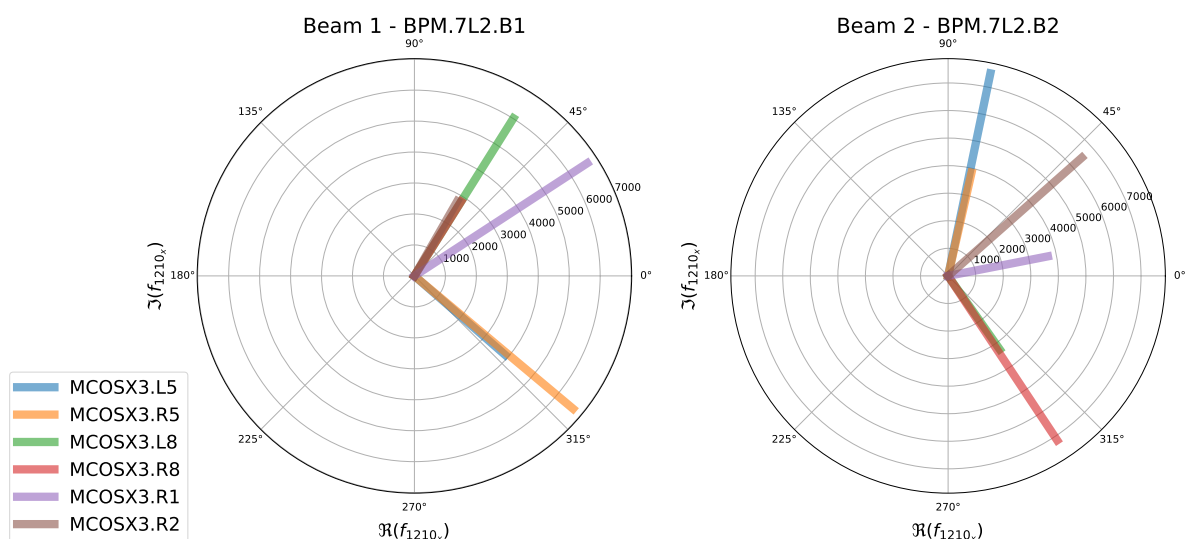


Figure 6.2.

6.3. Skew Octupolar Fields from Landau Octupoles

A

Hamiltonians and Transfer Maps

This appendix is intended to gather and explicit the Hamiltonians of the elements used in this thesis. Non-linear transfer maps are also described for some of those elements from the first to the second order.

A.1. Hamiltonians of Elements

The Hamiltonian of a *multipole* is the following [9–11]:

$$H = \Re \left[\sum_{n>1} (K_n + iJ_n) \frac{(x + iy)^n}{n!} \right]. \quad (\text{A.1})$$

From this, normal and skew fields can be separated:

$$\begin{aligned} N_n &= \frac{1}{n!} K_n \Re [(x + iy)^n] \\ S_n &= -\frac{1}{n!} J_n \Im [(x + iy)^n], \end{aligned} \quad (\text{A.2})$$

where K and J are the normalized strength of the multipole and x, y the transverse coordinates. Table A.1 explicits the normal and skew Hamiltonians of multipoles up to order 8.

A. Hamiltonians and Transfer Maps

Name	Order	Normal and Skew Hamiltonians
Drift	-	$H = \frac{1}{2}(p_x^2 + p_y^2)$
Quadrupole	2	$N_2 = \frac{1}{2!}K_2(x^2 - y^2)$ $S_2 = -J_2xy$
Sextupole	3	$N_3 = \frac{1}{3!}K_3(x^3 - 3xy^2)$ $S_3 = -\frac{1}{3!}J_3 \cdot (3x^2y - y^3)$
Octupole	4	$N_4 = \frac{1}{4!}K_4(x^4 - 6x^2y^2 + y^4)$ $S_4 = -\frac{1}{4!}J_4 \cdot (4x^3y - 4xy^3)$
Decapole	5	$N_5 = \frac{1}{5!}K_5(x^5 - 10x^3y^2 + 5xy^4)$ $S_5 = -\frac{1}{5!}J_5 \cdot (5x^4y - 10x^2y^3 + y^5)$
Dodecapole	6	$N_6 = \frac{1}{6!}K_6(x^6 - 15x^4y^2 + 15x^2y^4 - y^6)$ $S_6 = -\frac{1}{6!}J_6 \cdot (6x^5y - 20x^3y^3 + 6xy^5)$
Decatetrapole	7	$N_7 = \frac{1}{7!}K_7(x^7 - 21x^5y^2 + 35x^3y^4 - 7xy^6)$ $S_7 = -\frac{1}{7!}J_7 \cdot (7x^6y - 35x^4y^3 + 21x^2y^5 - y^7)$
Decahexapole	8	$N_8 = \frac{1}{8!}K_8(x^8 - 28x^6y^2 + 70x^4y^4 - 28x^2y^6 + y^8)$ $S_8 = -\frac{1}{8!}J_8 \cdot (8x^7y - 56x^5y^3 + 56x^3y^5 - 8xy^7)$

Table A.1.: Normal and skew Hamiltonians of multipoles up to order 8.

A

A.2. Transfer Maps

This section goes more in depth regarding the derivation of the examples of transfer maps introduced in Section 2.4.

As a reminder, the BCH of two elements up to order 3 is given below,

$$Z = \underbrace{H_2 + H_1}_{\text{First order}} + \underbrace{\frac{[H_2, H_1]}{2}}_{\text{Second order}} + \underbrace{\frac{[H_2, [H_2, H_1]]}{12} - \frac{[H_1, [H_2, H_1]]}{12}}_{\text{Third order}}. \quad (\text{A.3})$$

A.2.1. Generic Effective Hamiltonian of Two Elements

In order not to have to derive every combination of multipoles, a generic approach can be taken. Two elements of orders n and m can indeed be combined together via the BCH. Their hamiltonians is thus the one from Eq. (A.1) with orders m and n . A drift is put in between the two multipoles to change the coordinates. This results in non-zero Poisson brackets as the momentum is propagated,

$$[H_2, H_1] \rightarrow [H_2, D \cdot H_1]. \quad (\text{A.4})$$

Higher orders will arise with derivations when applying the Poisson brackets. Those orders can be found by counting the number of Poisson brackets, and which operators are implicated. A Poisson bracket implicating H_2 will increase the resulting order by m , and likewise for H_1 and n . The resulting order is then decreased by the number of poisson brackets times 2. Eq. (A.5) gives how this can be calculated when considering the written form of the Poisson brackets (eg. $[H_2, [H_2, H_1]]$).

A

$$\text{resulting order} = \text{count}("H_2") \cdot m + \text{count}("H_1") \cdot n - 2 \cdot \text{count}("[") \quad (\text{A.5})$$

Although this formula is quite helpful, it is not trivial to compute which orders will arise from each BCH order. Indeed, not all combinations of H_1 and H_2 appear, as explained in details in [17]. Table A.2 shows the Poisson brackets corresponding to each order of the BCH, up to order 6, along with the resulting multipole order. To keep the table readable, Poisson Brackets are not shown above that order, as duplicates of resulting orders become quite frequent. Similarly, Table A.3 shows how fields can be generated depending on the orders of multipoles and that of the BCH.

A. Hamiltonians and Transfer Maps

BCH Order	Poisson Brackets	Resulting Order
1	A	m
	B	n
2	$\frac{[A,B]}{2}$	$m+n-2$
3	$-\frac{[B,[A,B]]}{12}$ $\frac{[A,[A,B]]}{12}$	$m+2n-4$ $2m+n-4$
4	$-\frac{[B,[A,[A,B]]]}{24}$	$2m+2n-6$
5	$-\frac{[A,[B,[A,[A,B]]]]}{120}$ $-\frac{[B,[A,[A,[A,B]]]]}{180}$ $-\frac{[A,[B,[B,[A,B]]]]}{360}$ $-\frac{[A,[A,[A,[A,B]]]]}{720}$ $-\frac{[B,[B,[A,[A,B]]]]}{180}$ $-\frac{[B,[B,[B,[A,B]]]]}{720}$	$3m+2n-8$ $3m+2n-8$ $2m+3n-8$ $4m+n-8$ $2m+3n-8$ $m+4n-8$
6	$-\frac{[A,[A,[B,[A,[A,B]]]]]}{240}$ $-\frac{[A,[B,[B,[A,[A,B]]]]]}{240}$ $-\frac{[B,[B,[A,[A,[A,B]]]]]}{360}$ $-\frac{[A,[B,[B,[B,[A,B]]]]]}{720}$ $-\frac{[B,[A,[A,[A,[A,B]]]]]}{1440}$ $-\frac{[B,[B,[B,[A,[A,B]]]]]}{1440}$	$3m+3n-10$ $3m+3n-10$ $3m+3n-10$ $2m+4n-10$ $4m+2n-10$ $2m+4n-10$
7	\dots	$2m+5n-12$ $m+6n-12$ $3m+4n-12$ $5m+2n-12$ $6m+n-12$ $4m+3n-12$

Table A.2.: Resulting multipole orders arising from the Poisson brackets of a given BCH order for two multipoles A and B of order m and n . At order 7, the Poisson brackets are not given as duplicates grow the list significantly.

BCH Order						
Field	1	2	3	4	5	6
3	H_3					
4	H_4	$(H_3)^2$				
5	H_5	$H_3 H_4$	$(H_3)^3$			
6	H_6	$H_3 H_5,$ $(H_4)^2$	$(H_3)^2 H_4$	$(H_3)^4$		
7	H_7	$H_3 H_6,$ $H_4 H_5$	$(H_3)^2 H_5,$ $H_3 (H_4)^2$		$(H_3)^5$	
8	H_8	$H_3 H_7,$ $H_4 H_6$	$(H_3)^2 H_6,$ $(H_4)^3$	$(H_3)^2 (H_4)^2$	$(H_3)^4 H_4$	$(H_3)^6$
9	H_9	$H_4 H_7,$ $H_3 H_8,$ $H_5 H_6$	$(H_3)^2 H_7,$ $(H_4)^2 H_5,$ $H_3 (H_5)^2$		$(H_3)^3 (H_4)^2,$ $(H_3)^4 H_5$	
10	H_{10}	$H_4 H_8,$ $H_5 H_7,$ $H_3 H_9,$ $(H_6)^2$	$(H_3)^2 H_8,$ $H_4 (H_5)^2,$ $(H_4)^2 H_6$	$(H_4)^4,$ $(H_3)^2 (H_5)^2$	$(H_3)^2 (H_4)^3,$ $(H_3)^4 H_6$	$(H_3)^4 (H_4)^2$
11	H_{11}	$H_4 H_9,$ $H_3 H_{10},$ $H_6 H_7,$ $H_5 H_8$	$(H_4)^2 H_7,$ $H_3 (H_6)^2,$ $(H_5)^3,$ $(H_3)^2 H_9$		$(H_3)^4 H_7,$ $H_3 (H_4)^4,$ $(H_3)^3 (H_5)^2$	$(H_3)^3 (H_4)^3$
12	H_{12}	$H_6 H_8,$ $(H_7)^2,$ $H_5 H_9,$ $H_3 H_{11},$ $H_4 H_{10}$	$H_4 (H_6)^2,$ $(H_4)^2 H_8,$ $(H_5)^2 H_6,$ $(H_4)^2 (H_5)^2$	$(H_3)^2 (H_6)^2,$ $(H_4)^2 (H_5)^2$	$(H_3)^4 H_8,$ $(H_4)^5$	$(H_3)^4 (H_5)^2,$ $(H_3)^2 (H_4)^4$

A

Table A.3.: Correspondence of a combination of multipoles from a BCH order to multipole-like fields. The exponents indicate the order of the BCH for individual components.

A.2.2. Transfer Map of Two Sextupoles

The transfer map of two sextupoles H_1 and H_2 of strength K_1 and K_2 , separated by a drift to introduce a change of coordinates in H_1 is the following,

$$\mathcal{M} = e^{\cdot Z \cdot} = e^{\cdot H_2 \cdot} \cdot e^{D \cdot H_1 \cdot}, \quad (\text{A.6})$$

After such application of the drift on H_1 , the two hamiltonians read,

$$\begin{aligned} H_1 &= \frac{1}{3!} K_1 L_1 \left((L_D p_x + x)^3 - 3 (L_D p_x + x) (L_D p_y + y)^2 \right) \\ H_2 &= \frac{1}{3!} K_2 L_2 \left(x^3 - 3xy^2 \right). \end{aligned} \quad (\text{A.7})$$

Below are detailed each term of the BCH. Each term should be added together in order to obtain the whole effective Hamiltonian Z .

First Order

$$K_1 L_1 L_D \left(\begin{array}{l} \left(\frac{L_D^2 p_x^3}{6} - \frac{L_D^2 p_x p_y^2}{2} + \frac{L_D p_x^2 x}{2} - L_D p_x p_y y \right) \\ - \frac{L_D p_y^2 x}{2} + \frac{p_x x^2}{2} - \frac{p_x y^2}{2} - p_y x y \end{array} \right) \left. \begin{array}{l} \\ \\ \end{array} \right\} \text{sextupolar} \\ + K_1 L_1 \left(\frac{x^3}{6} - \frac{x y^2}{2} \right) + K_2 L_2 \left(\frac{x^3}{6} - \frac{x y^2}{2} \right) \end{math>$$

A

Second Order

$$K_1 K_2 L_1 L_2 L_D \left(\begin{array}{l} \left(\frac{L_D^2 p_x^2 x^2}{8} - \frac{L_D^2 p_x^2 y^2}{8} + \frac{L_D^2 p_x p_y x y}{2} - \frac{L_D^2 p_y^2 x^2}{8} \right) \\ + \frac{L_D^2 p_y^2 y^2}{8} + \frac{L_D p_x x^3}{4} + \frac{L_D p_x x y^2}{4} + \frac{L_D p_y x^2 y}{4} \\ + \frac{L_D p_y y^3}{4} + \frac{x^4}{8} + \frac{x^2 y^2}{4} + \frac{y^4}{8} \end{array} \right) \left. \begin{array}{l} \\ \\ \end{array} \right\} \text{octupolar-like}$$

Third Order

$$\begin{aligned}
& K_1^2 K_2 L_1^2 L_2 L_D \left(\begin{array}{l} \frac{L_D^5 p_x^4 x}{48} + \frac{L_D^5 p_x^3 p_y y}{12} - \frac{L_D^5 p_x^2 p_y^2 x}{8} - \frac{L_D^5 p_x p_y^3 y}{12} \\ + \frac{L_D^5 p_y^4 x}{48} + \frac{L_D^4 p_x^3 x^2}{12} + \frac{L_D^4 p_x^3 y^2}{12} - \frac{L_D^4 p_x p_y^2 x^2}{4} \\ - \frac{L_D^4 p_x p_y^2 y^2}{4} + \frac{L_D^3 p_x^2 x^3}{8} + \frac{L_D^3 p_x^2 x y^2}{8} - \frac{L_D^3 p_x p_y x^2 y}{4} \\ - \frac{L_D^3 p_x p_y y^3}{4} - \frac{L_D^3 p_y^2 x^3}{8} - \frac{L_D^3 p_y^2 x y^2}{8} + \frac{L_D^2 p_x x^4}{12} \\ - \frac{L_D^2 p_x y^4}{12} - \frac{L_D^2 p_y x^3 y}{6} - \frac{L_D^2 p_y x y^3}{6} + \frac{L_D x^5}{48} \\ - \frac{L_D x^3 y^2}{24} - \frac{L_D x y^4}{16} \end{array} \right) \\
& + K_1 K_2^2 L_1 L_2^2 L_D \left(\begin{array}{l} \frac{L_D^2 p_x x^4}{48} - \frac{L_D^2 p_x x^2 y^2}{8} + \frac{L_D^2 p_x y^4}{48} + \frac{L_D^2 p_y x^3 y}{12} \\ - \frac{L_D^2 p_y x y^3}{12} + \frac{L_D x^5}{48} - \frac{L_D x^3 y^2}{24} - \frac{L_D x y^4}{16} \end{array} \right)
\end{aligned} \quad \left. \right\} \text{decapolar-like} \quad (\text{A.10})$$

A.2.3. Transfer Map of a Sextupole and Octupole

The transfer map of a sextupole H_1 and octupole H_2 of strength K_1 and K_2 , separated by a drift like in the previous example is given by

$$\mathcal{M} = e^{:Z:} = e^{:H_2:} \cdot e^{D:H_1:} \quad (\text{A.11})$$

with H_1 and H_2 having as final expressions,

$$\begin{aligned}
H_1 &= \frac{1}{3!} K_{3,h1} L_1 \left((L_D p_x + x)^3 - 3 (L_D p_x + x) (L_D p_y + y)^2 \right) \\
H_2 &= \frac{1}{4!} K_2 L_2 \left(x^4 - 6x^2 y^2 + y^4 \right).
\end{aligned} \quad (\text{A.12})$$

The first two orders of the BCH of those two elements is given below.

First Order

$$\begin{aligned}
& K_3 \left(\begin{array}{l} \frac{L_D^3 p_x^3}{6} - \frac{L_D^3 p_x p_y^2}{2} + \frac{L_D^2 p_x^2 x}{2} - L_D^2 p_x p_y y - \frac{L_D^2 p_y^2 x}{2} \\ + \frac{L_D p_x x^2}{2} - \frac{L_D p_x y^2}{2} - L_D p_y x y + \frac{x^3}{6} - \frac{x y^2}{2} \end{array} \right) \left. \right\} \text{sextupolar} \\
& + K_4 \left(\frac{x^4}{24} - \frac{x^2 y^2}{4} + \frac{y^4}{24} \right) \left. \right\} \text{octupolar}
\end{aligned} \quad (\text{A.13})$$

Second Order

$$K_3 K_4 L_D \left(\begin{array}{l} \left(\frac{L_D^2 p_x^2 x^3}{24} - \frac{L_D^2 p_x^2 x y^2}{8} + \frac{L_D^2 p_x p_y x^2 y}{4} - \frac{L_D^2 p_x p_y y^3}{12} \right) \\ \left(-\frac{L_D^2 p_y^2 x^3}{24} + \frac{L_D^2 p_y^2 x y^2}{8} + \frac{L_D p_x x^4}{12} - \frac{L_D p_x y^4}{12} \right) \\ \left(+ \frac{L_D p_y x^3 y}{6} + \frac{L_D p_y x y^3}{6} + \frac{x^5}{24} + \frac{x^3 y^2}{12} + \frac{x y^4}{24} \right) \end{array} \right) \text{ decapolar-like} \quad (\text{A.14})$$

A.2.4. Transfer Map of a Skew Quadrupole and Octupole

The transfer map of a skew quadrupole H_1 and octupole H_2 of strength K_1 and K_2 , separated by a drift like in the previous examples is given by

$$\mathcal{M} = e^{:Z:} = e^{:H_2:} \cdot e^{D:H_1:} \quad (\text{A.15})$$

with H_1 and H_2 having as final expressions,

$$\begin{aligned} H_1 &= -J_1 L_1 (L_D p_x + x) (L_D p_y + y) \\ H_2 &= \frac{1}{4!} K_2 L_2 (x^4 - 6x^2 y^2 + y^4). \end{aligned} \quad (\text{A.16})$$

The first two orders of the BCH of those two elements is given below.

A
First Order

$$\begin{aligned} J_1 L_1 \left(-L_D^2 p_x p_y - L_D p_x y - L_D p_y x - x y \right) &\} \text{ skew quadrupolar} \\ + K_2 L_2 \left(\frac{x^4}{24} - \frac{x^2 y^2}{4} + \frac{y^4}{24} \right) &\} \text{ octupolar} \end{aligned} \quad (\text{A.17})$$

Second Order

$$J_1 K_2 L_1 L_2 L_D \left(\begin{array}{l} \left(\frac{L_D p_x x^2 y}{4} - \frac{L_D p_x y^3}{12} - \frac{L_D p_y x^3}{12} \right) \\ \left(+ \frac{L_D p_y x y^2}{4} + \frac{x^3 y}{6} + \frac{x y^3}{6} \right) \end{array} \right) \} \text{ skew octupolar-like} \quad (\text{A.18})$$

Chromatic Amplitude Detuning

This appendix details the derivations of chromatic amplitude detuning from sextupoles up to dodecapoles. *Chromatic Amplitude Detuning*, being detuning coming from both the action and the momentum offset, only starts appearing with decapoles. Below that order, only amplitude detuning and chromaticity can be observed. As those are part of the derivations, they will also be detailed here.

B.1. Expression

Up to the third order, the expression of the Taylor expansion of the Chromatic Amplitude Detuning around ϵ_x , ϵ_y and δ , for a tune Q_z , $z \in \{x, y\}$ reads:

$$\begin{aligned}
 Q_z(\epsilon_x, \epsilon_y, \delta) = Q_{z0} + & \left[\frac{\partial Q_z}{\partial \epsilon_x} \epsilon_x + \frac{\partial Q_z}{\partial \epsilon_y} \epsilon_y + \frac{\partial Q_z}{\partial \delta} \delta \right] \\
 & + \frac{1}{2!} \left[\frac{\partial^2 Q_z}{\partial \epsilon_x^2} \epsilon_x^2 + \frac{\partial^2 Q_z}{\partial \epsilon_y^2} \epsilon_y^2 + \frac{\partial^2 Q_z}{\partial \delta^2} \delta^2 \right. \\
 & \quad \left. + 2 \frac{\partial^2 Q_z}{\partial \epsilon_x \partial \epsilon_y} \epsilon_x \epsilon_y + 2 \frac{\partial^2 Q_z}{\partial \epsilon_x \partial \delta} \epsilon_x \delta + 2 \frac{\partial^2 Q_z}{\partial \delta \partial \epsilon_y} \delta \epsilon_y \right] \\
 & + \frac{1}{3!} \left[\frac{\partial^3 Q_z}{\partial \delta^3} \delta^3 + \frac{\partial^3 Q_z}{\partial \epsilon_x^3} \epsilon_x^3 + \frac{\partial^3 Q_z}{\partial \epsilon_y^3} \epsilon_y^3 \right. \\
 & \quad \left. + 3 \frac{\partial^3 Q_z}{\partial \epsilon_x \partial \delta^2} \delta^2 \epsilon_x + 3 \frac{\partial^3 Q_z}{\partial \epsilon_y \partial \delta^2} \delta^2 \epsilon_y + 3 \frac{\partial^3 Q_z}{\partial \epsilon_x^2 \partial \delta} \delta \epsilon_x^2 \right. \\
 & \quad \left. + 3 \frac{\partial^3 Q_z}{\partial \epsilon_y^2 \partial \delta} \delta \epsilon_y^2 + 3 \frac{\partial^3 Q_z}{\partial \epsilon_y \partial \epsilon_x^2} \epsilon_x^2 \epsilon_y + 3 \frac{\partial^3 Q_z}{\partial \epsilon_y^2 \partial \epsilon_x} \epsilon_x \epsilon_y^2 \right. \\
 & \quad \left. + 6 \frac{\partial^3 Q_z}{\partial \epsilon_y \partial \epsilon_x \partial \delta} \delta \epsilon_x \epsilon_y \right] + \dots
 \end{aligned} \tag{B.1}$$

B.2. Derivations

In this section, the terms of the chromatic amplitude detuning are given up to dodecapoles. Derivations are given only for sextupoles and octupoles, as the process remains fairly similar for higher orders. Vertical offsets will be neglected, as horizontal dispersion is dominant. The reasoning remains the same.

B

B.2.1. Principle

From [20], the detuning caused by a magnet of length L can be described by its hamiltonian with

$$\Delta Q_z = \frac{1}{2\pi} \int_L \frac{\partial \langle H \rangle}{\partial J_z} ds. \tag{B.2}$$

The usual variables x and y of Eq. (2.7) can be replaced by *action-angle* variables to introduce the action:

$$\begin{aligned}
 x & \rightarrow \sqrt{2J_x \beta_x} \cos \phi_x \\
 y & \rightarrow \sqrt{2J_y \beta_y} \cos \phi_x
 \end{aligned} \tag{B.3}$$

A momentum dependence can be introduced for a particle with a different orbit (Δz) [41] via dispersion. Combined with Eq. (B.3), a dependence on all required components is achieved:

$$\begin{aligned} x + \Delta x &\rightarrow \sqrt{2J_x\beta_x} \cos \phi_x + D_x \delta \\ y + \Delta y &\rightarrow \sqrt{2J_y\beta_y} \cos \phi_y + D_y \delta \end{aligned} \quad (\text{B.4})$$

After averaging over the phase variable, all that is left is to compute the partial derivatives.

B.2.2. Sextupole

Taken from Table A.1, the normal field of a sextupole is $N_3 = \frac{1}{3!}K_3(x^3 - 3xy^2)$. Introducing δ via an orbit offset and changing the variables to action-angle, as given in Eq. (B.4), leads to the following expression:

$$N_3 = \frac{1}{6}K_3 \left[-3 \left(\delta D_x + \sqrt{2J_x\beta_x} \cos \phi_x \right) \left(\sqrt{2J_y\beta_y} \cos \phi_y \right)^2 + \left(\delta D_x + \sqrt{2J_x\beta_x} \cos \phi_x \right)^3 \right] \quad (\text{B.5})$$

Averaging over the cosines means integrating over $[0, \pi]$ and dividing by π :

$$\begin{aligned} \langle N_3 \rangle &= \frac{1}{\pi} \int_0^\pi N_3 \\ &= \frac{1}{6\pi^2} K_3 \cdot \left(3\pi^2 J_x \beta_x \delta D_x - 3\pi^2 J_y \beta_y \delta D_x + \pi^2 \delta^3 D_x^3 \right) \end{aligned} \quad (\text{B.6})$$

Differentiating by either J_x or J_y gives the tune shift induced by a single sextupole:

$$\begin{aligned} \Delta Q_x &= \frac{1}{4\pi} K_3 \beta_x D_x \delta L \\ \Delta Q_y &= - \frac{1}{4\pi} K_3 \beta_y D_x \delta L \end{aligned} \quad (\text{B.7})$$

From now on, differentiating by the action would give amplitude detuning, and by δ the chromaticity. Cross-terms exist but evidently depend on the expression of the multipole. For a sextupole, differentiating by the action does not have an effect, as no action is present in the tune shift equation. Rather, sextupoles are known to contribute to the first order chromaticity Q' . The following gives a recap of those operations:

B. Chromatic Amplitude Detuning

$$\begin{aligned} \frac{\partial Q_x}{\partial J_x} &= 0 & ; \quad \frac{\partial Q_x}{\partial J_y} &= 0 & ; \quad \frac{\partial Q_x}{\partial \delta} &= \frac{1}{4\pi} K_3 \beta_x D_x L \\ \frac{\partial Q_y}{\partial J_x} &= 0 & ; \quad \frac{\partial Q_y}{\partial J_y} &= 0 & ; \quad \frac{\partial Q_y}{\partial \delta} &= -\frac{1}{4\pi} K_3 \beta_y D_x L \end{aligned} \quad (\text{B.8})$$

The overall contribution of sextupoles to the Chromatic Amplitude Detuning is then highlighted in the following:

$$Q_z(\epsilon_x, \epsilon_y, \delta) = Q_{z0} + \left[\frac{\partial Q_z}{\partial \epsilon_x} \epsilon_x + \frac{\partial Q_z}{\partial \epsilon_y} \epsilon_y + \frac{\partial Q_z}{\partial \delta} \delta \right] \quad (\text{B.9})$$

B.2.3. Octupole

With the normal hamiltonian of octupoles being $N_4 = \frac{1}{4!} K_4 (x^4 - 6x^2y^2 + y^4)$, applying an orbit offset and changing for action-angle variables gives the following:

B

$$\begin{aligned} N_4 = \frac{1}{24} K_4 & \left[\left(\sqrt{2J_x \beta_x} \cos \phi_x \right)^4 \right. \\ & + 4 \left(\sqrt{2J_x \beta_x} \cos \phi_x \right)^3 D_x \delta \\ & + 6 \left(\sqrt{2J_x \beta_x} \cos \phi_x \right)^2 D_x^2 \delta^2 \\ & + 4 \left(\sqrt{2J_x \beta_x} \cos \phi_x \right) D_x^2 \delta \\ & + D_x^4 \delta^4 \\ & - 6 \left(\sqrt{2J_x \beta_x} \cos \phi_x \right)^2 \left(\sqrt{2J_y \beta_y} \cos \phi_y \right)^2 \\ & - 6 \left(\sqrt{2J_y \beta_y} \cos \phi_y \right)^2 \cdot 2 \left(\sqrt{2J_x \beta_x} \cos \phi_x \right) D_x \delta \\ & - 6 \left(\sqrt{2J_y \beta_y} \cos \phi_y \right)^2 D_x^2 \delta^2 \\ & \left. + \left(\sqrt{2J_y \beta_y} \cos \phi_y \right)^4 \right] \quad (\text{B.10}) \end{aligned}$$

Average over the phase variables gives the following:

$$\begin{aligned}\langle N_4 \rangle &= \frac{1}{\pi} \int_0^\pi N_4 \\ &= \frac{1}{48} K_4 \left[3J_x^2 \beta_x^2 + 12J_x \beta_x D_x^2 \delta^2 + 2D_x^4 \delta^4 \right. \\ &\quad \left. - 12J_y \beta_y (J_x \beta_x + D_x^2 \delta^2) + 3J_y^2 \beta_y^2 \right]\end{aligned}\tag{B.11}$$

Differentiating by either J_x or J_y gives the tune shift induced by a single octupole. Contrary to sextupoles, it can be noted that some action terms $J_{x,y}$ remain in the expression.

$$\begin{aligned}\Delta Q_x &= \frac{1}{48\pi} K_4 L \left[3J_x \beta_x^2 + 6\beta_x D_x^2 \delta^2 - 6\beta_x J_y \beta_y \right] \\ \Delta Q_y &= \frac{1}{48\pi} K_4 L \left[-6J_x \beta_x \beta_y - 6\beta_y D_x^2 \delta^2 + 3J_y \beta_y^2 \right]\end{aligned}\tag{B.12}$$

Differentiating by the action $J_{x,y}$ yields amplitude detuning, while differentiating by the momentum offset yields the second order chromaticity Q'' :

$$\begin{aligned}\frac{\partial Q_x}{\partial J_x} &= \frac{1}{16\pi} K_4 \beta_x^2 L \quad ; \quad \frac{\partial Q_x}{\partial J_y} = -\frac{1}{8\pi} K_4 \beta_x \beta_y L \quad ; \quad \frac{\partial^2 Q_x}{\partial \delta^2} = \frac{1}{4\pi} K_4 \beta_x D_x^2 L \\ \frac{\partial Q_y}{\partial J_x} &= -\frac{1}{8\pi} K_4 \beta_x \beta_y L \quad ; \quad \frac{\partial Q_y}{\partial J_y} = \frac{1}{16\pi} K_4 \beta_y^2 L \quad ; \quad \frac{\partial^2 Q_y}{\partial \delta^2} = -\frac{1}{4\pi} K_4 \beta_y D_x^2 L\end{aligned}\tag{B.13}$$

The overall contribution of octupoles to the Chromatic Amplitude Detuning is then highlighted in the following:

$$\begin{aligned}Q_z(\epsilon_x, \epsilon_y, \delta) &= Q_{z0} + \left[\frac{\partial Q_z}{\partial \epsilon_x} \epsilon_x + \frac{\partial Q_z}{\partial \epsilon_y} \epsilon_y + \frac{\partial Q_z}{\partial \delta} \delta \right] \\ &\quad + \frac{1}{2!} \left[\frac{\partial^2 Q_z}{\partial \epsilon_x^2} \epsilon_x^2 + \frac{\partial^2 Q_z}{\partial \epsilon_y^2} \epsilon_y^2 + \frac{\partial^2 Q_z}{\partial \delta^2} \delta^2 \right. \\ &\quad \left. + 2 \frac{\partial^2 Q_z}{\partial \epsilon_x \partial \epsilon_y} \epsilon_x \epsilon_y + 2 \frac{\partial^2 Q_z}{\partial \epsilon_x \partial \delta} \epsilon_x \delta + 2 \frac{\partial^2 Q_z}{\partial \delta \partial \epsilon_y} \delta \epsilon_y \right]\end{aligned}\tag{B.14}$$

B.2.4. Decapole

Skipping the first steps detailed previously, the tune shift induced by a normal decapole is given by the following:

B. Chromatic Amplitude Detuning

$$\begin{aligned}\Delta Q_x &= \frac{1}{240\pi} K_5 L \left[10D_x^3 \delta^3 \beta_x + 15D_x \delta J_x \beta_x^2 - 30J_y \beta_y \beta_x D_x \delta \right] \\ \Delta Q_y &= \frac{1}{240\pi} K_5 L \left[-10D_x^3 \delta^3 \beta_y + 15D_x \delta J_y \beta_y^2 - 30J_x \beta_x \beta_y D_x \delta \right]\end{aligned}\quad (\text{B.15})$$

The terms of the chromatic amplitude detuning can now be computed. Unlike sextupoles and octupoles, cross-terms between δ and the action now appear, giving rise to *chromatic amplitude detuning* and the third order chromaticity Q''' :

$$\begin{aligned}\frac{\partial^2 Q_x}{\partial J_x \partial \delta} &= \frac{1}{16\pi} K_5 \beta_x^2 D_x L \quad ; \quad \frac{\partial^2 Q_x}{\partial J_y \partial \delta} = \frac{1}{8\pi} K_5 \beta_x \beta_y D_x L \quad ; \quad \frac{\partial^3 Q_x}{\partial \delta^3} = \frac{1}{4\pi} K_5 \beta_x D_x^3 L \\ \frac{\partial^2 Q_y}{\partial J_x \partial \delta} &= -\frac{1}{8\pi} K_5 \beta_x \beta_y D_x L \quad ; \quad \frac{\partial^2 Q_y}{\partial J_y \partial \delta} = \frac{1}{16\pi} K_5 \beta_y^2 D_x L \quad ; \quad \frac{\partial^3 Q_y}{\partial \delta^3} = -\frac{1}{4\pi} K_5 \beta_y D_x^3 L\end{aligned}\quad (\text{B.16})$$

The contribution of decapoles to Chromatic Amplitude Detuning is then the following:

$$\begin{aligned}Q_z(\epsilon_x, \epsilon_y, \delta) &= Q_{z0} + \left[\frac{\partial Q_z}{\partial \epsilon_x} \epsilon_x + \frac{\partial Q_z}{\partial \epsilon_y} \epsilon_y + \frac{\partial Q_z}{\partial \delta} \delta \right] \\ &\quad + \frac{1}{2!} \left[\frac{\partial^2 Q_z}{\partial \epsilon_x^2} \epsilon_x^2 + \frac{\partial^2 Q_z}{\partial \epsilon_y^2} \epsilon_y^2 + \frac{\partial^2 Q_z}{\partial \delta^2} \delta^2 \right. \\ &\quad \left. + 2 \frac{\partial^2 Q_z}{\partial \epsilon_x \partial \epsilon_y} \epsilon_x \epsilon_y + 2 \frac{\partial^2 Q_z}{\partial \epsilon_x \partial \delta} \epsilon_x \delta + 2 \frac{\partial^2 Q_z}{\partial \delta \partial \epsilon_y} \delta \epsilon_y \right] \\ &\quad + \frac{1}{3!} \left[\frac{\partial^3 Q_z}{\partial \delta^3} \delta^3 + \dots \right]\end{aligned}\quad (\text{B.17})$$

B

B.2.5. Dodecapole

The tune shift induced by a normal dodecapole is given by the following:

$$\begin{aligned}Q_x &= \frac{1}{720\pi} K_6 L \left[15J_x^2 \beta_x^3 + 30\beta_x D_x^4 \delta^4 + 90J_x \beta_x^2 D_x^2 \delta^2 \right. \\ &\quad \left. - 180J_y \beta_y \beta_x D_x^2 \delta^2 - 90J_y \beta_y J_x \beta_x^2 + 90J_y^2 \beta_y^2 \beta_x \right] \\ Q_y &= \frac{1}{720\pi} K_6 L \left[-30\beta_y D_x^4 \delta^4 - 180\beta_y J_x \beta_x D_x^2 \delta^2 - 90\beta_y J_x^2 \beta_x^2 \right. \\ &\quad \left. + 90J_y \beta_y^2 J_x \beta_x + 45J_y \beta_y^2 D_x^2 \delta^2 - 15J_y^2 \beta_y^3 \right]\end{aligned}\quad (\text{B.18})$$

The terms of the chromatic amplitude detuning can now be computed. Like for decapoles, chromatic amplitude detuning terms appear, as well as the third order chromaticity $Q^{(4)}$:

$$\begin{aligned}
 \frac{\partial^2 Q_x}{\partial J_x^2} &= \frac{1}{96\pi} K_6 \beta_x^3 L & \frac{\partial^2 Q_y}{\partial J_y^2} &= -\frac{1}{96\pi} K_6 \beta_y^3 L \\
 \frac{\partial^3 Q_x}{\partial J_x \partial \delta^2} &= \frac{1}{16\pi} K_6 \beta_x^2 D_x^2 L & \frac{\partial^3 Q_y}{\partial J_y \partial \delta^2} &= \frac{1}{16\pi} K_6 \beta_y^2 D_x^2 L \\
 \frac{\partial^2 Q_x}{\partial J_y^2} &= \frac{1}{32\pi} K_6 \beta_y^2 \beta_x L & \frac{\partial^2 Q_y}{\partial J_x^2} &= -\frac{1}{32\pi} K_6 \beta_y \beta_x^2 L \\
 \frac{\partial^3 Q_x}{\partial J_y \partial \delta^2} &= -\frac{1}{8\pi} K_6 \beta_y \beta_x D_x^2 L & \frac{\partial^3 Q_y}{\partial J_x \partial \delta^2} &= -\frac{1}{8\pi} K_6 \beta_y \beta_x D_x^2 L \\
 \frac{\partial^2 Q_x}{\partial J_x \partial J_y} &= -\frac{1}{32\pi} K_6 \beta_y \beta_x^2 L & \frac{\partial^2 Q_y}{\partial J_y \partial J_x} &= \frac{1}{32\pi} K_6 \beta_y^2 \beta_x L \\
 \frac{\partial^4 Q_x}{\partial \delta^4} &= \frac{1}{4\pi} K_6 \beta_x D_x^4 L & \frac{\partial^4 Q_y}{\partial \delta^4} &= -\frac{1}{4\pi} K_6 \beta_y D_x^4 L
 \end{aligned} \tag{B.19}$$

The contribution of dodecapoles to Chromatic Amplitude Detuning is then the following:

$$\begin{aligned}
 Q_z(\epsilon_x, \epsilon_y, \delta) = Q_{z0} + & \left[\frac{\partial Q_z}{\partial \epsilon_x} \epsilon_x + \frac{\partial Q_z}{\partial \epsilon_y} \epsilon_y + \frac{\partial Q_z}{\partial \delta} \delta \right] \\
 & + \frac{1}{2!} \left[\frac{\partial^2 Q_z}{\partial \epsilon_x^2} \epsilon_x^2 + \frac{\partial^2 Q_z}{\partial \epsilon_y^2} \epsilon_y^2 + 2 \frac{\partial^2 Q_z}{\partial \epsilon_x \partial \epsilon_y} \epsilon_x \epsilon_y + \dots \right] \\
 & + \frac{1}{3!} \left[3 \frac{\partial^3 Q_z}{\partial \epsilon_x \partial \delta^2} \delta^2 \epsilon_x + 3 \frac{\partial^3 Q_z}{\partial \epsilon_y \partial \delta^2} \delta^2 \epsilon_y + \dots \right] \\
 & + \frac{1}{4!} \left[\frac{\partial^4 Q_z}{\partial \delta^4} \delta^4 \right]
 \end{aligned} \tag{B.20}$$

B

B.3. PTC Validation

A simulation has been done with PTC to assess that those equations are correct. A dodecapole has been added to the lattice with a strength $KL = 1e6$. Here are the results, confirming PTC works as intended.

The ANH numbers refer to the partial derivative relative to J_x , J_y and δ . So ANHX 021 would for example be $\frac{\partial^3 Q_x}{\partial J_y^2 \partial \delta}$.

B. Chromatic Amplitude Detuning

Term	Analytical	Simulation	Rel. Diff [%]
ANH X 200	4782639.96971	4782639.97	0.0
ANH X 102	86945.930342	86945.93	-0.0
ANH X 020	593469879.552116	593469880.01	0.0
ANH X 012	-1118366.433407	-1118366.433	-0.0
ANH X 110	-92277073.535598	-92277073.6	0.0
ANH X 004	1053.754809	1053.7548	-0.000001
ANH Y 200	-92277073.535598	-92277073.6	0.0
ANH Y 102	-1118366.433407	-1118366.433	-0.0
ANH Y 020	-1272278817.264865	-1272278818.913	0.0
ANH Y 012	3596325.539479	3596325.543	0.0
ANH Y 110	593469879.552116	593469880.01	0.0
ANH Y 004	-6777.108503	-6777.1085	-0.0

C

Resonance Driving Terms

This appendix intends to clarify where Resonance Driving Terms can be seen in the frequency spectrum, what resonance they contribute to and what their action dependance is.

C.1. Expressions

The number of valid RDTs indeed grows rapidly with the magnet order n , as shows Table C.1, and is given by the following combinations:

$$C(n+3, 3) - C(n+1, 1) - [(n+1) \bmod 2] \cdot C\left(\left\lfloor \frac{n}{2} \right\rfloor + 1, 1\right). \quad (\text{C.1})$$

Multipole	Order	Number of poles	Number of RDTs
Quadrupole	2	4	5
Sextupole	3	6	16
Octupole	4	8	27
Decapole	5	10	50
Dodecapole	6	12	73
Decatetrapole	7	14	112
Decahexapole	8	16	151
Hectopole	50	100	23349
Kilopole	500	1000	2.1×10^7

Table C.1.: Number of valid RDTs for a given multipole order

Several different RDTs can contribute to the same line, which can be observed in the horizontal or

C

C. Resonance Driving Terms

vertical spectrum. The tables below describe which RDTs contribute to a specific combination of line and plane. All tables have been computed up to the order 6, for octopoles. The line columns represents (Q_x, Q_y) . For example $(-1, 2)$ is $-1Q_x + 2Qy$.

As a reminder, for a given RDT f_{jklm} , we will observe:

$$\begin{array}{ll} (j-k)Q_x + (l-m)Q_y = p \in \mathbb{N} & \text{excited resonance} \\ H(1-j+k, m-l) & \text{horizontal line, if } j \neq 0 \\ V(k-j, 1-l+m) & \text{vertical line, if } l \neq 0. \end{array} \quad (\text{C.2})$$

The amplitude of each line is given by:

$$\begin{aligned} |H_{f_{jklm}}| &= 2j(2I_x)^{\frac{j+k-1}{2}}(2I_y)^{\frac{l+m}{2}}|f_{jklm}| \\ |V_{f_{jklm}}| &= 2l(2I_x)^{\frac{j+k}{2}}(2I_y)^{\frac{l+m-1}{2}}|f_{jklm}|. \end{aligned} \quad (\text{C.3})$$

According to equations C.2 and C.3, it can be seen that many RDTs will not generate any line and thus can not be observed.

C.2. Frequency Spectrum Lines

The following Table C.2 shows which RDTs can be seen at a factor $Q_x \pm Q_y$ in the vertical or horizontal spectrums. This table is mostly useful when trying to identify which multipole or RDT contributes to a specific line that can appear during measurements.

Q_x	Q_y	H-jklm	V-jklm
-5	0	6000	5010
-4	-1	5010	4020
-4	0	5000	4010
-4	1	5001	4011
-3	-2	4020	3030
-3	-1	4010	3020
-3	0	4000, 4011, 5100	3010, 3021, 4110
-3	1	4001	3011
-3	2	4002	3012
-2	-3	3030	2040
-2	-2	3020	2030
-2	-1	3010, 3021, 4110	2020, 2031, 3120
-2	0	3000, 3011, 4100	2010, 2021, 3110
-2	1	3001, 3012, 4101	2011, 2022, 3111

Q_x	Q_y	H-jklm	V-jklm
-2	2	3002	2012
-2	3	3003	2013
-1	-4	2040	1050
-1	-3	2030	1040
-1	-2	2020, 2031, 3120	1030, 1041, 2130
-1	-1	2010, 2021, 3110	1020, 1031, 2120
-1	0	2000, 2011, 3100, 2022, 3111, 4200	1010, 1021, 2110, 1032, 2121, 3210
-1	1	2001, 2012, 3101	1011, 1022, 2111
-1	2	2002, 2013, 3102	1012, 1023, 2112
-1	3	2003	1013
-1	4	2004	1014
0	-5	1050	0060
0	-4	1040	0050
0	-3	1030, 1041, 2130	0040, 0051, 1140
0	-2	1020, 1031, 2120	0030, 0041, 1130
0	-1	1010, 1021, 2110, 1032, 2121, 3210	0020, 0031, 1120, 0042, 1131, 2220
0	0	1011, 2100, 1022, 2111, 3200	0021, 1110, 0032, 1121, 2210
0	1	1001, 1012, 2101, 1023, 2112, 3201	
0	2	1002, 1013, 2102	0012, 0023, 1112
0	3	1003, 1014, 2103	0013, 0024, 1113
0	4	1004	0014
0	5	1005	0015
1	-4	1140	0150
1	-3	1130	0140
1	-2	1120, 1131, 2220	0130, 0141, 1230
1	0		0110, 0121, 1210, 0132, 1221, 2310
1	-1	1110, 1121, 2210	0120, 0131, 1220
1	1	1101, 1112, 2201	0111, 0122, 1211
1	2	1102, 1113, 2202	0112, 0123, 1212
1	3	1103	0113
1	4	1104	0114
2	-3	1230	0240
2	-2	1220	0230
2	-1	1210, 1221, 2310	0220, 0231, 1320
2	0	1200, 1211, 2300	0210, 0221, 1310
2	1	1201, 1212, 2301	0211, 0222, 1311
2	2	1202	0212
2	3	1203	0213
3	-2	1320	0330
3	-1	1310	0320
3	0	1300, 1311, 2400	0310, 0321, 1410
3	1	1301	0311

C. Resonance Driving Terms

Q_x	Q_y	H-jklm	V-jklm
3	2	1302	0312
4	-1	1410	0420
4	0	1400	0410
4	1	1401	0411
5	0	1500	0510

Table C.2.: Correspondence of Resonance Driving Terms to the lines seen in the horizontal or vertical frequency spectrum.

C.3. Amplitude, Resonances and Lines

This part focuses on individual Resonance Drivings Terms, expliciting what magnet they originate from, what resonance they excite, how they can be observed and what kicks are needed in order to measure them. The amplitude columns implicitly omits the term $|f_{jklm}|$, which depends on K and J . The color coding helps quickly identifying dependences:

- I_x : depends only on horizontal amplitude
- I_y : depends only on vertical amplitude
- $I_x I_y$: depends on both horizontal and vertical amplitudes

n	jklm	Type	Resonance	H-line	V-line	Amplitude H	Amplitude V
2	0020	normal	(0, 2)		(0, -1)		$4(2I_y)^{1/2}$
2	2000	normal	(2, 0)	(-1, 0)		$4(2I_x)^{1/2}$	
2	0110	skew	(-1, 1)		(1, 0)		$2(2I_x)^{1/2}$
2	1001	skew	(1, -1)	(0, 1)		$2(2I_y)^{1/2}$	
2	1010	skew	(1, 1)	(0, -1)	(-1, 0)	$2(2I_y)^{1/2}$	$2(2I_x)^{1/2}$
3	0111	normal	(-1, 0)		(1, 1)		$2(2I_x)^{1/2}(2I_y)^{1/2}$
3	0120	normal	(-1, 2)		(1, -1)		$4(2I_x)^{1/2}(2I_y)^{1/2}$
3	1002	normal	(1, -2)	(0, 2)		$2(2I_y)$	
3	1011	normal	(1, 0)	(0, 0)	(-1, 1)	$2(2I_y)$	$2(2I_x)^{1/2}(2I_y)^{1/2}$
3	1020	normal	(1, 2)	(0, -2)	(-1, -1)	$2(2I_y)$	$4(2I_x)^{1/2}(2I_y)^{1/2}$
3	1200	normal	(-1, 0)	(2, 0)		$2(2I_x)$	
3	2100	normal	(1, 0)	(0, 0)		$4(2I_x)$	
3	3000	normal	(3, 0)	(-2, 0)		$6(2I_x)$	
3	0012	skew	(0, -1)		(0, 2)		$2(2I_y)$
3	0021	skew	(0, 1)		(0, 0)		$4(2I_y)$

n	jklm	Type	Resonance	H-line	V-line	Amplitude H	Amplitude V
3	0030	skew	(0, 3)		(0, -2)		$6(2I_y)$
3	0210	skew	(-2, 1)		(2, 0)		$2(2I_x)$
3	1101	skew	(0, -1)	(1, 1)		$2(2I_x)^{1/2}(2I_y)^{1/2}$	
3	1110	skew	(0, 1)	(1, -1)	(0, 0)	$2(2I_x)^{1/2}(2I_y)^{1/2}$	$2(2I_x)$
3	2001	skew	(2, -1)	(-1, 1)		$4(2I_x)^{1/2}(2I_y)^{1/2}$	
3	2010	skew	(2, 1)	(-1, -1)	(-2, 0)	$4(2I_x)^{1/2}(2I_y)^{1/2}$	$2(2I_x)$
4	0013	normal	(0, -2)		(0, 3)		$2(2I_y)^{3/2}$
4	0031	normal	(0, 2)		(0, -1)		$6(2I_y)^{3/2}$
4	0040	normal	(0, 4)		(0, -3)		$8(2I_y)^{3/2}$
4	0211	normal	(-2, 0)		(2, 1)		$2(2I_x)(2I_y)^{1/2}$
4	0220	normal	(-2, 2)		(2, -1)		$4(2I_x)(2I_y)^{1/2}$
4	1102	normal	(0, -2)	(1, 2)		$2(2I_x)^{1/2}(2I_y)$	
4	1120	normal	(0, 2)	(1, -2)	(0, -1)	$2(2I_x)^{1/2}(2I_y)$	$4(2I_x)(2I_y)^{1/2}$
4	1300	normal	(-2, 0)	(3, 0)		$2(2I_x)^{3/2}$	
4	2002	normal	(2, -2)	(-1, 2)		$4(2I_x)^{1/2}(2I_y)$	
4	2011	normal	(2, 0)	(-1, 0)	(-2, 1)	$4(2I_x)^{1/2}(2I_y)$	$2(2I_x)(2I_y)^{1/2}$
4	2020	normal	(2, 2)	(-1, -2)	(-2, -1)	$4(2I_x)^{1/2}(2I_y)$	$4(2I_x)(2I_y)^{1/2}$
4	3100	normal	(2, 0)	(-1, 0)		$6(2I_x)^{3/2}$	
4	4000	normal	(4, 0)	(-3, 0)		$8(2I_x)^{3/2}$	
4	0112	skew	(-1, -1)		(1, 2)		$2(2I_x)^{1/2}(2I_y)$
4	0121	skew	(-1, 1)		(1, 0)		$4(2I_x)^{1/2}(2I_y)$
4	0130	skew	(-1, 3)		(1, -2)		$6(2I_x)^{1/2}(2I_y)$
4	0310	skew	(-3, 1)		(3, 0)		$2(2I_x)^{3/2}$
4	1003	skew	(1, -3)	(0, 3)		$2(2I_y)^{3/2}$	
4	1012	skew	(1, -1)	(0, 1)	(-1, 2)	$2(2I_y)^{3/2}$	$2(2I_x)^{1/2}(2I_y)$
4	1021	skew	(1, 1)	(0, -1)	(-1, 0)	$2(2I_y)^{3/2}$	$4(2I_x)^{1/2}(2I_y)$
4	1030	skew	(1, 3)	(0, -3)	(-1, -2)	$2(2I_y)^{3/2}$	$6(2I_x)^{1/2}(2I_y)$
4	1201	skew	(-1, -1)	(2, 1)		$2(2I_x)(2I_y)^{1/2}$	
4	1210	skew	(-1, 1)	(2, -1)	(1, 0)	$2(2I_x)(2I_y)^{1/2}$	$2(2I_x)^{3/2}$
4	2101	skew	(1, -1)	(0, 1)		$4(2I_x)(2I_y)^{1/2}$	
4	2110	skew	(1, 1)	(0, -1)	(-1, 0)	$4(2I_x)(2I_y)^{1/2}$	$2(2I_x)^{3/2}$
4	3001	skew	(3, -1)	(-2, 1)		$6(2I_x)(2I_y)^{1/2}$	
4	3010	skew	(3, 1)	(-2, -1)	(-3, 0)	$6(2I_x)(2I_y)^{1/2}$	$2(2I_x)^{3/2}$
5	0113	normal	(-1, -2)		(1, 3)		$2(2I_x)^{1/2}(2I_y)^{3/2}$
5	0122	normal	(-1, 0)		(1, 1)		$4(2I_x)^{1/2}(2I_y)^{3/2}$

C

C. Resonance Driving Terms

n	jklm	Type	Resonance	H-line	V-line	Amplitude H	Amplitude V
5	0131	normal	(-1, 2)		(1, -1)		$6(2I_x)^{1/2}(2I_y)^{3/2}$
5	0140	normal	(-1, 4)		(1, -3)		$8(2I_x)^{1/2}(2I_y)^{3/2}$
5	0311	normal	(-3, 0)		(3, 1)		$2(2I_x)^{3/2}(2I_y)^{1/2}$
5	0320	normal	(-3, 2)		(3, -1)		$4(2I_x)^{3/2}(2I_y)^{1/2}$
5	1004	normal	(1, -4)	(0, 4)		$2(2I_y)^2$	
5	1013	normal	(1, -2)	(0, 2)	(-1, 3)	$2(2I_y)^2$	$2(2I_x)^{1/2}(2I_y)^{3/2}$
5	1022	normal	(1, 0)	(0, 0)	(-1, 1)	$2(2I_y)^2$	$4(2I_x)^{1/2}(2I_y)^{3/2}$
5	1031	normal	(1, 2)	(0, -2)	(-1, -1)	$2(2I_y)^2$	$6(2I_x)^{1/2}(2I_y)^{3/2}$
5	1040	normal	(1, 4)	(0, -4)	(-1, -3)	$2(2I_y)^2$	$8(2I_x)^{1/2}(2I_y)^{3/2}$
5	1202	normal	(-1, -2)	(2, 2)		$2(2I_x)(2I_y)$	
5	1211	normal	(-1, 0)	(2, 0)	(1, 1)	$2(2I_x)(2I_y)$	$2(2I_x)^{3/2}(2I_y)^{1/2}$
5	1220	normal	(-1, 2)	(2, -2)	(1, -1)	$2(2I_x)(2I_y)$	$4(2I_x)^{3/2}(2I_y)^{1/2}$
5	1400	normal	(-3, 0)	(4, 0)		$2(2I_x)^2$	
5	2102	normal	(1, -2)	(0, 2)		$4(2I_x)(2I_y)$	
5	2111	normal	(1, 0)	(0, 0)	(-1, 1)	$4(2I_x)(2I_y)$	$2(2I_x)^{3/2}(2I_y)^{1/2}$
5	2120	normal	(1, 2)	(0, -2)	(-1, -1)	$4(2I_x)(2I_y)$	$4(2I_x)^{3/2}(2I_y)^{1/2}$
5	2300	normal	(-1, 0)	(2, 0)		$4(2I_x)^2$	
5	3002	normal	(3, -2)	(-2, 2)		$6(2I_x)(2I_y)$	
5	3011	normal	(3, 0)	(-2, 0)	(-3, 1)	$6(2I_x)(2I_y)$	$2(2I_x)^{3/2}(2I_y)^{1/2}$
5	3020	normal	(3, 2)	(-2, -2)	(-3, -1)	$6(2I_x)(2I_y)$	$4(2I_x)^{3/2}(2I_y)^{1/2}$
5	3200	normal	(1, 0)	(0, 0)		$6(2I_x)^2$	
5	4100	normal	(3, 0)	(-2, 0)		$8(2I_x)^2$	
5	5000	normal	(5, 0)	(-4, 0)		$10(2I_x)^2$	
5	0014	skew	(0, -3)		(0, 4)		$2(2I_y)^2$
5	0023	skew	(0, -1)		(0, 2)		$4(2I_y)^2$
5	0032	skew	(0, 1)		(0, 0)		$6(2I_y)^2$
5	0041	skew	(0, 3)		(0, -2)		$8(2I_y)^2$
5	0050	skew	(0, 5)		(0, -4)		$10(2I_y)^2$
5	0212	skew	(-2, -1)		(2, 2)		$2(2I_x)(2I_y)$
5	0221	skew	(-2, 1)		(2, 0)		$4(2I_x)(2I_y)$
5	0230	skew	(-2, 3)		(2, -2)		$6(2I_x)(2I_y)$
5	0410	skew	(-4, 1)		(4, 0)		$2(2I_x)^2$
5	1103	skew	(0, -3)	(1, 3)		$2(2I_x)^{1/2}(2I_y)^{3/2}$	
5	1112	skew	(0, -1)	(1, 1)	(0, 2)	$2(2I_x)^{1/2}(2I_y)^{3/2}$	$2(2I_x)(2I_y)$
5	1121	skew	(0, 1)	(1, -1)	(0, 0)	$2(2I_x)^{1/2}(2I_y)^{3/2}$	$4(2I_x)(2I_y)$
5	1130	skew	(0, 3)	(1, -3)	(0, -2)	$2(2I_x)^{1/2}(2I_y)^{3/2}$	$6(2I_x)(2I_y)$

n	jklm	Type	Resonance	H-line	V-line	Amplitude H	Amplitude V
5	1301	skew	(-2, -1)	(3, 1)		$2(2I_x)^{3/2}(2I_y)^{1/2}$	
5	1310	skew	(-2, 1)	(3, -1)	(2, 0)	$2(2I_x)^{3/2}(2I_y)^{1/2}$	$2(2I_x)^2$
5	2003	skew	(2, -3)	(-1, 3)		$4(2I_x)^{1/2}(2I_y)^{3/2}$	
5	2012	skew	(2, -1)	(-1, 1)	(-2, 2)	$4(2I_x)^{1/2}(2I_y)^{3/2}$	$2(2I_x)(2I_y)$
5	2021	skew	(2, 1)	(-1, -1)	(-2, 0)	$4(2I_x)^{1/2}(2I_y)^{3/2}$	$4(2I_x)(2I_y)$
5	2030	skew	(2, 3)	(-1, -3)	(-2, -2)	$4(2I_x)^{1/2}(2I_y)^{3/2}$	$6(2I_x)(2I_y)$
5	2201	skew	(0, -1)	(1, 1)		$4(2I_x)^{3/2}(2I_y)^{1/2}$	
5	2210	skew	(0, 1)	(1, -1)	(0, 0)	$4(2I_x)^{3/2}(2I_y)^{1/2}$	$2(2I_x)^2$
5	3101	skew	(2, -1)	(-1, 1)		$6(2I_x)^{3/2}(2I_y)^{1/2}$	
5	3110	skew	(2, 1)	(-1, -1)	(-2, 0)	$6(2I_x)^{3/2}(2I_y)^{1/2}$	$2(2I_x)^2$
5	4001	skew	(4, -1)	(-3, 1)		$8(2I_x)^{3/2}(2I_y)^{1/2}$	
5	4010	skew	(4, 1)	(-3, -1)	(-4, 0)	$8(2I_x)^{3/2}(2I_y)^{1/2}$	$2(2I_x)^2$
6	0015	normal	(0, -4)		(0, 5)		$2(2I_y)^{5/2}$
6	0024	normal	(0, -2)		(0, 3)		$4(2I_y)^{5/2}$
6	0042	normal	(0, 2)		(0, -1)		$8(2I_y)^{5/2}$
6	0051	normal	(0, 4)		(0, -3)		$10(2I_y)^{5/2}$
6	0060	normal	(0, 6)		(0, -5)		$12(2I_y)^{5/2}$
6	0213	normal	(-2, -2)		(2, 3)		$2(2I_x)(2I_y)^{3/2}$
6	0222	normal	(-2, 0)		(2, 1)		$4(2I_x)(2I_y)^{3/2}$
6	0231	normal	(-2, 2)		(2, -1)		$6(2I_x)(2I_y)^{3/2}$
6	0240	normal	(-2, 4)		(2, -3)		$8(2I_x)(2I_y)^{3/2}$
6	0411	normal	(-4, 0)		(4, 1)		$2(2I_x)^2(2I_y)^{1/2}$
6	0420	normal	(-4, 2)		(4, -1)		$4(2I_x)^2(2I_y)^{1/2}$
6	1104	normal	(0, -4)	(1, 4)		$2(2I_x)^{1/2}(2I_y)^2$	
6	1113	normal	(0, -2)	(1, 2)	(0, 3)	$2(2I_x)^{1/2}(2I_y)^2$	$2(2I_x)(2I_y)^{3/2}$
6	1131	normal	(0, 2)	(1, -2)	(0, -1)	$2(2I_x)^{1/2}(2I_y)^2$	$6(2I_x)(2I_y)^{3/2}$
6	1140	normal	(0, 4)	(1, -4)	(0, -3)	$2(2I_x)^{1/2}(2I_y)^2$	$8(2I_x)(2I_y)^{3/2}$
6	1302	normal	(-2, -2)	(3, 2)		$2(2I_x)^{3/2}(2I_y)$	
6	1311	normal	(-2, 0)	(3, 0)	(2, 1)	$2(2I_x)^{3/2}(2I_y)$	$2(2I_x)^2(2I_y)^{1/2}$
6	1320	normal	(-2, 2)	(3, -2)	(2, -1)	$2(2I_x)^{3/2}(2I_y)$	$4(2I_x)^2(2I_y)^{1/2}$
6	1500	normal	(-4, 0)	(5, 0)		$2(2I_x)^{5/2}$	
6	2004	normal	(2, -4)	(-1, 4)		$4(2I_x)^{1/2}(2I_y)^2$	
6	2013	normal	(2, -2)	(-1, 2)	(-2, 3)	$4(2I_x)^{1/2}(2I_y)^2$	$2(2I_x)(2I_y)^{3/2}$
6	2022	normal	(2, 0)	(-1, 0)	(-2, 1)	$4(2I_x)^{1/2}(2I_y)^2$	$4(2I_x)(2I_y)^{3/2}$
6	2031	normal	(2, 2)	(-1, -2)	(-2, -1)	$4(2I_x)^{1/2}(2I_y)^2$	$6(2I_x)(2I_y)^{3/2}$

C

C. Resonance Driving Terms

n	jklm	Type	Resonance	H-line	V-line	Amplitude H	Amplitude V
6	2040	normal	(2, 4)	(-1, -4)	(-2, -3)	$4(2I_x)^{1/2}(2I_y)^2$	$8(2I_x)(2I_y)^{3/2}$
6	2202	normal	(0, -2)	(1, 2)		$4(2I_x)^{3/2}(2I_y)$	
6	2220	normal	(0, 2)	(1, -2)	(0, -1)	$4(2I_x)^{3/2}(2I_y)$	$4(2I_x)^2(2I_y)^{1/2}$
6	2400	normal	(-2, 0)	(3, 0)		$4(2I_x)^{5/2}$	
6	3102	normal	(2, -2)	(-1, 2)		$6(2I_x)^{3/2}(2I_y)$	
6	3111	normal	(2, 0)	(-1, 0)	(-2, 1)	$6(2I_x)^{3/2}(2I_y)$	$2(2I_x)^2(2I_y)^{1/2}$
6	3120	normal	(2, 2)	(-1, -2)	(-2, -1)	$6(2I_x)^{3/2}(2I_y)$	$4(2I_x)^2(2I_y)^{1/2}$
6	4002	normal	(4, -2)	(-3, 2)		$8(2I_x)^{3/2}(2I_y)$	
6	4011	normal	(4, 0)	(-3, 0)	(-4, 1)	$8(2I_x)^{3/2}(2I_y)$	$2(2I_x)^2(2I_y)^{1/2}$
6	4020	normal	(4, 2)	(-3, -2)	(-4, -1)	$8(2I_x)^{3/2}(2I_y)$	$4(2I_x)^2(2I_y)^{1/2}$
6	4200	normal	(2, 0)	(-1, 0)		$8(2I_x)^{5/2}$	
6	5100	normal	(4, 0)	(-3, 0)		$10(2I_x)^{5/2}$	
6	6000	normal	(6, 0)	(-5, 0)		$12(2I_x)^{5/2}$	
6	0114	skew	(-1, -3)		(1, 4)		$2(2I_x)^{1/2}(2I_y)^2$
6	0123	skew	(-1, -1)		(1, 2)		$4(2I_x)^{1/2}(2I_y)^2$
6	0132	skew	(-1, 1)		(1, 0)		$6(2I_x)^{1/2}(2I_y)^2$
6	0141	skew	(-1, 3)		(1, -2)		$8(2I_x)^{1/2}(2I_y)^2$
6	0150	skew	(-1, 5)		(1, -4)		$10(2I_x)^{1/2}(2I_y)^2$
6	0312	skew	(-3, -1)		(3, 2)		$2(2I_x)^{3/2}(2I_y)$
6	0321	skew	(-3, 1)		(3, 0)		$4(2I_x)^{3/2}(2I_y)$
6	0330	skew	(-3, 3)		(3, -2)		$6(2I_x)^{3/2}(2I_y)$
6	0510	skew	(-5, 1)		(5, 0)		$2(2I_x)^{5/2}$
6	1005	skew	(1, -5)	(0, 5)		$2(2I_y)^{5/2}$	
6	1014	skew	(1, -3)	(0, 3)	(-1, 4)	$2(2I_y)^{5/2}$	$2(2I_x)^{1/2}(2I_y)^2$
6	1023	skew	(1, -1)	(0, 1)	(-1, 2)	$2(2I_y)^{5/2}$	$4(2I_x)^{1/2}(2I_y)^2$
6	1032	skew	(1, 1)	(0, -1)	(-1, 0)	$2(2I_y)^{5/2}$	$6(2I_x)^{1/2}(2I_y)^2$
6	1041	skew	(1, 3)	(0, -3)	(-1, -2)	$2(2I_y)^{5/2}$	$8(2I_x)^{1/2}(2I_y)^2$
6	1050	skew	(1, 5)	(0, -5)	(-1, -4)	$2(2I_y)^{5/2}$	$10(2I_x)^{1/2}(2I_y)^2$
6	1203	skew	(-1, -3)	(2, 3)		$2(2I_x)(2I_y)^{3/2}$	
6	1212	skew	(-1, -1)	(2, 1)	(1, 2)	$2(2I_x)(2I_y)^{3/2}$	$2(2I_x)^{3/2}(2I_y)$
6	1221	skew	(-1, 1)	(2, -1)	(1, 0)	$2(2I_x)(2I_y)^{3/2}$	$4(2I_x)^{3/2}(2I_y)$
6	1230	skew	(-1, 3)	(2, -3)	(1, -2)	$2(2I_x)(2I_y)^{3/2}$	$6(2I_x)^{3/2}(2I_y)$
6	1401	skew	(-3, -1)	(4, 1)		$2(2I_x)^2(2I_y)^{1/2}$	
6	1410	skew	(-3, 1)	(4, -1)	(3, 0)	$2(2I_x)^2(2I_y)^{1/2}$	$2(2I_x)^{5/2}$
6	2103	skew	(1, -3)	(0, 3)		$4(2I_x)(2I_y)^{3/2}$	

C.3. Amplitude, Resonances and Lines

n	jklm	Type	Resonance	H-line	V-line	Amplitude H	Amplitude V
6	2112	skew	(1, -1)	(0, 1)	(-1, 2)	$4(2I_x)(2I_y)^{3/2}$	$2(2I_x)^{3/2}(2I_y)$
6	2121	skew	(1, 1)	(0, -1)	(-1, 0)	$4(2I_x)(2I_y)^{3/2}$	$4(2I_x)^{3/2}(2I_y)$
6	2130	skew	(1, 3)	(0, -3)	(-1, -2)	$4(2I_x)(2I_y)^{3/2}$	$6(2I_x)^{3/2}(2I_y)$
6	2301	skew	(-1, -1)	(2, 1)		$4(2I_x)^2(2I_y)^{1/2}$	
6	2310	skew	(-1, 1)	(2, -1)	(1, 0)	$4(2I_x)^2(2I_y)^{1/2}$	$2(2I_x)^{5/2}$
6	3003	skew	(3, -3)	(-2, 3)		$6(2I_x)(2I_y)^{3/2}$	
6	3012	skew	(3, -1)	(-2, 1)	(-3, 2)	$6(2I_x)(2I_y)^{3/2}$	$2(2I_x)^{3/2}(2I_y)$
6	3021	skew	(3, 1)	(-2, -1)	(-3, 0)	$6(2I_x)(2I_y)^{3/2}$	$4(2I_x)^{3/2}(2I_y)$
6	3030	skew	(3, 3)	(-2, -3)	(-3, -2)	$6(2I_x)(2I_y)^{3/2}$	$6(2I_x)^{3/2}(2I_y)$
6	3201	skew	(1, -1)	(0, 1)		$6(2I_x)^2(2I_y)^{1/2}$	
6	3210	skew	(1, 1)	(0, -1)	(-1, 0)	$6(2I_x)^2(2I_y)^{1/2}$	$2(2I_x)^{5/2}$
6	4101	skew	(3, -1)	(-2, 1)		$8(2I_x)^2(2I_y)^{1/2}$	
6	4110	skew	(3, 1)	(-2, -1)	(-3, 0)	$8(2I_x)^2(2I_y)^{1/2}$	$2(2I_x)^{5/2}$
6	5001	skew	(5, -1)	(-4, 1)		$10(2I_x)^2(2I_y)^{1/2}$	
6	5010	skew	(5, 1)	(-4, -1)	(-5, 0)	$10(2I_x)^2(2I_y)^{1/2}$	$2(2I_x)^{5/2}$

Table C.3.: Amplitude dependence, associated resonance and spectrum appearance of Resonance Driving Terms up to dodecapoles ($n = 6$).

Bibliography

- [1] *CERN Resources Website*. URL: <https://home.cern/resources>.
- [2] J Gareyte, J P Koutchouk, and F Ruggiero. *Landau Damping, Dynamic Aperture and Octupoles in LHC*. LHC Project Report 91. CERN, 1997. URL: <https://cds.cern.ch/record/321824>.
- [3] Oliver Sim Brüning et al. *LHC Design Report*. 2004. doi: [10.5170/CERN-2004-003-V-1](https://doi.org/10.5170/CERN-2004-003-V-1).
- [4] Félix Soubelet. “Local Interaction Region Coupling Correction for the LHC”. PhD thesis. 2023. URL: <https://cds.cern.ch/record/2891759>.
- [5] Laurent Deniau. *Magnetic model of Main Dipoles*. Technology Department. CERN, 2009.
- [6] *FiDeL - the magnetic model of the LHC*. 2021. URL: <https://lhc-div-mms.web.cern.ch/tests/MAG/Fidel/>.
- [7] Joschua Dilly. “Corrections of High-Order Nonlinear Errors in the LHC and HL-LHC Beam Optics”. To Be Submitted. Humboldt University of Berlin, 2022.
- [8] Rob Wolf. *Engineering Specification: Field Error Naming Conventions for LHC Magnets*. Tech. rep. LHC-M-ES-001.00. CERN, 2001. URL: <https://lhc-div-mms.web.cern.ch/lhc-div-mms/tests/MAG/FiDeL/Documentation/lhc-m-es-0001-30-00.pdf>.
- [9] Keintzel Jacqueline. “Beam Optics Design, Measurement and Correction Strategies for Circular Colliders at the Energy and Luminosity Frontier”. PhD thesis.
- [10] Rogelio Tomás. “Direct Measurement of Resonance Driving Terms in the Super Proton Synchrotron (SPS) of CERN Using Beam Position Monitors”. PhD Thesis. 2003. URL: <http://cds.cern.ch/record/615164>.
- [11] Andrea Franchi. “Studies and Measurements of Linear Coupling and Nonlinearities in Hadron Circular Accelerators”. Doctoral Thesis. Johann Wolfgang Goethe-Universität, 2006. URL: <https://publikationen.ub.uni-frankfurt.de/frontdoor/index/index/year/2006/docId/2270>.

Bibliography

- [12] E. D Courant and H. S Snyder. “Theory of the Alternating-Gradient Synchrotron”. In: *Annals of Physics* 3.1 (1958). doi: [10.1016/0003-4916\(58\)90012-5](https://doi.org/10.1016/0003-4916(58)90012-5). URL: <http://www.sciencedirect.com/science/article/pii/0003491658900125>.
- [13] S. Y. Lee. *Accelerator Physics*. Second. Hackensack, N.J: World Scientific, 2004.
- [14] A J Dragt. “An Overview of Lie Methods for Accelerator Physics”. In: *Proceedings of PAC*. Pasadena, CA USA: JACoW, 2013.
- [15] Ghislain J Roy. “Analysis of the optics of the Final Focus Test Beam using Lie algebra based techniques”. PhD thesis. 1992.
- [16] Etienne Forest. *Beam dynamics: a new attitude and framework*. The physics and technology of particle and photon beams 8. Amsterdam: Harwood Academic, 1998.
- [17] Fernando Casas and Ander Murua. “An efficient algorithm for computing the Baker-Campbell-Hausdorff series and some of its applications”. In: *Journal of Mathematical Physics* 50.3 (2009). doi: [10.1063/1.3078418](https://doi.org/10.1063/1.3078418). URL: <http://arxiv.org/abs/0810.2656>.
- [18] Félix Simon Carlier. “A Nonlinear Future: Measurements and Corrections of Nonlinear Beam Dynamics Using Forced Transverse Oscillations”. PhD Thesis. 2020. URL: <http://cds.cern.ch/record/2715765/>.
- [19] Werner Herr. *Mathematical and Numerical Methods for Non-linear Beam Dynamics*. Tech. rep. CERN Accelerator School, 2018. URL: <http://arxiv.org/abs/2006.09052>.
- [20] Joschua Dilly and Mael Le Garrec. *On the derivation of Amplitude Detuning and Chromaticity Formulas for Particle Accelerators*. 2023. URL: <http://arxiv.org/abs/2301.09132>.
- [21] Jacqueline Keintzel et al. “Second-Order Dispersion Measurement in LHC”. In: *IPAC’19*. Melbourne, Australia, 2019. doi: [10.18429/JACoW-IPAC2019-MOPMP027](https://doi.org/10.18429/JACoW-IPAC2019-MOPMP027).
- [22] R. Bartolini and F. Schmidt. “Normal Form via Tracking or Beam Data”. In: *Part. Accel.* 59.LHC-Project-Report-132 (1997).
- [23] M. Wendt. “BPM Systems: A Brief Introduction to Beam Position Monitoring”. In: *ArXiv200514081 Phys.* (2020). URL: <http://arxiv.org/abs/2005.14081>.
- [24] A. Nosych. *Geometrical Non-Linearity Correction Procedure Of LHC Beam Position Monitors*. 2014. URL: <https://edms.cern.ch/document/1342295/1>.
- [25] R. Miyamoto et al. “Parametrization of the driven betatron oscillation”. In: *Physical Review Special Topics - Accelerators and Beams* 11.8 (2008). doi: [10.1103/PhysRevSTAB.11.084002](https://doi.org/10.1103/PhysRevSTAB.11.084002). URL: <https://link.aps.org/doi/10.1103/PhysRevSTAB.11.084002>.
- [26] Javier Serrano and Matthieu Cattin. *The LHC AC Dipole system: an introduction*. 2010.
- [27] Ewen Hamish Maclean et al. *Commissioning of the nonlinear chromaticity at injection for LHC Run II*. Accelerators & Technology Sector Note 2016-0013. 2016. URL: <https://cds.cern.ch/record/2121333>.

- [28] N. Catalan-Lasheras, Stéphane David Fartoukh, and Jean-Pierre Koutchouk. *Linear Optics Measurements Using an AC-Dipole Excitation*. Tech. rep. 2004. URL: <http://cds.cern.ch/record/712136>.
- [29] M. Le Garrec. *Non-linear Chromaticity GUI*. 2022. URL: <https://gitlab.cern.ch/mlegarre/nl-chroma-gui>.
- [30] E H Maclean et al. “Non-linear Chromaticity Studies of the LHC at Injection”. In: *Proc. IPAC’11*. San Sebastian, Spain, Sep. 2011: JACoW Publishing, Geneva, Switzerland, 2011. URL: <https://jacow.org/IPAC2011/papers/WEPC078.pdf>.
- [31] Ewen Hamish Maclean, Felix Simon Carlier, and Jaime Coello de Portugal. “Commissioning of Non-linear Optics in the LHC at Injection Energy”. In: *Proc. IPAC*. Busan, Korea, 2016. doi: [10.18429/JACoW-IPAC2016-THPMR039](https://doi.org/10.18429/JACoW-IPAC2016-THPMR039). URL: <https://cds.cern.ch/record/2207446>.
- [32] Ewen Hamish Maclean et al. “Measurement of Nonlinear Observables in the Large Hadron Collider Using Kicked Beams”. In: *Phys. Rev. ST Accel. Beams* 17.8 (2014). doi: [10.1103/PhysRevSTAB.17.081002](https://doi.org/10.1103/PhysRevSTAB.17.081002). URL: <https://link.aps.org/doi/10.1103/PhysRevSTAB.17.081002>.
- [33] W. Venturini Delsolaro and R Wolf. *Magnetic Behavior of LHC Superconducting Correctors: Issues for Machine Operation*. Tech. rep. 2005. URL: <https://cds.cern.ch/record/987834/>.
- [34] *Ten out of ten for LHC decapole magnets*. Tech. rep. BUL-NA-2001-041. 2001. URL: <https://cds.cern.ch/record/45154>.
- [35] Yannis Papaphilippou. “Detecting chaos in particle accelerators through the frequency map analysis method”. In: () .
- [36] F??lix Simon Carlier. “A nonlinear future: measurements and corrections of nonlinear beam dynamics using forced transverse oscillations”. PhD thesis. 2020.
- [37] Riccardo de Maria. “LHC Interaction region upgrade”. PhD thesis. 2008. URL: <https://cds.cern.ch/record/1127611>.
- [38] Ewen H. Maclean et al. “Prospects for beam-based study of dodecapole nonlinearities in the CERN High-Luminosity Large Hadron Collider”. In: *The European Physical Journal Plus* 137.11 (2022). doi: [10.1140/epjp/s13360-022-03367-2](https://doi.org/10.1140/epjp/s13360-022-03367-2). URL: <https://link.springer.com/10.1140/epjp/s13360-022-03367-2>.
- [39] A. Franchi et al. “First Simultaneous Measurement of Sextupolar and Octupolar Resonance Driving Terms in a Circular Accelerator from Turn-by-Turn Beam Position Monitors Data”. In: *Phys. Rev. Spec. Top. - Accel. Beams* 17.7 (2014). doi: [10.1103/PhysRevSTAB.17.074001](https://doi.org/10.1103/PhysRevSTAB.17.074001).
- [40] P. Hagen et al. *Wise: An adaptive simulation of the LHC optics*. Tech. rep. 2006. URL: <https://cds.cern.ch/record/977794/files/lhc-project-report-971.pdf>.
- [41] Helmut Wiedemann. *Particle accelerator physics*. 2nd ed. Berlin ; New York: Springer, 1999.

Bibliography

- [42] Joschua Dilly et al. “First operational dodecapole correction in the LHC”. In: *Physical Review Accelerators and Beams* 26.12 (2023). doi: [10.1103/PhysRevAccelBeams.26.121001](https://doi.org/10.1103/PhysRevAccelBeams.26.121001). URL: <https://link.aps.org/doi/10.1103/PhysRevAccelBeams.26.121001>.
- [43] Mael Le Garrec et al. “Measurement and modelling of decapole errors in the LHC from beam-based studies”. In: *IPAC’23*. Venice, Italy, 2023. doi: [10.18429/JACOW-IPAC2023-MOPL024](https://doi.org/10.18429/JACOW-IPAC2023-MOPL024). URL: <https://jacow.org/ipac2023/doi/jacow-ipac2023-mopl024>.
- [44] Mael Le Garrec et al. “First measurement of fourth and fifth order chromaticity in the LHC”. In: *IPAC’23*. Venice, Italy, 2023. doi: [10.18429/JACOW-IPAC2023-MOPL027](https://doi.org/10.18429/JACOW-IPAC2023-MOPL027). URL: <https://jacow.org/ipac2023/doi/jacow-ipac2023-mopl027>.
- [45] Tobias Persson et al. “LHC Optics Commissioning in 2023 and 2024”. In: *IPAC’24*. Nashville, Tennessee, USA, 2024.
- [46] Vittorio Ferrentino et al. “LHC 2023 Ion Optics Commissioning”. In: *IPAC’24*. Nashville, Tennessee, USA, 2024.
- [47] Sasha J. Horney et al. “Sextupole RDTs in The LHC at Injection and in the Ramp”. In: *IPAC’24*. Nashville, Tennessee, USA, 2024.
- [48] Tuuli Nissinen et al. “LHC Optics Measurements from Transverse Damper for the High Intensity Frontier”. In: 2023. doi: [10.18429/JACOW-HB2023-THBP14](https://doi.org/10.18429/JACOW-HB2023-THBP14). URL: <https://jacow.org/hb2023/doi/JACoW-HB2023-THBP14.html>.
- [49] Rogelio Tomás García et al. “Optics for Landau Damping with Minimized Octupolar Resonances in the LHC”. In: 2023. doi: [10.18429/JACOW-HB2023-THBP20](https://doi.org/10.18429/JACOW-HB2023-THBP20). URL: <https://jacow.org/hb2023/doi/JACoW-HB2023-THBP20.html>.
- [50] Jacqueline Keintzel et al. “60° phase advance optics measurements in the Large Hadron Collider at CERN”. In: *IPAC’23*. Venice, Italy, 2023. doi: [10.18429/JACOW-IPAC2023-MOPL026](https://doi.org/10.18429/JACOW-IPAC2023-MOPL026). URL: <https://jacow.org/ipac2023/doi/jacow-ipac2023-mopl026>.
- [51] Felix Carlier et al. “Challenges of K-modulation measurements in the LHC Run 3”. In: *IPAC’23*. Venice, Italy, 2023. doi: [10.18429/JACOW-IPAC2023-MOPL014](https://doi.org/10.18429/JACOW-IPAC2023-MOPL014). URL: <https://jacow.org/ipac2023/doi/jacow-ipac2023-mopl014>.
- [52] Felix Carlier et al. “LHC Run 3 optics corrections”. In: *IPAC’23*. Venice, Italy, 2023. doi: [10.18429/JACOW-IPAC2023-MOPL015](https://doi.org/10.18429/JACOW-IPAC2023-MOPL015). URL: <https://jacow.org/ipac2023/doi/jacow-ipac2023-mopl015>.
- [53] Elena Fol et al. “Experimental Demonstration of Machine Learning Application in LHC Optics Commissioning”. In: *Proc. 13th Int. Part. Accel. Conf. IPAC22*. Vol. IPAC2022. Bangkok, Thailand: JACoW, 2022. doi: [10.18429/JACOW-IPAC2022-MOPOPT047](https://doi.org/10.18429/JACOW-IPAC2022-MOPOPT047).
- [54] Tobias Persson et al. “Optics Correction Strategy for Run 3 of the LHC”. In: *Proc. 13th Int. Part. Accel. Conf. IPAC22*. Vol. IPAC2022. Bangkok, Thailand: JACoW, 2022. doi: [10.18429/JACOW-IPAC2022-WEPOST008](https://doi.org/10.18429/JACOW-IPAC2022-WEPOST008).

- [55] Tobias Persson et al. “Optics Measurements and Correction Plans for the HL-LHC”. In: *IPAC’21*. Campinas, Brazil: JACOW Publishing, Geneva, Switzerland, 2021. doi: [10.18429/JACoW-IPAC2021-WEPAB026](https://doi.org/10.18429/JACoW-IPAC2021-WEPAB026). URL: <https://accelconf.web.cern.ch/ipac2021/doi/JACoW-IPAC2021-WEPAB026.html>.
- [56] Tobias Persson et al. “Optics Correction Strategy for Run 3 of the LHC”. In: *IPAC’21*. Campinas, Brazil: JACOW Publishing, Geneva, Switzerland, 2021. doi: [10.18429/JACoW-IPAC2021-WEPAB027](https://doi.org/10.18429/JACoW-IPAC2021-WEPAB027). URL: <https://accelconf.web.cern.ch/ipac2021/doi/JACoW-IPAC2021-WEPAB027.html>.
- [57] Ewen Maclean et al. “Optics Measurement by Excitation of Betatron Oscillations in the CERN PSB”. In: *IPAC’21*. Campinas, Brazil: JACOW Publishing, Geneva, Switzerland, 2021. doi: [10.18429/JACoW-IPAC2021-THPAB168](https://doi.org/10.18429/JACoW-IPAC2021-THPAB168).
- [58] Maël Le Garrec et al. *MD6864 – Decapole studies at injection*. Accelerators & Technology Sector Note CERN-ACC-NOTE-2023-0018. CERN, 2023. URL: <https://cds.cern.ch/record/2879070>.
- [59] Xavier Buffat et al. *Optics Measurement and Correction Strategies for HL-LHC*. Accelerators & Technology Sector Note CERN-ACC-2022-0004. CERN, 2022. URL: <https://cds.cern.ch/record/2808650>.
- [60] O. Aberle et al. *High-Luminosity Large Hadron Collider (HL-LHC): Technical Design Report*. CERN Yellow Reports: Monographs CERN-2020-010. Geneva: CERN, 2020. doi: [10.23731/CYRM-2020-0010](https://doi.org/10.23731/CYRM-2020-0010). URL: <https://cds.cern.ch/record/2749422>.
- [61] Maël Le Garrec. *Correction of Decapolar Resonances in the LHC*. Goethe Universität, Frankfurt, 2023.

List of Publications

Journal Publications

None yet.

Journal Publications (co-author)

- (1) Ewen H. Maclean et al. “Prospects for beam-based study of dodecapole nonlinearities in the CERN High-Luminosity Large Hadron Collider”. In: *The European Physical Journal Plus* 137.11 (2022). doi: [10.1140/epjp/s13360-022-03367-2](https://doi.org/10.1140/epjp/s13360-022-03367-2). URL: <https://link.springer.com/10.1140/epjp/s13360-022-03367-2>
- (2) Joschua Dilly et al. “First operational dodecapole correction in the LHC”. in: *Physical Review Accelerators and Beams* 26.12 (2023). doi: [10.1103/PhysRevAccelBeams.26.121001](https://doi.org/10.1103/PhysRevAccelBeams.26.121001). URL: <https://link.aps.org/doi/10.1103/PhysRevAccelBeams.26.121001>

Conference Proceedings

- (1) Mael Le Garrec et al. “Measurement and modelling of decapole errors in the LHC from beam-based studies”. In: *IPAC’23*. Venice, Italy, 2023. doi: [10.18429/JACOW-IPAC2023-MOPL024](https://doi.org/10.18429/JACOW-IPAC2023-MOPL024). URL: <https://jacow.org/ipac2023/doi/jacow-ipac2023-mopl024>
- (2) Mael Le Garrec et al. “First measurement of fourth and fifth order chromaticity in the LHC”. in: *IPAC’23*. Venice, Italy, 2023. doi: [10.18429/JACOW-IPAC2023-MOPL027](https://doi.org/10.18429/JACOW-IPAC2023-MOPL027). URL: <https://jacow.org/ipac2023/doi/jacow-ipac2023-mopl027>

Conference Proceedings (co-author)

- (1) Tobias Persson et al. "LHC Optics Commissioning in 2023 and 2024". In: *IPAC'24*. Nashville, Tennessee, USA, 2024
- (2) Vittorio Ferrentino et al. "LHC 2023 Ion Optics Commissioning". In: *IPAC'24*. Nashville, Tennessee, USA, 2024
- (3) Sasha J. Horney et al. "Sextupole RDTs in The LHC at Injection and in the Ramp". In: *IPAC'24*. Nashville, Tennessee, USA, 2024
- (4) Tuuli Nissinen et al. "LHC Optics Measurements from Transverse Damper for the High Intensity Frontier". In: 2023. doi: [10.18429/JACOW-HB2023-THBP14](https://doi.org/10.18429/JACOW-HB2023-THBP14). URL: <https://jacow.org/hb2023/doi/JACoW-HB2023-THBP14.html>
- (5) Rogelio Tomás García et al. "Optics for Landau Damping with Minimized Octupolar Resonances in the LHC". in: 2023. doi: [10.18429/JACOW-HB2023-THBP20](https://doi.org/10.18429/JACOW-HB2023-THBP20). URL: <https://jacow.org/hb2023/doi/JACoW-HB2023-THBP20.html>
- (6) Jacqueline Keintzel et al. "60° phase advance optics measurements in the Large Hadron Collider at CERN". in: *IPAC'23*. Venice, Italy, 2023. doi: [10.18429/JACOW-IPAC2023-MOPL026](https://doi.org/10.18429/JACOW-IPAC2023-MOPL026). URL: <https://jacow.org/ipac2023/doi/jacow-ipac2023-mopl026>
- (7) Felix Carlier et al. "Challenges of K-modulation measurements in the LHC Run 3". In: *IPAC'23*. Venice, Italy, 2023. doi: [10.18429/JACOW-IPAC2023-MOPL014](https://doi.org/10.18429/JACOW-IPAC2023-MOPL014). URL: <https://jacow.org/ipac2023/doi/jacow-ipac2023-mopl014>
- (8) Felix Carlier et al. "LHC Run 3 optics corrections". In: *IPAC'23*. Venice, Italy, 2023. doi: [10.18429/JACOW-IPAC2023-MOPL015](https://doi.org/10.18429/JACOW-IPAC2023-MOPL015). URL: <https://jacow.org/ipac2023/doi/jacow-ipac2023-mopl015>
- (9) Elena Fol et al. "Experimental Demonstration of Machine Learning Application in LHC Optics Commissioning". In: *Proc. 13th Int. Part. Accel. Conf. IPAC22*. Vol. IPAC2022. Bangkok, Thailand: JACoW, 2022. doi: [10.18429/JACOW-IPAC2022-MOP0T047](https://doi.org/10.18429/JACOW-IPAC2022-MOP0T047)
- (10) Tobias Persson et al. "Optics Correction Strategy for Run 3 of the LHC". in: *Proc. 13th Int. Part. Accel. Conf. IPAC22*. Vol. IPAC2022. Bangkok, Thailand: JACoW, 2022. doi: [10.18429/JACOW-IPAC2022-WEPOST008](https://doi.org/10.18429/JACOW-IPAC2022-WEPOST008)
- (11) Tobias Persson et al. "Optics Measurements and Correction Plans for the HL-LHC". in: *IPAC'21*. Campinas, Brazil: JACoW Publishing, Geneva, Switzerland, 2021. doi: [10.18429/JACOW-IPAC2021-WEPAB026](https://doi.org/10.18429/JACOW-IPAC2021-WEPAB026). URL: <https://accelconf.web.cern.ch/ipac2021/doi/JACoW-IPAC2021-WEPAB026.html>
- (12) Tobias Persson et al. "Optics Correction Strategy for Run 3 of the LHC". in: *IPAC'21*. Campinas, Brazil: JACoW Publishing, Geneva, Switzerland, 2021. doi: [10.18429/JACOW-IPAC2021-WEPOST008](https://doi.org/10.18429/JACOW-IPAC2021-WEPOST008)

[IPAC2021-WEPAB027](https://accelconf.web.cern.ch/ipac2021/doi/JACoW-IPAC2021-WEPAB027.html). URL: <https://accelconf.web.cern.ch/ipac2021/doi/JACoW-IPAC2021-WEPAB027.html>

- (13) Ewen Maclean et al. “Optics Measurement by Excitation of Betatron Oscillations in the CERN PSB”. in: *IPAC’21*. Campinas, Brazil: JACOW Publishing, Geneva, Switzerland, 2021. doi: [10.18429/JACoW-IPAC2021-THPAB168](https://doi.org/10.18429/JACoW-IPAC2021-THPAB168)

Notes and Reports

- (1) Maël Le Garrec et al. *MD6864 – Decapole studies at injection*. Accelerators & Technology Sector Note CERN-ACC-NOTE-2023-0018. CERN, 2023. URL: <https://cds.cern.ch/record/2879070>
- (2) Joschua Dilly and Mael Le Garrec. *On the derivation of Amplitude Detuning and Chromaticity Formulas for Particle Accelerators*. 2023. URL: <http://arxiv.org/abs/2301.09132>
- (3) Xavier Buffat et al. *Optics Measurement and Correction Strategies for HL-LHC*. Accelerators & Technology Sector Note CERN-ACC-2022-0004. CERN, 2022. URL: <https://cds.cern.ch/record/2808650>
- (4) O. Aberle et al. *High-Luminosity Large Hadron Collider (HL-LHC): Technical Design Report*. CERN Yellow Reports: Monographs CERN-2020-010. Geneva: CERN, 2020. doi: [10.23731/CYRM-2020-0010](https://doi.org/10.23731/CYRM-2020-0010). URL: <https://cds.cern.ch/record/2749422>

Seminars

- (1) Maël Le Garrec. *Correction of Decapolar Resonances in the LHC*. Goethe Universität, Frankfurt, 2023